

Aircraft and spacecraft observations of high-energy radiation associated with lightning leaders

Chris Alexander Kallevik Skeie

Thesis for the degree of Philosophiae Doctor (PhD)
University of Bergen, Norway
2022

UNIVERSITY OF BERGEN



Aircraft and spacecraft observations of high-energy radiation associated with lightning leaders

Chris Alexander Kallevik Skeie



Thesis for the degree of Philosophiae Doctor (PhD)
at the University of Bergen

Date of defense: 03.10.2022

© Copyright Chris Alexander Kallevik Skeie

The material in this publication is covered by the provisions of the Copyright Act.

Year: 2022

Title: Aircraft and spacecraft observations of high-energy radiation associated with lightning leaders

Name: Chris Alexander Kallevik Skeie

Print: Skipnes Kommunikasjon / University of Bergen

Acknowledgements

Through this PhD journey, I have had many people at my side I wish to thank. First I would like to thank my union representatives Jan Georg Tangenes and Kjetil Heitmann as well as my current supervisors Martino Marisaldi and Nikolai Grigorievich Lehtinen, for all your support and guidance. Without you, this thesis would never have been finished...

During these four years, I have gotten to know all my fellow PhDs better, and I would like to thank you all for the fun times we have had and the helpful discussions, both professional and nonsense lunch discussions. My only regret is that we never got to try and make one of our "extremely well" thought of business ideas, like the chopstraw or zap-fit. I want to extend an extra thank you to Anders, Ingrid and Eldho, for always being helpful, and for making these years fun and eventful.

I would also like to thank the 'Energetic Particle Precipitation' and 'Dynamics of the Asymmetric Geospace' groups, as well as David and Brant from the "Hard Radiation from Thunderstorms" group for many good conversations and discussions. I would also like to thank my former Master's supervisor Pavlo Kochkin, who helped spark my interest in lightning.

A wish to thank my father Tor Edward, and sister Marthe Christina, for their support during these years, always willing to lend an ear, and my mother Sigrun for always believing in me.

Finally, I would like to thank Carolina Maiorana, for all the patience, understanding, and support during this period, for which I am eternally grateful.

Chris Alexander Skeie
Bergen, June 2022

"Electricity is really just organised lightning"

George Carlin

Outline

This thesis consists of an introductory part and three scientific papers. The papers, found in Chapter 7, have all been submitted to international, peer-reviewed journals, where two of the papers have so far been published. The third paper of this thesis is currently in review, as of 16th of Mai 2022.

1. C. A. Skeie, N. Østgaard, N. G. Lehtinen, D. Sarria, P. Kochkin, A. I. de Boer, M. Bardet, C. Allasia, F. Flourens, (2020) *Constraints on Recoil Leader Properties Estimated from X-ray Emissions in Aircraft-triggered Discharges*, Journal of Geophysical Research: Atmospheres **125/14**
2. A. Lindanger, C. A. Skeie, M. Marisaldi, I. Bjørge-Engeland, N. Østgaard, A. Mezentsev, V. Reglero, O. Chanrion, T. Neubert, (2022) *Production of Terrestrial Gamma-ray Flashes During the Early Stages of Lightning Flashes*, Journal of Geophysical Research: Atmospheres **127/8**
3. C. A. Skeie, N. Østgaard, A. Mezentsev, I. Bjørge-Engeland, M. Marisaldi, N. Lehtinen, V. Reglero, T. Neubert, (2022) *The temporal relationship between Terrestrial Gamma-ray flashes and associated optical pulses from lightning*, Journal of Geophysical Research: Atmospheres (IN-REVIEW (16.05.2022))

Papers I have worked on as a co-author while being a PhD candidate (not included in this thesis):

- C. Maiorana, M. Marisaldi, M. Füllekrug, S. Soula, J. Lapierre, A. Mezentsev, C.A. Skeie, M. Heumesser, O. Chanrion, N. Østgaard, T. Neubert, V. Reglero, (2021) *Observation of Terrestrial Gamma-Ray Flashes at Mid Latitude*, Journal of Geophysical Research: Atmospheres **126/18**
- A. Lindanger, M. Marisaldi, D. Sarria, N. Østgaard, N. Lehtinen, C.A. Skeie, A. Mezentsev, P. Kochkin, K. Ullaland, S. Yang, G. Genov, B. E. Carlson, C. Köhn, J. Navarro-Gonzalez, P. Connell, V. Reglero, T. Neubert, (2021) *Spectral Analysis of Individual Terrestrial Gamma-Ray Flashes Detected by ASIM*, Journal of Geophysical Research: Atmospheres **126/23**
- I. Bjørge-Engeland, N. Østgaard, A. Mezentsev, C. A. Skeie, D. Sarria, J. Lapierre, A. Lindanger, T. Neubert, M. Marisaldi, O. Chanrion, K. Ullaland, S. Yang, G. Genov, F. Christiansen, V. Reglero, (2022) *Terrestrial Gamma-ray Flashes with Accompanying Elves, detected by ASIM*, Journal of Geophysical Research: Atmospheres

List of Abbreviations

<i>AGILE</i>	Astro-rivelatore Gamma a Immagini Leggero
<i>ASIM</i>	Atmosphere-Space Interactions Monitor
<i>BATSE</i>	Burst and Transient Source Experiment
<i>BGO</i>	Bismuth-Germanium-Oxide
<i>CG</i>	Cloud to Ground
<i>CGRO</i>	Compton Gamma Ray Observatory
<i>CZT</i>	Cadmium-Zinc-Telluride
<i>ELF</i>	Extremely Low Frequencies
<i>FoV</i>	Field of View
<i>GRB</i>	Gamma-ray Bursts
<i>GLD360</i>	Global Lightning Detection Network
<i>HED</i>	High-energy Detector
<i>IC</i>	Intra-Cloud
<i>ILDAS</i>	In-flight Lightning Damage Assessment System
<i>LED</i>	Low-energy Detector
<i>LF</i>	Low Frequency
<i>LP</i>	Lower Positive
<i>LIS</i>	Lightning Imaging Sensor
<i>MN</i>	Main Negative
<i>MP</i>	Main Positive
<i>MMIA</i>	Modular Multi-spectral Imaging Array
<i>MXGS</i>	Modular X- and Gamma-ray Sensor
<i>NLDN</i>	National Lightning Detection Network
<i>NLR</i>	Royal Netherlands Aerospace Centre
<i>PMT</i>	Photomultiplier Tube
<i>RREA</i>	Relativistic Runaway Electron Avalanche
<i>RHESSI</i>	Ramaty High Energy Solar Spectroscopic Imager
<i>TGF</i>	Terrestrial Gamma-ray Flash
<i>TOA</i>	Time of Arrival
<i>TOGA</i>	time of group arrival
<i>TLE</i>	Transient Luminous Event
<i>TRMM</i>	Tropical Rainfall Measuring Mission
<i>VLF</i>	Very Low Frequency
<i>WWLLN</i>	World Wide Lightning Location Network

Contents

Acknowledgements	i
Outline	iii
List of Abbreviations	v
1 Introduction	1
1.1 Objectives	2
1.2 Outline	3
2 Atmospheric Electricity	5
2.1 Thunderclouds and cloud electrification	5
2.2 Lightning flashes	6
2.2.1 Electron avalanches	7
2.2.2 Streamers	7
2.2.3 Leaders	9
2.2.4 Photon emissions associated with thunderclouds and lightning .	11
2.2.5 Radio atmospherics from Lightning	11
3 Aircraft in thunderstorm environment	15
3.1 Aircraft-triggered lightning flashes	16
3.2 Local electric field signature of an aircraft-triggered lightning flash . . .	18
3.2.1 Initial phase of aircraft-triggered lightning flash	18
3.2.2 Recoil events	19
4 High-energy radiation from thunderstorm environments	21
4.1 X-rays from lightning leaders	21
4.1.1 Stepped leaders	22
4.1.2 Recoil Events	22
4.1.3 The ILDAS instruments	23
4.2 Terrestrial Gamma-ray Flashes	25
4.2.1 Mechanisms for production of TGFs	26
4.2.2 TGF-lightning connection	28
4.2.3 Observations of TGFs	29
4.2.4 ASIM instrument	31
5 Introduction to the papers	35

6	Conclusions	39
7	Scientific results	57

Chapter 1

Introduction

Since *Wilson* (1924) first suggested a connection between the emissions of X-rays and electrons accelerated in the electric fields of thunderclouds, many high-energy phenomena related to thunderclouds and lightning have been observed. Terrestrial Gamma-ray Flashes (TGFs) are sub-millisecond bursts of X- and gamma-radiation with energies up to several tens of MeV. They are the most energetic naturally occurring phenomena on Earth, and were first detected by the Burst and Transient Source Experiment (BATSE), onboard the Compton Gamma-ray Observatory (*Fishman et al.*, 1994). Since then, many more space-borne instruments have made detections of the TGFs, with the Atmosphere-Space Interactions Monitor (ASIM) being the first instrument specifically designed to detect them (*Neubert et al.*, 2019).

While the connection between TGFs and thunderclouds was immediately recognised, it was first thought that they were created far above the thunderclouds at altitudes over 40 km (*Lehtinen et al.*, 1996; *Nemiroff et al.*, 1996). The reason for this hypothesis was that X- and gamma-radiation originating at lower altitudes would be strongly attenuated, while the detected energies were very intense. With more observations, the production altitude was found to be at the top part of thunderclouds (*Carlson et al.*, 2007; *Cummer et al.*, 2014; *Dwyer and Smith*, 2005; *Hazelton et al.*, 2009; *Lindanger et al.*, 2021; *Mailyan et al.*, 2016; *Pu et al.*, 2019; *Stanley et al.*, 2006; *Xu et al.*, 2012), and TGFs were found to be associated with negative leaders of intracloud lightning (IC+) (*Cummer et al.*, 2015; *Lu et al.*, 2010; *Pu et al.*, 2019; *Shao et al.*, 2010; *Stanley et al.*, 2006; *Østgaard et al.*, 2013). The production of the TGFs themselves is still not fully understood. Two main theories have been suggested, which are both built on a process called Relativistic Runaway Electron Avalanches (RREA) (*Gurevich et al.*, 1992), in which electrons are accelerated to relativistic energies in the electric fields of thunderclouds. The electrons then radiate energetic photons by bremsstrahlung. After this part, the two theories differ in how the high quantity of seed electrons are created. One theory is the Relativistic Feedback model (*Dwyer*, 2003), in which seeding of RREA is achieved by backscattered X-rays and positrons. The other theory involves the acceleration of electrons in the transient and superposed electric fields of lightning leader and streamers (*Celestin and Pasko*, 2011; *Moss et al.*, 2006). The two theories are not mutually exclusive and could be in effect at the same time. Many questions about TGFs are still unanswered, for example, the occurrence rate of TGFs, source luminosities, production mechanisms, as well as how exactly the TGFs are connected to the lightning flashes.

First in 2001, it was theorised that the emissions of X-rays could be linked to the lightning leader itself (*Moore et al.*, 2001). This was shown to be the case by *Dwyer et al.* (2005), who found that the observed bursts of X-rays were associated with the stepping process of negative leaders. Both natural and triggered lightning have been observed to produce microsecond-long bursts of X-rays (*Dwyer et al.*, 2004, 2005; *Howard et al.*, 2010; *Kochkin et al.*, 2015; *Saleh et al.*, 2009; *Schaal et al.*, 2012), with typical photon energies of a few hundred keV. These bursts as mentioned above, are found to be associated with the stepping process of negative leaders, and also with recoil events, which happen later in the lightning flash. During a recoil event, large currents pass through an already existing leader channel, which heats the lightning channel and emits visible light. These events are some of the most luminous parts of the lightning flash.

Other events tied to the acceleration of electrons and emissions of X- and Gamma-rays have also been observed. Gamma-ray Glows are seconds to minutes long-lasting emissions of X- and Gamma-rays, thought to be caused by continuous RREA in thunderclouds (*Babich et al.*, 2010; *Chilingarian et al.*, 2010; *Torii et al.*, 2004; *Tsuchiya et al.*, 2007). The first airborne observations of Gamma-ray Glows were presented in *McCarthy and Parks* (1985) and *Parks et al.* (1981), which also showed that the gamma-ray emissions were terminated by lightning, and not created by it. Gamma-ray glows have since been observed in multiple other aircraft campaigns (*Kelley*, 2014; *Kochkin et al.*, 2017; *Østgaard et al.*, 2019a), as well as balloon flights (*Eack et al.*, 1996a,b, 2000). Gamma-ray Glows are also observed from the ground (*Brunetti et al.*, 2000; *Chubenko et al.*, 2000; *Torii et al.*, 2002, 2009), where they are sometimes called Thunderstorm Ground Enhancements, due to the glows being detected on the ground.

1.1 Objectives

The objective of this thesis is to further investigate high-energy radiation associated with lightning leaders, as observed from aircraft and space-borne instruments.

Paper I in this thesis gathers airborne observations of high-energy X-rays from so called recoil events, which are then used together with 3 different consecutive models. The first model investigates if electrons accelerated over short distances are accelerated to the full applied potential. The second model simulates the X-ray spectra based on different initial energy electrons, provided from the first model. The third model investigates the electric field between the recoil leader and the aircraft, based on gap distance and leader lengths, which is constrained by the potentials from the fits of the second model. From the results of these simulations, we derive constraints on recoil leader properties, such as length and distance between aircraft and leader is obtained.

Paper II investigates the connection between lightning discharges and Terrestrial Gamma-ray Flashes (TGFs), using observations of TGFs from space-borne instruments and correlating them with ground-based lightning radio data. The study investigates during which stage in a lightning flash the TGFs are observed. For this purpose the study uses the previously mentioned observations, but also includes TGF detections where optical data, associated to the propagation of the lightning leader is available. The TGFs with optical data have very high temporal resolution, and are used to give the study a more detailed view of the time sequence of each flash.

Paper III continues the investigation of TGFs using optical data. The paper investigates the temporal relationship between TGFs and associated optical pulses using space-born observations of the two. The order of TGF and optical pulse onset is addressed, as well as the relationship between the duration of TGFs, and the time interval between the onset of TGF and the onset of optical pulse.

1.2 Outline

In chapter 2 of this thesis the reader will be given an introduction to atmospheric electricity. The chapter first describes thundercloud formation and electrification, then gives an introduction to the mechanisms involved in a lightning flash. Chapter 3 will give an overview of effects on Aircraft in thunderstorm environment, with a focus on how the aircraft takes part in the creation of lightning flashes, as well as some aircraft-observed lightning events. Chapter 4 will outline the creation and observations of high energy radiation from thunderstorm environment, both from aircraft and space-borne instruments. Chapter 5 gives a short summary of the peer reviewed papers included in this thesis, with the results outlined in Chapter 6. The scientific papers of this thesis are included in Chapter 7.

Chapter 2

Atmospheric Electricity

2.1 Thunderclouds and cloud electrification

Formation of clouds happens when air becomes locally supersaturated with water vapour. This normally happens as moist air at ground level is warmed up by sunlight, becomes buoyant and starts to rise. As the air cell rises and the pressure starts to decrease with altitude, moisture in the air will start to condense, forming liquid water droplets. As the pressure and temperature is reduced due to the rise in altitude, the air cell will undergo adiabatic expansion, and the air cell will become supersaturated with water. The altitude at which this happens is most often around 1000 m, where the temperature is well above 0°C. Due to the positive temperatures, these clouds mostly consist of liquid droplets, and can rarely, if ever, produce lightning (*Cooray, 2004*).

The main source of lightning flashes is cumulonimbus clouds, more colloquially called thunderclouds. The cumulonimbus clouds are large, and usually extend up to the tropopause (8 to 18 km) due to large updrafts and vigorous convection inside the cloud. The clouds have shapes reminiscent of anvils, due to the flat tops created by wind shear or convection cut-off at the tropopause. Sometimes the clouds can extend over the tropopause with what is called an overshooting top, which is caused by very strong updrafts (*Rakov and Uman, 2003*). Normally the convection dissipates in a matter of a few hours, however, if the conditions are right, new convective cells can be created around the thundercloud, making up what is known as a multi-cell storm, and in rare cases the convective cell can become self-sustaining, causing the thunderclouds to last much longer. At the altitudes towards the top of the thunderclouds the temperatures drop to $\sim -50^\circ\text{C}$ (*Rakov and Uman, 2003*). Some water particles will start to freeze when the temperature reaches sub 0°C, but some remain liquid while reaching temperatures as low as -40°C , becoming what is called super-cooled liquid, further cooling causes all water particles to freeze. These super-cooled water particles can collide with ice crystals, causing them to freeze on top of them, creating what is called graupel. The graupel pellets can grow and reach sizes ranging from micrometer to centimetre in scale. As the graupels size increases, so does their weight, and eventually the graupel will start to fall.

The electrification of thunderclouds is caused by the distribution and motion of electric charges, which are thought to be the result of collisions between liquid and solid water particles with the graupel. The charge the graupel gains from collisions is dependent on the temperature of the air around it. The graupel theory is based on

experiments performed by *Takahashi* (1978) and *Jayaratne et al.* (1983), who used a cloud chamber with probes in a mixture of super-cooled water and ice to simulate charge gained by the falling graupels. The experiments showed that the polarity and size of the charged regions in the thunderclouds could be explained by temperature in the cloud. Falling graupel first leaves behind positive charge in the upper regions of the cloud, where the temperatures are below -20°C . Further down in the cloud, where the temperatures are between -10 to -20°C the graupel leaves behind negative charge. At temperatures above -10°C the graupel will again leave behind positive charge.

The thundercloud electric structure is complex and dependent on many specific conditions, however, a simplified tripole structure is often used to describe the charge structure of the thundercloud (*Williams*, 1989). Figure 2.1 shows the idealised overview of the charge structure of a cumulonimbus at typical altitudes, consisting of 3 vertically stacked charge layers. The top positive and negative charge regions are referred to as the main positive (MP) and main negative charge regions, and have similar charge magnitudes, while the lower positive (LP) charge region has a much smaller charge magnitude than the MP and MN charge regions (*Williams*, 1989). Occasionally it has been observed that the charge structure is reversed, with the main negative and positive charge regions swapping places. In a non-ideal thundercloud the charge structures will not be static, and will move around as the updrafts and convection changes. A screening layer of negative charge is also often found at the top of the cloud.

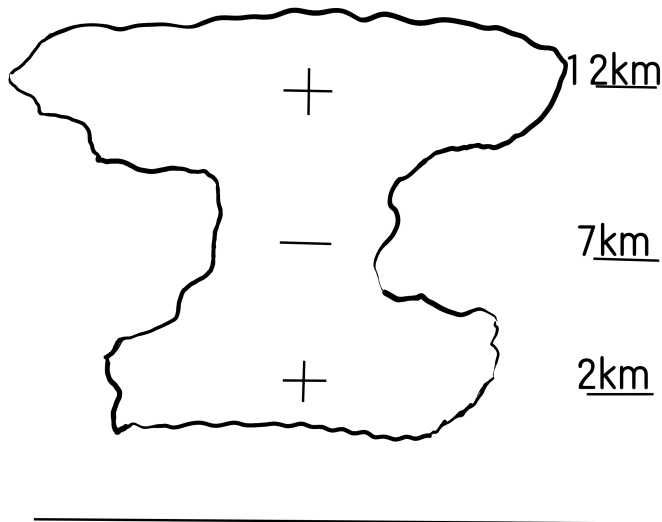


Figure 2.1: Illustration of a vertically stacked tripole charge distribution in a cumulonimbus. The top positive and negative charge layers are thought to be of equal charge, with average of ~ 40 C, while the lower positive is $\sim 10\%$ of the upper positive charge.

2.2 Lightning flashes

A lightning flash, or discharge can be divided into two classes: cloud-to-ground (CG) flashes, which connect to the ground, and cloud discharges. Cloud discharges are fur-

ther divided into discharges between clouds (cloud-to-cloud), discharges inside a cloud (intra-cloud discharges (IC)) and cloud-to-air discharges. Approximately 75% of all lightning flashes are IC discharges (*Rakov and Uman, 2003*), with the remaining discharges being mainly CG flashes. IC discharges are difficult to study, as the opacity of the clouds make it difficult to acquire optical data, and the harsh environment inside the thunderclouds make it difficult to get measurements of the electric charges and currents. Measurements of thundercloud characteristics and lightning-related events have been gathered using space-borne instruments, balloons, as well as aircraft campaigns and radio measurements.

Lightning within the classes described above are usually further divided into positive and negative, based on the direction of the current. Discharges with upward current, i.e., with negative charge transferred downwards, are termed negative, while discharges in which positive charge is transferred downwards are positive. Figure 2.2 shows four scenarios for CG discharges. Panels a) and b) show negative lightning, with a negative leader propagating toward the ground from a negative charge centre in a), or with a positive leader from the ground propagating towards the negative charge centre in the cloud as in b). Positive CGs are shown in panels c) and d), where in c) a positive leader is propagating downwards from the positive charge centre in the cloud towards the ground, and in d) where a negative leader propagates upwards from the ground to the positive charge centre in the cloud. IC lightning follows the same convention. It has been shown that IC+ lightning are associated to the production of bursts of high energy X- and gamma-rays termed Terrestrial Gamma-ray Flashes (TGFs) and are observed from space (outlined in Chapter 4.2).

2.2.1 Electron avalanches

How lightning discharges initiate is still a largely unanswered question. At present time, a key element is thought to be the acceleration of free electrons in the electric fields of thunderclouds, where they initiate electron avalanches. An avalanche occurs when the electric field is strong enough to accelerate electrons to energies such that the interaction between the electrons and atoms and molecules in air will ionise the atoms and molecules, freeing more electrons. The freed electrons will also be accelerated by the electric field, and can in turn ionise more atoms. If the ionisation rate is larger than the electron attachment rate, the electron number grows in an avalanche process. The electric field needed for equal ionisation and attachment rates is called the breakeven field, and is determined to be around 30-31 kV/cm for air at sea-level density and pressure. An electric breakdown may occur at a different field strength, depending on the configuration of electrodes. In the literature, one may often find cited the breakdown field of 32 kV/cm, which is applicable to a 1 cm inter-electrode gap. However, for longer gaps the breakdown may occur in uniform fields as low as 23.6 kV/cm (*Raizer, 1992*).

2.2.2 Streamers

As more and more electron avalanches are initiated, the electric field in front of the avalanche head will start to increase, and when the electric field becomes comparable

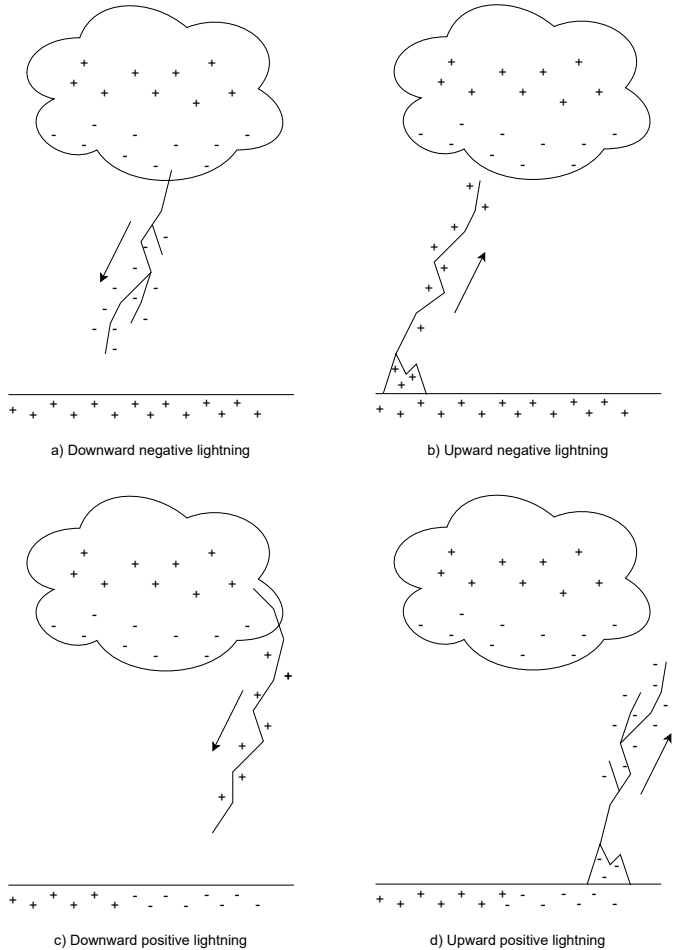


Figure 2.2: Illustration of the four cloud-to-ground scenarios, where electric charge is moved upwards (a and b), or downwards (c and d). Illustration based on figure from (Rakov and Uman, 2003, p. 5).

to the external field, the avalanche will be converted into what is called a streamer discharge. This condition on the spatial charge of the avalanche is called Meek's criterion (Meek, 1940) and allows to calculate the external field necessary for streamer creation in a gap of a given length. The calculated number of electrons needed to create such a field is of the order 10^8 - 10^9 (Meek, 1940). After streamer inception, the streamers themselves will continue to ionise atoms within $\sim 200 \mu\text{m}$ of the streamer head. This distance is known as the boundary of the active region of the streamer. Streamer propagation was proposed by Meek (1940) to be due to by photo-ionisation by UV photons, which are absorbed in the active region of the streamer. If the electric fields reach certain thresholds, the streamers will continue to propagate out of the inception area. This threshold is much lower than the conventional breakeven field, and is found to be $\sim 4.4 \text{ kV/cm}$ for positive streamers, and ~ 8 - 12.5 kV/cm for negative streamers (Lehtinen, 2021; Raizer, 1992, p. 362). In these lower electric fields the streamers will become

isolated due to the high attachment rate, and have low currents and conductivity. As the electric fields in front of the streamers themselves start to increase, the streamers will multiply, gain speed and get higher currents, which can lead to significant heating of the atoms and ions. The heating of atoms and ions will in the end lead to the formation of a highly conductive, hot channel called a leader. This process is thought to produce visible light as the electrons excite nitrogen molecules in the air (*Chanrion et al., 2019*). Streamers are divided into positive (cathode-directed) and negative (anode-directed), based on their charge sign (direction of propagation).

Streamer propagation

Loeb and Meek (1941) was the first to propose the streamer propagation mechanism. The streamer head creates photons, which are radiated forwards from the streamer, ionising the surrounding atoms, producing free electrons. In the high electric fields in front of the streamer head, the free electrons produced from ionisation are accelerated and initiate electron avalanches, as shown in Figure 2.3. For positive streamers these avalanches will grow back towards the streamer head, where they will merge with the positive streamer, thus growing it. The electron avalanche forming in front of the negative streamers will propagate away from the streamer head. However, the negative streamer propagates faster than the electron avalanche and will therefore catch up with the avalanches and merge (*Lehtinen, 2021; Raizer, 1992*). Figure 2.3 shows a schematic overview of positive and negative streamers, with the velocity direction of the electron avalanches.

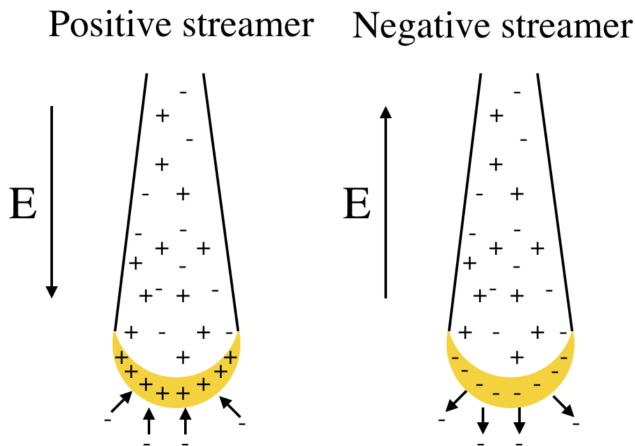


Figure 2.3: Illustration of a positive and negative streamer, where the streamer heads are seen to have net charge associated with the propagation mechanism. Figure from *Dubinova (2016)*.

2.2.3 Leaders

According to *Rakov and Uman (2003)*, the conversion from streamer to leader happens as the conductivity of the streamer reaches values of the order of 10^4 S/m. This happens

as streamers form around a common stem, and their combined currents lead to joule heating of the stem. The high temperature of the stem will lead to higher ionisation rates, freeing more electrons in the gas of the stem, further increasing the conductivity and in the end forming a highly conductive channel. This channel, which consists of a quasi-neutral plasma is called a leader, and is called positive or negative depending on which sign charge is in excess and the direction of propagation. Due to the high conductivity in the leader, a high electric field region will form ahead of the leader tip, in which streamers can form and propagate. The leader will then extend into the newly created streamer region and make it part of the leader, thus increasing the length of its channel. The minimum electric field needed for the leader to propagate was found to be 1 kV/cm (*Bazelyan and Raizer, 2000; Cooray, 2004*). As the leader propagates, electric charges will move, creating a current which emits radio signals and optical emissions. As the leader attaches to the ground or a charge centre, a larger current surge will occur, resulting in very bright emissions of light, as well as large-amplitude very low frequency (VLF) pulses. The emission of light from the lightning leader is thought to be associated to the dissociation of O₂ into atomic oxygen, when the current heats the leader channel (*Chanrion et al., 2019*).

Positive leaders

Positive leaders initiate with positive streamers making up a positive leader channel, as described in section 2.2.2. The positive leader head will consist of positive charge, which will enhance the electric field in front of it, supporting streamer inception and propagation. The current of the streamers heats the region in front of the leader, and as new streamers are created from the tip they cause more heating, which allows the positive leader to propagate forward (*Gorin et al., 1976; Rakov and Uman, 2003*).

Negative leaders

The propagation of negative leaders as observed from laboratory experiments is characterised by presence of so-called steps, which are rarely observed in positive leaders. The process of stepping is illustrated in Figure 2.4 as a streak photography over time, with electrode current measurements below. The negative leader (1) starts with a leader channel growing from a negative high-voltage electrode, with a net negatively charged bright leader head (2). A space stem (4) (also termed a pilot by (*Gallimberti et al., 2002*)) will form in front of the negative leader. In the electric field between the space stem and negative leader tip, positive streamers are formed (3), which will propagate back towards the negative leader. Negative streamers (5) are formed at the opposite side of the space stem, and propagate in the same direction as the negative leader. The leader tip will develop quasi-continuously downwards, while the space stem moves in front of it. The space stem will become a space leader (6) by thermalisation and develop both towards the negative leader and away from it. For this reason it is also referred to as a bidirectional leader. As the positive end of the space leader reaches the negative leader tip (7) they merge, and the higher potential of the negative leader channel is moved to the negative end of the bidirectional leader. This is followed by corona streamers or a bursts of negative corona (8). During the merging process (7), current waves travel upwards through the leader, and the channel lights up. This is called a negative leader

step, and has been shown to be associated with emissions of high-energy photons from bremsstrahlung of accelerated electrons. A new space stem is developed during step 8, which can initiate the next leader step, thus continuing the negative leader propagation (Biagi *et al.*, 2010; Gorin *et al.*, 1976).

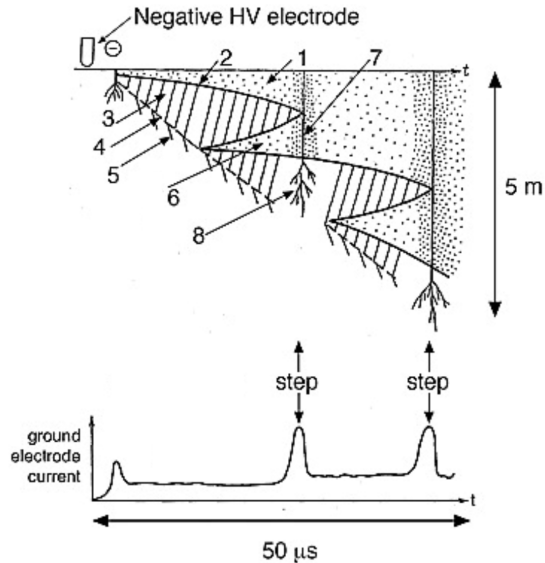


Figure 2.4: Illustration of the steps involved in negative leader propagation. Image adapted from Gorin *et al.* (1976).

2.2.4 Photon emissions associated with thunderclouds and lightning

In addition to visible light caused by the lightning itself, thunderclouds and lightning have been associated with a plethora of other optical events. Figure 2.5 show an overview of many of these events, dubbed transient luminous events (TLEs), with approximate altitudes. These TLEs have different production mechanisms, but most of them have in common that they are produced by particles accelerated in the electric fields associated with thunderclouds and/or lightning discharges, with a few being byproducts of each other. In addition to these TLEs, thunderclouds and lightning have been observed to create high-energy X- and gamma-rays, which will be described further in chapter 4.

2.2.5 Radio atmospherics from Lightning

Lightning discharges have been found to emit radio waves with a wide range of frequencies, stretching from VLF (3-30 kHz) up to low frequency (LF) (30-300 kHz) and above (Rakov and Uman, 2003). These radio waves, which are often referred to as

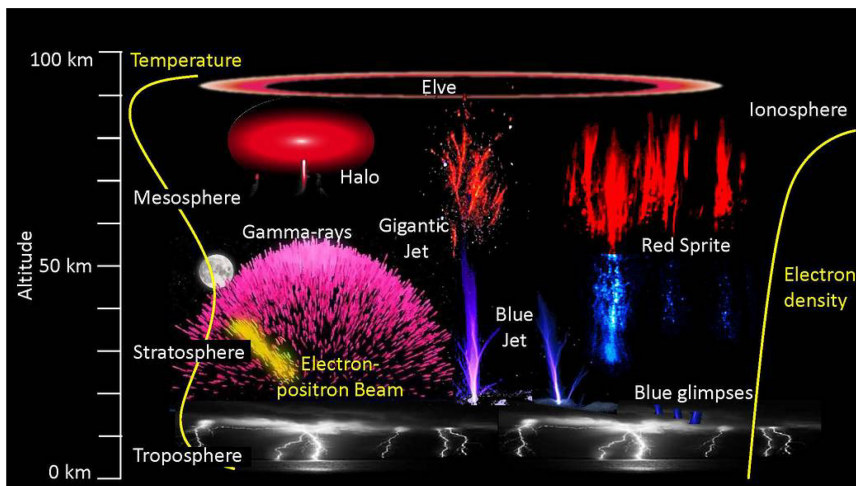


Figure 2.5: Overview of some of the transient luminous events. The image of the moon is added to give the visual scale of the phenomena as perceived from ground. Image from Neubert et al. (2019)

lightning radio atmospherics, or sferics for short, can be detected over vast distances (thousands of kilometers). This is due to the sferics being reflected by the Earth's surface and the ionosphere, if the radio frequencies are below the plasma frequencies of the ionosphere. The sferics can be used for many observations, like the remote sensing of charge motion in a lightning flash or geo-location of lightning flashes. Geo-location can be done by triangulation of the signal, based on the difference in the times of arrival (TOA) of the sferic to different receiver stations. For this purpose the VLF band is usually selected, as it is easily detectable for up to several thousands of kilometres (Dowden et al., 2002). Another way to geo-locate sferics is using the magnetic direction finding method, in which a vertical current like that of a lightning discharge is detected by the horizontal component of the magnetic field it generates (Mehranzamin et al., 2019). These two methods are often used together by lightning location networks. There are many active lightning detection networks, some of the largest ones are the World Wide Lightning Location Network (WWLLN), and Vaisala's Global Lightning Detection Network (GLD360). There are also many regional detection networks, like the National Lightning Detection Network (NLDN) in the United States of America. For the papers included in this work we have used sferics from Vaisala's GLD360 and WWLLN, which are briefly described in the following two sections.

Vaisala's GLD360

Vaisala's Global Lightning Detection Network (GLD360) is a sferic detection network, which provides mainly time and location data of lightning flashes, but also other characteristics such as peak currents with polarity. The GLD360 is a ground-based lightning radio detection network which is sensitive mainly to VLF and lower LF frequencies (500 Hz to 50 kHz), and is well described in Demetriades et al. (2010); Said and Murphy (2016); Said et al. (2010, 2013). The network uses both difference in time of arrival, and magnetic direction finding at each sensor to geo-locate individual light-

ning discharges. GLD360 has an expected detection efficiency of $\sim 75\text{-}85\%$ for CG flashes, which is reduced to $\sim 40\text{-}50\%$ for IC flashes. The geo-location has a median uncertainty of only 2-6 km (*Demetriades et al.*, 2010; *Said and Murphy*, 2016).

World Wide Lightning Location Network

The World Wide Lightning Location Network is a global lightning detection and geo-location network developed by the University of Washington. The network currently consists of over 70 stations across the globe (<http://wwlln.net/>, visited 3/6/2022). The network relies on the time of group arrival (TOGA) (*Dowden et al.*, 2002), which is a method that uses the whole wavetrain, and not just the initial pulse of the radio wave. The network is sensitive to VLF frequencies (3-30 kHz), and a minimum of five sensors are needed to geo-locate sferics. The global location accuracy was found to be $\sim 2\text{-}20$ km, with a median of 3 km and average of ~ 3.5 km (*Lay et al.*, 2005; *Rodger et al.*, 2005). The detection efficiency of WWLLN is dependent on location, where North America, South East Asia and Europa have high detection efficiencies (*Hutchins et al.*, 2012).

Chapter 3

Aircraft in thunderstorm environment

Lightning flashes involving aircraft can be separated into two groups: lightning flashes where the lightning leader is intercepted by the aircraft, and lightning flashes that are initiated by the aircraft itself. The majority of lightning flashes are initiated by the aircraft itself, with only $\sim 10\%$ of lightning flashes being intercepted by the aircraft (Rakov and Uman, 2003). It is estimated that aircraft will be involved in the triggering and/or initiation of a lightning flash once per 1000 flight hours, meaning about once per year (Rakov and Uman, 2003). For larger modern aircraft, the lightning flash is mostly harmless, as the aircraft hull is made of composit material, which works as a conductive tube, with the inside surface being isolated from the outside of the aircraft; however, catastrophic accidents are known to occur. The initiation of aircraft-triggered lightning is associated with static charging of the aircraft, by precipitation particles in the thunderclouds (Morgan *et al.*, 2012; Rakov and Uman, 2003; Uman and Rakov, 2003), and is most probable to happen when the aircraft is inside the cloud, at altitudes where the temperature reaches $0\text{ }^{\circ}\text{C}$ or less (Fisher *et al.*, 1977). Most aircraft are equipped with static wicks, which are proprietary-design devices that remove charge from the aircraft during flight, to hinder buildup of electric charge. The majority of damage to aircraft comes from the attachment points of the lightning to the aircraft, therefore those places are where the aircraft is thoroughly investigated for damage after each aircraft-triggered or intercepted lightning flash. The lightning attachment points and the process involved have therefore been extensively investigated (Fisher *et al.*, 1988; Miller, 1968; Morgan *et al.*, 2012; Reazer *et al.*, 1987; Skeie, 2018). The thunderclouds themselves are also hostile towards the aircraft, with strong and chaotic winds and updrafts. Due to these dangers, aircraft mostly avoid thunderclouds, choosing to fly around or wait until the thunderclouds pass. The avoidance of thunderclouds leads to increased operations costs, due to the additional flight time and fuel consumption, which in turn has lead to research into better charge control methods of the aircraft.

In this chapter we will provide background information necessary to understand how lightning flashes can be initiated by aircraft, the formation of the bidirectional lightning leader, as well as the components of the lightning flashes as viewed by instruments on board the aircraft. For this purpose, this chapter will use use examples of observations made from the In-flight Lightning Damage Assessment System (ILDAS), which is also used in chapter 4 and the scientific papers of this thesis. ILDAS was at the time (2014-2016) mounted on board an Airbus aircraft performing icing tests, which had the aircraft staying at altitudes where the temperature was $0\text{ }^{\circ}\text{C}$.

3.1 Aircraft-triggered lightning flashes

The charging of the aircraft happens as precipitation particles in the cloud collide with the aircraft, depositing charge acquired by static charging and triboelectric effect. The sign of the charge is dependent on the temperature and region of the cloud the aircraft is in (see section 2.1). As the aircraft enters a strong ambient electric field (such as those found in a thundercloud), the aircraft will become polarised, and the local electric field on the aircraft will become amplified. The sharpest parts of the aircraft, such as nose, tail and wing tip will experience the largest amplification as they enhance the electric field the most, due to compression of equipotential lines at sharper geometries (Fisher *et al.*, 1977; Morgan *et al.*, 2012). Figure 3.1 shows an electrostatic model of an aircraft in a 100 kV/m ambient electric field. In this figure, one can see that the horizontal electric field is amplified up to 10 times at the nose and tail. The wing tips and edges of the jet engines also show large amplifications.

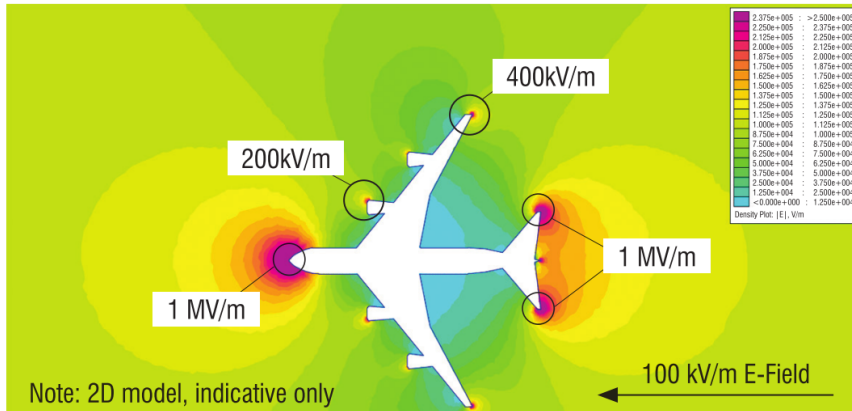


Figure 3.1: Electrostatic model of an aircraft in a 100 kV/m ambient electric field, showing the amplification of the local electric field of the aircraft. Figure from (Morgan *et al.*, 2012)

The intensification of the local electric field can lead to the triggering of a lightning flash from the aircraft itself. The triggered lightning will consist of a bidirectional leader originating at the aircraft itself, that is, the aircraft will be the origin of two oppositely charged lightning leaders (Kasemir, 1960, 2012). Figure 3.2 shows the lightning triggering process for an aircraft. In step I the aircraft is polarised in the presence of the strong ambient electric field of a thundercloud. The positive leader usually starts from the aircraft first, before the negative leader. This is due to the fact that positive and negative streamer threshold mechanisms are different, which leads to the positive threshold being lower than the negative (Lehtinen, 2021; Lehtinen and Marskar, 2021; Rakov and Uman, 2003). Step II in the figure shows such a positive leader, which initiates at a sharp extremity of the aircraft (nose), and propagates in the direction of the ambient electric field. The positive leader attracts negative charge, which will flow to the aircraft, further polarising the aircraft. After a few milliseconds, a negative leader will initiate from a different extremity of the aircraft (tail in step III), and propagate in the opposite direction of the ambient electric field. As the negative leader grows faster,

it is better at transporting negative charge away from the aircraft than the positive leader is at transporting to the aircraft, resulting in a positive net charge of the aircraft, which is observed as a positive increase in the local electric field. Then, the positive leader will start branching, while continuing to gain speed, resulting in a negative net charge on the aircraft, which is observed as an increasingly negative local electric field (Mazur, 1989a; Rakov and Uman, 2003).

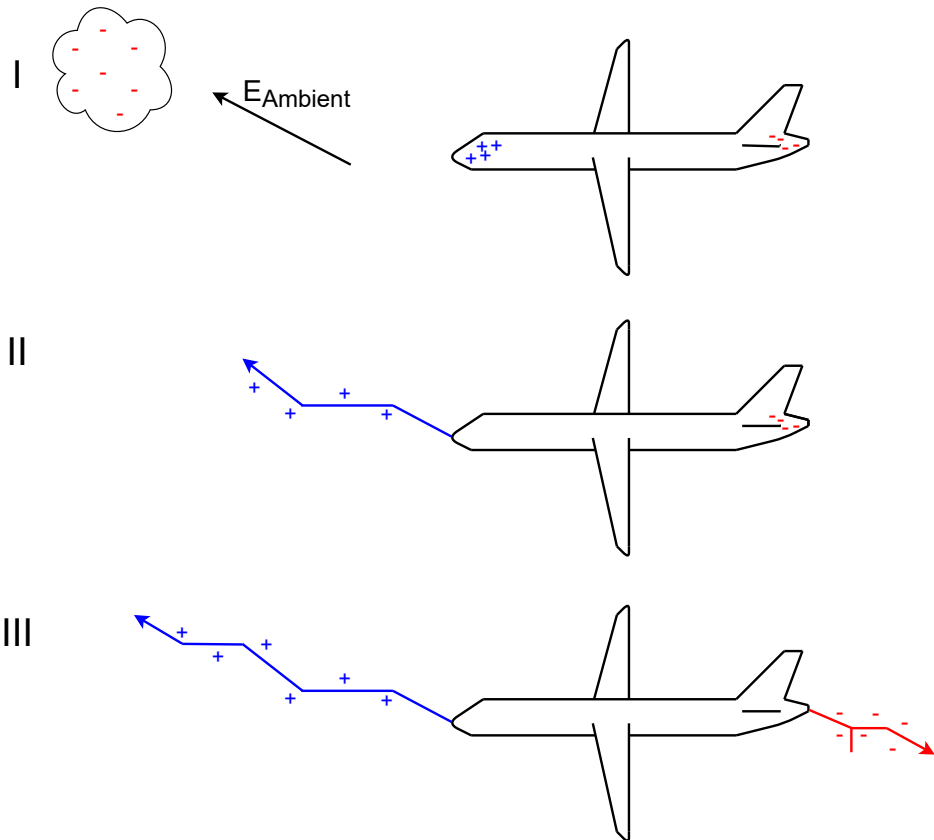


Figure 3.2: Schematic of aircraft-triggered lightning from an aircraft inside a thundercloud. I) The charged aircraft becomes polarised by ambient electric field of a thundercloud. II) A positive leader (blue line) is initiated and propagates with the ambient electric field, further polarising the aircraft. III) A negative leader (red line) initiates from a different extremity of the aircraft, propagating in the opposite direction of the ambient electric field.

In some rare cases, the aircraft-triggered lightning will initiate with a negative coronal discharge at an extremity, before the positive leader is initiated. This is not yet fully understood, but is thought to occur when the aircraft is very slowly negatively charged over time before the aircraft is polarised. The net negative charge could make it easier to initiate a negative corona, over that of a positive leader. Alternatively, the area of the negative charge could hold a sharper geometry than that of the positive charge, so that the electric field is enhanced more where the negative charge resides.

3.2 Local electric field signature of an aircraft-triggered lightning flash

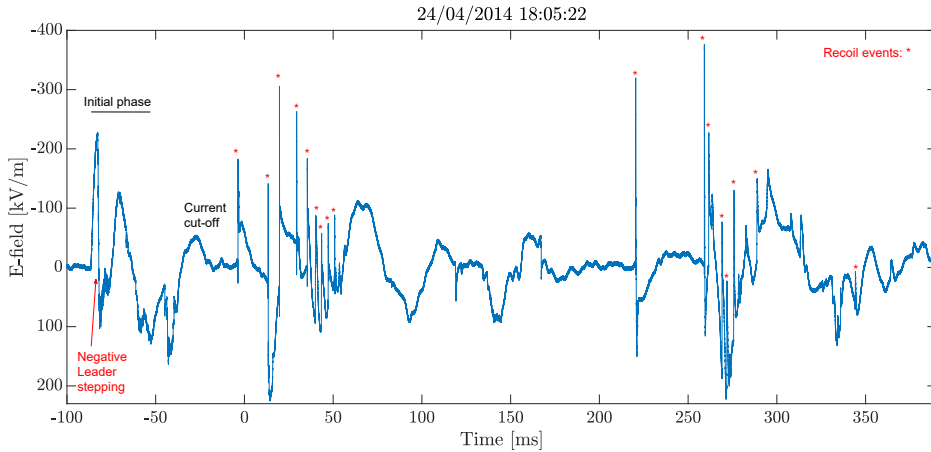


Figure 3.3: Local electric field on board the ILDAS aircraft, which is proportional to the change in the total aircraft charge, during an aircraft-triggered lightning. The flash consists of an initial phase, where a positive and negative leader are initiated from the aircraft. After a current cutoff, multiple spikes in the local electric field are seen, corresponding to so-called recoil events.

Figure 3.3 shows the measured local electric field on board the ILDAS aircraft during a triggered lightning flash. The flash begins at ~ -80 ms and lasts for about 450 ms. The triggered lightning flash starts with an initial phase (expanded in Figure 3.4) during which the positive and negative leaders are initiated, further described in section 3.2.1. Following a current cutoff (between ~ -40 and 0 ms), many fast and sharp spikes are seen in the local electric field (marked with "*"), corresponding to the so-called recoil events, and will be further described in section 3.2.2.

3.2.1 Initial phase of aircraft-triggered lightning flash

Figure 3.4 shows the local electric field on board an aircraft during the triggering of a lightning flash. The positive leader is initiated in time interval A, making the net aircraft charge negative, as negative charges are transported onto the aircraft. After some milliseconds the negative leader initiates at another extremity of the aircraft at the start of time interval B. The negative leader can step, which is seen as the sharp spikes in the measured local electric field, marked with red x-es in the figure, which is outlined in section 4.1. During these steps, the electric field in front of the leader is intensified, and, if high enough fields are reached, they can generate X-ray radiation

from bremsstrahlung of the accelerated electrons. During this period, negative charge is removed by the negative leader faster than it is loaded onto the aircraft by the positive leader, resulting in net positive charge on the aircraft. At the start of time interval C we see the effects of the positive leader gaining speed and starting to branch. More negative charge is again moved onto the aircraft, before the leaders equalise and find an equilibrium (Mazur, 1989a).

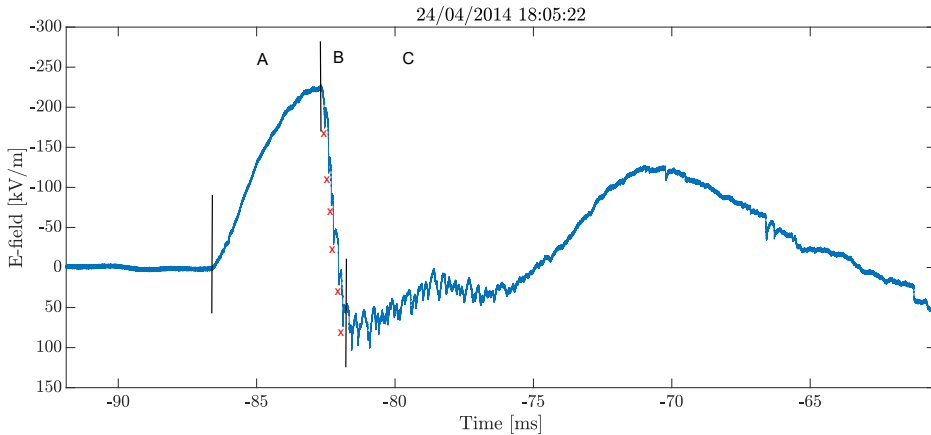


Figure 3.4: Local electric field on board an aircraft, during an aircraft-triggered lightning. The figure shows the initial phase of the lightning flash where a positive leader is initiated (A), negative leader is initiated (B), before the positive leader gains speed and starts to branch (C). The red x-es show the time of the negative leader steps. Adapted from Figure 3 in (Skeie et al., 2020)

3.2.2 Recoil events

Recoil events are considered a collective term for dart- and recoil leaders (Mazur, 2002; Mazur et al., 2013), which are processes during which large currents pass through an already pre-existing lightning leader channel. Due to the large current, the lightning leader is heated, emitting visible light. These events are some of the most luminous parts of the lightning flash. It has been suggested that the events known as K-changes are a type of recoil events, in which negative recoil leaders occur when a positive leader propagates into the negative charge section in a thundercloud (Ogawa and Brook, 1964). Recoil events in aircraft-triggered lightning are observed some milliseconds after the initiation of the negative leader. The mechanism of the recoil events is the following: first, the current cutoff happens, as the positive leader continues to propagate away from the aircraft, causing the leader end connected to the aircraft to cool down and lose part of its conductivity. The propagating positive leader continues to obtain induced charges, which will be distributed as a dipole, forming a negatively charged end towards the aircraft. The amassing of negative charge may lead to a negative electric breakdown at the end of the leader close to the aircraft, forming a negative leader, which is likely to propagate through the already existing cooled channel, until it reaches the aircraft again (Kochkin et al., 2015; Lalande et al., 1999; Laroche et al., 2012; Mazur, 1989a,b; Mazur and Moreaut, 1992; Mazur and Ruhnke, 1993; More-

aut et al., 1992). Figure 3.3 shows the local electric field of a triggered lightning flash, where the "*" symbols show the recoil events as they appear starting just before 0 ms time. Figure 3.5 shows the measured local electric field and currents passing through the aircraft during a recoil event. As seen in this Figure, the electric field is sharply becoming more negative over just a few microseconds, with large current waves passing through the aircraft over tens of microseconds. During these recoil events, as the negative recoil leader approaches the aircraft, the electric field between the two can become large enough to accelerate electrons, which can then undergo bremsstrahlung and emits X-rays, much like the situation for the negative stepping leader. The X-rays associated to recoil leader are further discussed in section 4.1.2.

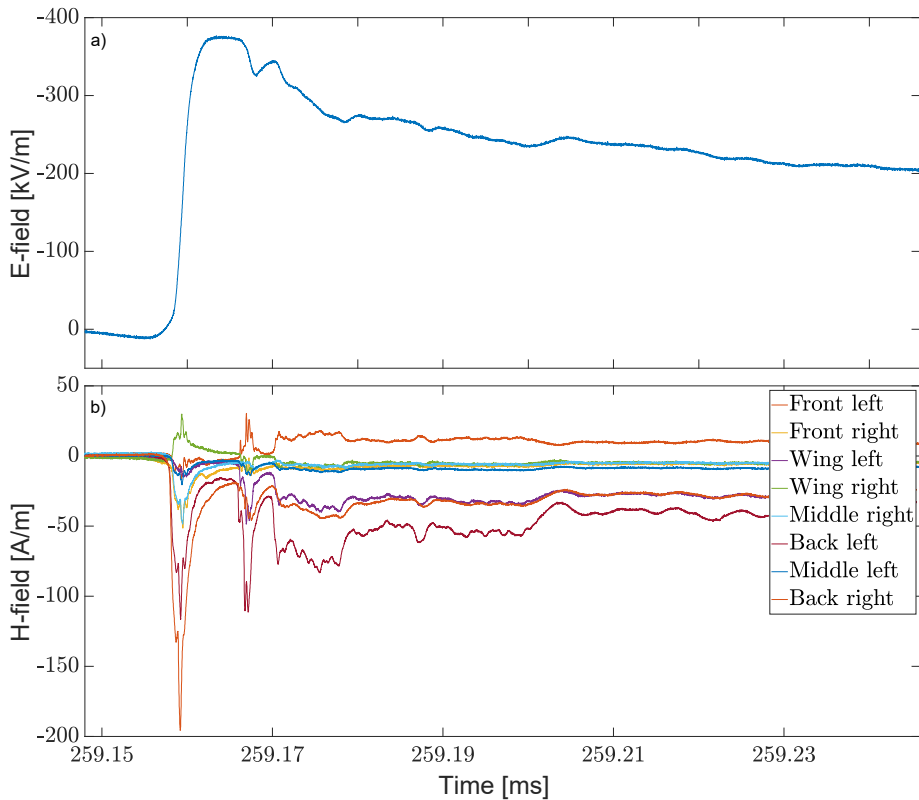


Figure 3.5: a) Local electric field on aircraft during a recoil event. b) measured currents flowing through the aircraft during the recoil event.

Chapter 4

High-energy radiation from thunderstorm environments

The production of high-energy radiation from thunderclouds was first suggested by *Wilson* (1924), who connected the acceleration of electrons in the electric fields of thunderclouds to emission of high-energy photons. Since then, many different radiation-producing events have been linked to the acceleration of particles in the electric fields of thunderclouds, as well as from lightning leaders themselves. The main source of high-energy radiation from thundercloud and lightning-related events is thought to be from bremsstrahlung. Bremsstrahlung, or braking radiation as it is sometimes called, is the process in which electrons, decelerated in a Coulomb field associated to a molecular or atomic nucleus, emits electromagnetic radiation. The energy radiated is dependent on the size of the nucleus as well as the distance at which the electron passes it, and the power radiated in classical approximation is proportional to the square of the deceleration of the electron. Most electrons are decelerated in a series of interactions (*Cember and Johnson*, 2009), rather than one interaction. This chapter will outline the various processes involved in emission of high-energy radiation associated with thunderstorms and lightning leaders in particular. The rest of this chapter will use examples of observations made from the In-flight Lightning Damage Assessment System (ILDAS) and the Atmosphere-Space Interactions Monitor (ASIM) missions, which are also the source of the experimental data used in the research papers of this thesis. The chapter will also include a description of these instruments.

4.1 X-rays from lightning leaders

It has long been known that lightning and thunderclouds are associated with X-ray emissions, but not since the early 2000s has it been shown that both triggered and natural lightning itself can generate short bursts of X-rays. The X-rays in the bursts have typical energies of a few hundred keV, and have been tied to the stepping of negative leaders and recoil events (*Dwyer*, 2004; *Dwyer et al.*, 2004, 2005, 2011, 2003; *Howard et al.*, 2010; *Kochkin et al.*, 2015; *Montanyà et al.*, 2014; *Moore et al.*, 2001; *Saleh et al.*, 2009; *Schaal et al.*, 2012). Multiple major flight campaigns made observations of X-rays already in the 60s-80s, but attributed the X-rays to the thunderstorms, rather than the lightning itself (*Fisher et al.*, 1988; *McCarthy and Parks*, 1985; *Miller*, 1968;

Parks et al., 1981; *Uman and Rakov*, 2003). This section will outline the production and observations of high-energy X-rays generated from lightning leader steps and recoil events.

4.1.1 Stepped leaders

The first to infer the connection between X-rays and stepping leaders were *Moore et al.* (2001), who reported on observations of X-rays in close association with negative stepped leaders in a CG lightning flash. *Dwyer et al.* (2005) later showed that the stepping leader is the source of bursts of X-rays, with typical energies well below 150 keV. Furthermore, *Dwyer et al.* (2005) also found the observations of X-rays to be similar to those of triggered lightning dart leaders, implying they both share a similar production mechanism. During a negative leader step, electrons are thought to be accelerated in the strong electric fields between the negative leader front and the space leaders (see section 2.2.3). The accelerated electrons then emit X-rays via bremsstrahlung as they interact with particles in the air.

Figure 4.1 shows the local electric field in panel a), and energy measurements in b), during the initial phase of an aircraft-triggered lightning as detected by the In-flight Lightning Damage Assessment System (ILDAS). As seen after the negative leader initiation (at time -63 ms), one of the steps (inside the dotted red square) produces a few tens of nanoseconds-long X-ray pulse of ~ 220 keV, thought to be from a single photon. As seen in the figure, the X-ray pulse is closely associated with a small (average of 30 kV/m for ILDAS events) but fast (some microseconds) change in the measured local electric field (*Skeie*, 2018). During the 3 years of flights, only 14 such events have been found in the ILDAS data. This is due to the fact that the negative leaders generating these X-rays are propagating away from the aircraft, so only back-scattered X-rays are detected.

4.1.2 Recoil Events

During recoil events, the recoil leader propagates back towards the aircraft in the pre-made channel. The electric field between the negative recoil leader and the aircraft will be amplified, which can cause electrons in the field to be accelerated. These electrons then undergo bremsstrahlung, emitting X-rays. The X-rays are observed by ILDAS as a few microseconds-long bursts of X-rays with photon energies up to ~ 500 keV, where a burst could contain as many as 12 X-ray pulses that are a few tens of nanoseconds-long (*Skeie et al.*, 2020).

Figure 4.2 shows one of the recoil events detected by ILDAS. Panel a) shows the local electric field on board the aircraft. An ~ 380 kV/m increase in the local electric field is seen, happening over just a few μ s. Panel b) shows the accompanying X-ray emissions, where multiple X-ray pulses with lower energies are observed, before a larger and wider pulse is seen. This wider pulse is thought to be the product of multiple stacking X-ray photons. ILDAS detected 54 recoil events associated with X-rays during the 3 years of flights, where a total of 245 individual nanosecond-long X-ray pulses were detected. These events are presented, and used for the analysis in *Skeie et al.* (2020).

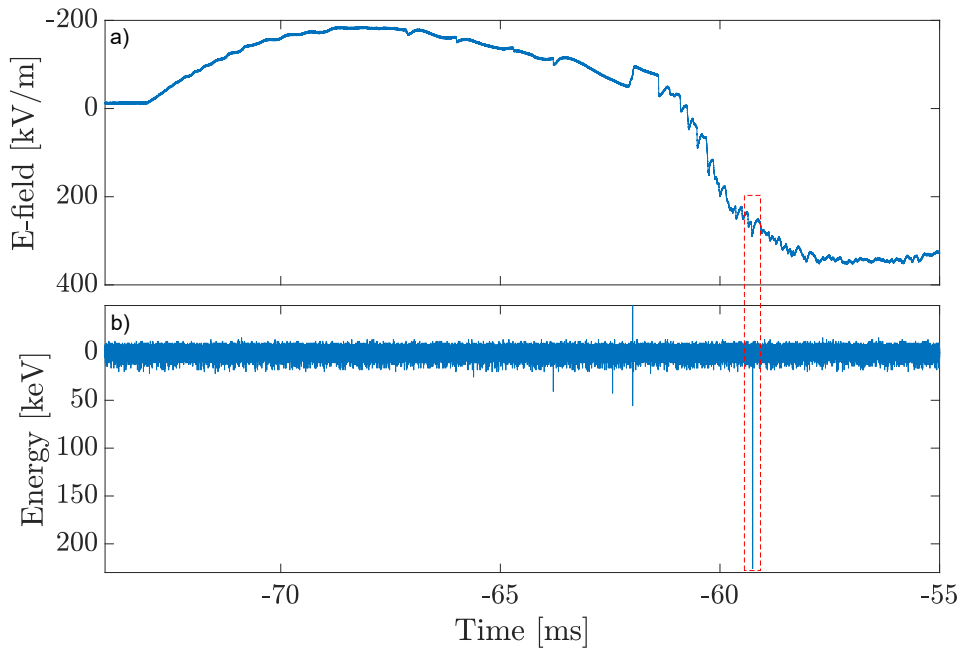


Figure 4.1: Overview of an aircraft-triggered lightning flash, as observed by the ILDAS instruments. *a)* Local electric field on the ILDAS mission aircraft, during the initial phase of a triggered lightning. *b)* $\text{LaBr}_3(\text{Ce})$ high-energy radiation measurements. The dotted red square outlines a leader step, with the accompanying X-ray pulse.

4.1.3 The ILDAS instruments

The In-flight Lightning Damage Assessment System was developed by the Royal Netherlands Aerospace Centre (NLR, <http://ildas.nlr.nl/>) and have had multiple set-ups over the years. The instruments, and the set-ups have been described in detail in *Boissin et al.* (2012); *de Boer et al.* (2011, 2013a,b, 2015); *Hervé et al.* (2014); *van Deursen et al.* (2013); *Zwemmer et al.* (2013a,b). The data presented from ILDAS in this thesis, as well as the data used in *Skeie et al.* (2020), are from 2014-2016, during which ILDAS consisted of 1 local electric field sensor, 8 magnetic field (H-field) sensors and 2 X-ray detectors, distributed on the aircraft as shown in Figure 4.3. The local electric field (E-field) sensor and the magnetic field sensors (H-field sensors) are all differential detectors. A subsequent analog integration of the E- and H-field signals provide a flat response over the frequency bands of 10 Hz to 500 kHz for E-field, and 100 Hz to 10 MHz for the H-fields. Both type of sensors have a sampling rate of 83.3 MHz, which corresponds to a sampling interval of 12 ns. The local electric field sensor mainly serves as a trigger for data recording during lightning flashes, and is time differentiated, meaning the zero value of the field is an unknown magnitude (*Kochkin et al.*, 2015). The measured local electric field is proportional to the total charge change on the aircraft during the integration time of the instrument. The sensor consists of a

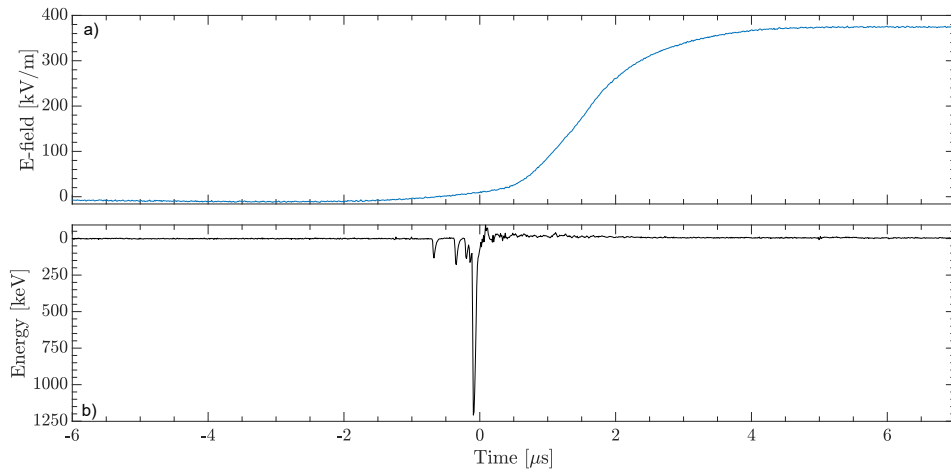


Figure 4.2: Recoil event during aircraft-triggered lightning, as observed by ILDAS. Panel a) shows the local electric field during the recoil event, and panel b) shows the measured energy of the associated X-ray burst. Edited version of figure 4 in (Skeie *et al.*, 2020)

capacitive probe, which is attached to the edge of a window towards the front of the aircraft. The aircraft fuselage is essentially a long conductive tube, where the electric field will always be perpendicular to the surface. During the campaigns considered for this thesis, the sensor was placed at the edge of a window close to the front of the aircraft.

In the ILDAS papers mentioned above, as well as Skeie *et al.* (2020) the polarity of the sensor is chosen such that a positive increase corresponds to an increasingly negative electric field, but for the examples in this thesis the figures have had their axis changed to show a negative increase when the electric field becomes more negative. The H-field sensors measure the current passing through the hull of the aircraft, with six detectors (H02,H03,H09,H07,H08 and H13) measuring the current from nose to tail, and 2 detectors (H04 and H05) measuring the current passing between the wings and the main fuselage of the aircraft. The H-field detectors also integrate the signal over time, meaning we can not measure constant or slowly increasing/decreasing currents passing through the aircraft. The H-field detectors work by measuring the magnetic field on the outer fuselage, which is proportional to the current passing along the aircraft hull (Kochkin *et al.*, 2015). The two X-ray detectors consist of $\text{LaBr}_3(\text{Ce})$ scintillators with 38 mm length and 38 mm diameter crystals, connected to photomultipliers (Kochkin *et al.*, 2015). Due to the fuselage of the aircraft, as well as the protective box of the instrument and the scintillator housing, all X-rays with energies lower than 30 keV are absorbed. The detectors can measure up to 10 MeV, but the sensitivity of the detectors is reduced for energies >550 keV, due to the crystals dimension. The sampling rate of the X-ray detectors are 100 MHz, corresponding to a sampling interval of 10 ns.

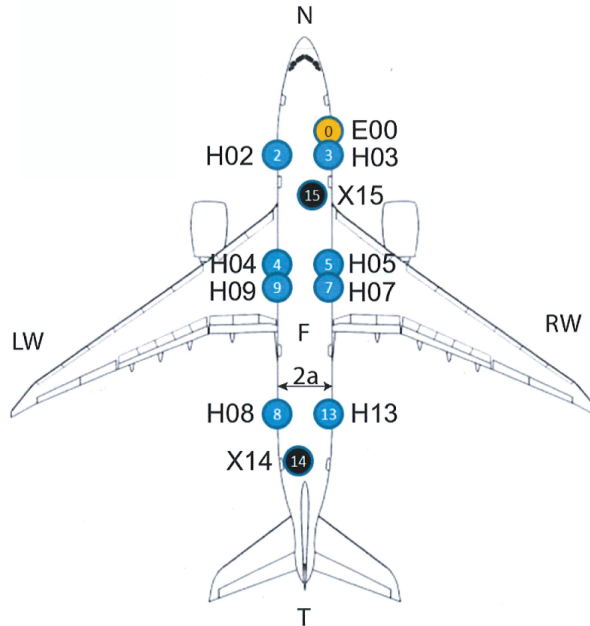


Figure 4.3: Distribution of ILDAS instruments on board the aircraft, in the period of 2014-2016. E00 is the local electric field detector (yellow circle), HXX are the H-field detectors (blue circles), and X14 and X15 are the X-ray detectors (black circles). Figure from Kochkin *et al.* (2015)

4.2 Terrestrial Gamma-ray Flashes

Terrestrial Gamma-ray Flashes (TGFs) are very short bursts of intense X- and gamma-radiation produced in thunderstorms. They were first discovered by chance in 1991, by the Burst and Transient Source Experiment (BATSE) instrument on board the Compton Gamma Ray Observatory (CGRO) (Fishman *et al.*, 1994). Since then, many more TGF and TGF related observations have been made from space borne instruments (Briggs *et al.*, 2013; Grefenstette *et al.*, 2009; Marisaldi *et al.*, 2010, 2014; Smith *et al.*, 2005, 2020; Østgaard *et al.*, 2019b), airborne instruments (Bowers *et al.*, 2018; Smith *et al.*, 2011), ground based instruments (Abbasi *et al.*, 2018; Dwyer *et al.*, 2004, 2012a; Hare *et al.*, 2016; Tran *et al.*, 2015; Wada *et al.*, 2019). Radio measurements in different frequency bands are also used to determine TGF characteristics where the different radio frequencies are used to investigate different properties associated to the TGF-lightning phenomena (Lu *et al.*, 2010; Pu *et al.*, 2019; Shao *et al.*, 2010; Østgaard *et al.*, 2021). All of these detections have improved our understanding of the TGF properties, initiation, and connection to thunderclouds and lightning. This section will outline the leading theories behind the production of TGFs, TGF characteristics and observations of TGFs from space.

4.2.1 Mechanisms for production of TGFs

There are currently two main theories for the production of TGFs. Both theories build on a process called the relativistic electron runaway process (*Wilson, 1924*), in which electrons are accelerated in electric fields strong enough to overcome the friction force of air. The friction force experienced by the accelerated electrons is due to ionising collisions, as well as bremsstrahlung emissions. Figure 4.4 shows the dynamic friction force of electrons in air at sea level density and pressure. The dashed lines show electric field thresholds for different electric breakdown processes. If the force from the electric field is larger than the friction force, the electrons will gain energy and run away. If the electric field is over the thermal runaway value (E_C in Figure 4.4) all electrons will become runaway electrons. The minimum electric field needed for an electron to runaway is called the breakeven field (E_t in Figure 4.4) (*Moss et al., 2006*).

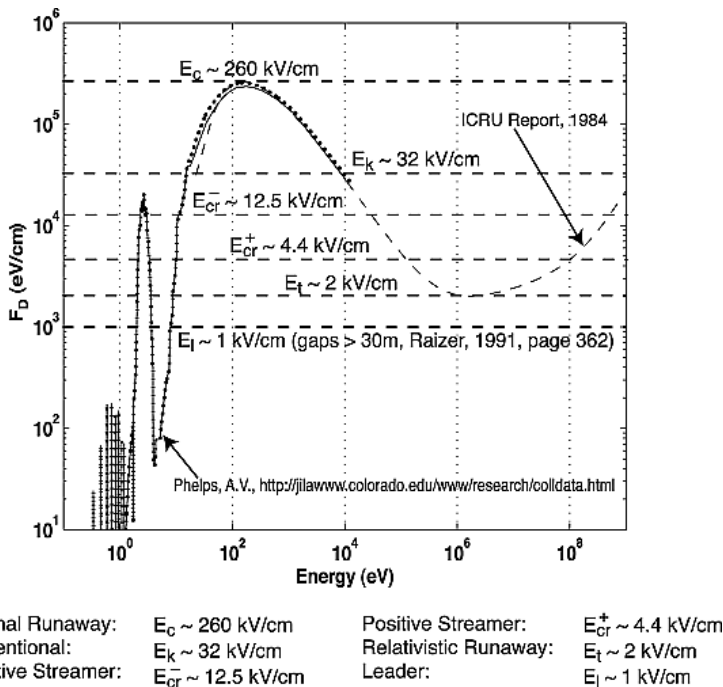


Figure 4.4: Dynamic friction force of electrons in air, at sea-level pressure and density. The dashed lines show electric field values needed for different breakdown processes. Figure from Moss et al. (2006).

The accelerated runaway electrons can then produce more free electrons by elastic scattering with electrons bound in air molecules, through the process called Møller scattering. The freed electrons will then also be accelerated in the electric field, before they can also further Møller scatter, resulting in an avalanche effect referred to as Relativistic Runaway Electron Avalanche (RREA) (*Gurevich et al., 1992*). *Dwyer (2003)* and *Babich et al. (2004)* found that the theoretical threshold to sustain a RREA is an electrical field of 2.8 kV/cm at sea-level, which is $\sim 30\%$ larger than the breakeven field (E_t in Figure 4.4), but still lower than the maximum measured electric fields in thunderclouds ~ 3 kV/cm (*Rakov and Uman, 2003*). This difference is due to the fact

that the calculated dynamic friction force only takes does not take into account electron momentum loss, due to elastic scattering (*Lehtinen and Østgaard*, 2018). Using TGF observations from space, and a Monte Carlo simulation to determine the spectra of TGFs, *Dwyer and Smith* (2005) found that the number of initial electrons at source needed to produce a TGF was $\sim 10^{17}$. This number of seed electrons is much more than what can be explained by cosmic ray showers or natural radioactivity, as well as from RREA multiplication alone (*Dwyer*, 2008). Two different theories have been proposed to solve this lack of electrons at source. One theory is based on what is called thermal runaway, in which low-energy electrons are accelerated in transient, superposed electric fields of the lightning leader and streamers in the thundercloud ambient electric field, which can overcome the friction maximum. The other theory is based on RREA seeded with free electrons with high energies, produced by cosmic ray showers, which can already have energies that are above the friction maximum of ~ 100 eV, and can therefore run away in the electric fields of the thundercloud. In this scenario back-scattered X-rays (from bremsstrahlung of the electrons) and positrons created by pair production seed additional electron avalanches, which again create more back-scattered X-rays and positrons, creating what is called a relativistic feedback mechanism (*Dwyer*, 2008). It should be noted that there is nothing preventing both theories from working at the same time, where the initial seed electrons are created from thermal runaway, before starting the feedback mechanism.

Thermal runaway

Thermal runaway, or cold runaway as it is sometimes called, is a process based on the assumption that the superposition of electric fields of the lightning leader front, streamers and ambient electric field can be strong enough to accelerate low-energy electrons over the friction maximum (*Celestin and Pasko*, 2011; *Moss et al.*, 2006), and run away. The first step of this model is the acceleration of thermal electrons in the electric fields in a streamer zone up to ~ 100 keV. In front of the lightning leader, the electric fields of leader, streamer and ambient field could shortly superpose, and potentially be large enough to accelerate low-energy electrons over the maximum friction. After the electrons have been accelerated past the friction maximum they can initiate the RREA process in the electric field in front of the lightning leader (*Celestin and Pasko*, 2011; *Moss et al.*, 2006). The needed number (10^{17}) of source electrons for TGF production can be created from thermal electrons which are accelerated over the friction maximum. The number of energetic electrons may increase even further if the RREA process takes place.

Relativistic Feedback

The Relativistic feedback theory is built around multiplication of RREAs from electrons created from back-scattered X-rays and positrons (*Dwyer*, 2003). In this theory a seed electron with initial energy of $\gtrsim 1$ MeV is already present, most commonly thought to be produced by cosmic ray interaction with air. The seed electron can then runaway and start a RREA, where X-rays are produced by bremsstrahlung. The X-rays will then produce free electrons and positrons by Compton scattering and pair production. Back-scattered X-rays and positrons (which will propagate backwards in relation to

the electric field), can produce new electrons via pair production and elastic scattering, which in turn can start new RREAs. The multiplication of RREAs can produce enough electrons to explain the needed 10^{17} source electrons. Figure 4.5 shows the processes involved in the feedback mechanism, with approximate number of electrons that can be explained by each process.

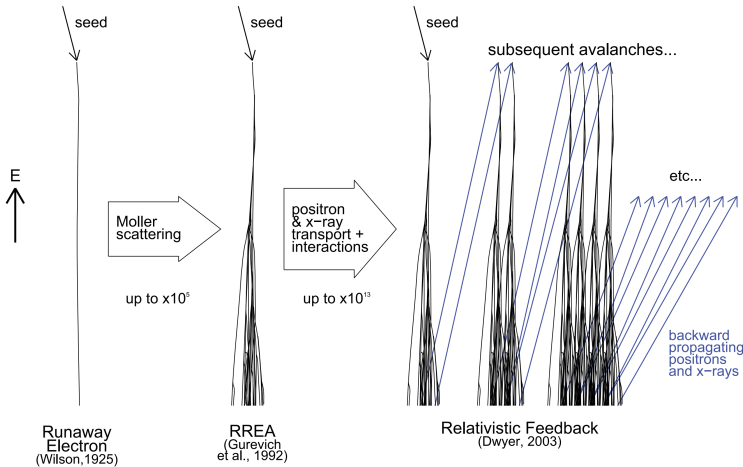


Figure 4.5: Illustration of the mechanisms involved in the multiplication of electrons for the Relativistic feedback theory. A runaway electron is started with an initial high-energy seed electron, which starts the RREA process, which in turn multiplies through the relativistic feedback mechanism. The blue lines show backward propagating X-rays and positrons. Figure from Dwyer et al. (2012b).

4.2.2 TGF-lightning connection

Lightning discharges were first suggested to be connected to TGFs by *Fishman et al.* (1994), who noted that TGFs detected by BATSE were all observed over thunderstorms. Initially it was believed that TGFs could not have been produced at low altitudes, such as inside the thunderclouds, due to the assumption that the photons would be absorbed and not reach the space based instruments. However, with more case studies it was shown that the TGFs were associated with IC+ lightning leaders, moving negative charge, and propagating upwards in the initial phase of the lightning flashes (*Cummer et al.*, 2015; *Lu et al.*, 2010; *Pu et al.*, 2019; *Shao et al.*, 2010; *Stanley et al.*, 2006; *Østgaard et al.*, 2013). This was also shown in *Lindanger et al.* (2022) (part of this thesis) where TGF detections with accompanying optical data was used to show that the TGFs are produced during the initial phase of a lightning flash. The optical light is thought to be emitted as a strong current goes through the lightning leader channel, where air is heated to several thousands of kelvin over a very short timescale. These optical emissions, which are in essence a proxy for the current in the lightning leader channel, can also serve as remote diagnostic of the processes at play. Lightning is also a strong emitter of electromagnetic waves, with frequencies ranging from extremely low frequencies (ELF) to very high frequencies (VLF), which allows for remote sensing of the discharge processes using ground based instruments. Using lightning sferics

together with TGF detections, the TGFs were found to be associated to the radio signals within a few tens of microseconds (*Connaughton et al.*, 2010; *Lindanger et al.*, 2020; *Marisaldi et al.*, 2015; *Stanley et al.*, 2006).

The first to report a simultaneous observation of a TGF and optical light from lightning was *Østgaard et al.* (2013). They reported a TGF detected by the Ramaty High Energy Solar Spectroscopic Imager (RHESSI) and optical detection from the Lightning Imaging Sensor (LIS) on board the Tropical Rainfall Measuring Mission (TRMM). A strong VLF radio pulse was also observed at the same time as the TGF, detected by the World Wide Lightning Location Network (WWLLN). The TGF-optical sequence was re-investigated by *Gjesteland et al.* (2017) using the same instruments, however, they could not determine the sequence of events due to instrumental uncertainties. After ASIM was launched, multiple works have addressed the sequence of TGF-optical light from lightning, showing that the majority of TGFs occur at the onset, or before the optical emissions (*Heumesser et al.*, 2021; *Neubert et al.*, 2020; *Østgaard et al.*, 2019b). These results are further improved in *Skeie et al.* (2022 In review), which is a part of this thesis, where data from a period with lower uncertainty is used to re-address this sequence.

4.2.3 Observations of TGFs

Since their discovery in 1991, TGFs have been extensively studied. This section will outline the characteristics of TGFs, as they they are currently known to be. The TGF characteristics have been determined in large due to the TGFs detected by BATSE, and have since been refined by TGF observations by the Fermi Gamma-ray telescope, RHESSI, the Astro-rivelatore Gamma a Immagini Leggero (AGILE), and recently the Atmosphere-Space Interactions Monitor (ASIM). The determined TGF characteristics are heavily dependent on the instruments used for observing the TGFs and the applied methods. This has lead to many characteristics being refined as newer and better instruments have been used.

The production altitude of TGFs is thought to be at the top of thunderclouds, which are at or below the tropopause height. This was obtained from analysis and modelling of the cumulative energy spectra observed by the various space missions. In the beginning it was first thought that the TGFs were associated to a phenomenon called sprites (see Figure 2.5), and that the TGFs were produced at altitudes above 40 km (*Nemiroff et al.*, 1996). With further spectral analysis and radio measurements it was determined that the production altitude of TGFs is below ~ 20 km altitude (*Carlson et al.*, 2007; *Gjesteland et al.*, 2010), most likely between 10-15 km (*Carlson et al.*, 2007; *Cummer et al.*, 2014; *Dwyer and Smith*, 2005; *Hazelton et al.*, 2009; *Lindanger et al.*, 2021; *Mailyan et al.*, 2016; *Pu et al.*, 2019; *Stanley et al.*, 2006; *Xu et al.*, 2012), placing the production altitude inside the top part of thunderclouds.

TGFs are thought to be X- and gamma-ray radiation produced by bremsstrahlung of accelerated electrons, produced from thermal-runaway and/or relativistic feedback, as outlined in sections 4.2.1 and 4.2.1. The individual photon energies of the TGFs are reported to be up to 40 MeV (*Briggs et al.*, 2010; *Fishman et al.*, 1994; *Marisaldi et al.*, 2010, 2014; *Smith et al.*, 2005), which makes TGFs the most energetic naturally occurring phenomena on Earth. The exact minimum and maximum photon energies are

still unknown, but as the photons are created from the bremsstrahlung process, any energy value up to the maximum energy that an accelerated electron can get in the electric field of a thundercloud. It is important to note that the measured energies are dependent on instrumental effects, such as the sensitivity and dead time of the instrument, photon pile up, etc. As TGFs are produced by bremsstrahlung, they are thought to be distributed in a cone-shaped beam with an opening angle depending on the production model, with an opening angle between 30° and 40° being the most commonly used (Gjesteland *et al.*, 2011; Hazelton *et al.*, 2009; Mailyan *et al.*, 2016). TGFs are usually observed as a single short pulse of X- and gamma-radiation, which has a fast rise time and a tail of low energy photons made from Compton scattering (Grefenstette *et al.*, 2008; Østgaard *et al.*, 2008). The shape of the TGF is often approximated with a log-normal or Gaussian fit. All missions have also reported observing TGFs consisting of multiple pulses (Fishman *et al.*, 1994; Foley *et al.*, 2014; Lindanger *et al.*, 2020; Mailyan *et al.*, 2021; Maiorana *et al.*, 2020; Østgaard *et al.*, 2019b), and the conditions needed for the production of multiple pulses is yet to be understood.

The first spectral analysis of TGFs corroborated the idea that TGFs were high-energy emissions created by the bremsstrahlung process (Dwyer and Smith, 2005; Marisaldi *et al.*, 2010; Smith *et al.*, 2005). Using modelling (Celestin *et al.*, 2015; Skeltved *et al.*, 2017) and TGF observations (Dwyer and Smith, 2005; Dwyer *et al.*, 2012b; Marisaldi *et al.*, 2014), the cumulative TGF spectrum was later found to follow a power law, with an e-folding energy of ~ 7.3 MeV. Spectral analysis have been performed on single TGFs as well. Mailyan *et al.* (2016, 2019), and Lindanger *et al.* (2021) used samples of individual TGFs from the Fermi Gamma-ray telescope and ASIM respectively, and found that there were high variability in the TGF spectra and therefore also in the source properties, like production altitude, opening angle, etc.

The fluence distribution of TGFs detected by previous missions have been fitted to a power law, with an exponent between -2.2 and -2.4 (Marisaldi *et al.*, 2014; Tierney *et al.*, 2013; Østgaard *et al.*, 2012), which was independently determined using data from Fermi, RHESSI and AGILE. As with the detected energies, the fluence measurements are highly affected by instrumental effects, as well as effects due to propagation through the atmosphere. Smith *et al.* (2020) discovered that RHESSI detectors were often paralysed during bright TGFs, detecting only a few counts during the rising phase before being paralysed, which could mean that many high-fluence TGFs were reported as low-fluence TGFs, or not detected as a TGF at all.

The TGF durations have also been proven to be highly dependent on the various mission instruments and instrument dead times. The First TGFs discovered by BATSE were reported to last a few milliseconds. This was improved by later TGF observations (Grefenstette *et al.*, 2009; Lindanger *et al.*, 2020; Maiorana *et al.*, 2020; Roberts *et al.*, 2017), which determined the TGF durations to be close to a hundred microseconds. With the launch of ASIM this was further reduced to below 100 microsecond for the ASIM-detected TGF (Østgaard *et al.*, 2019b). A comparison of the durations between the instruments are difficult, as the different groups have different ways of defining the durations in part due to the difference in number of photons detected in each TGF.

4.2.4 ASIM instrument

The Atmosphere-Space Interactions Monitor, seen in figure 4.6, is an ESA mission, multi-instrument payload, with contributions from Denmark, Norway and Spain, which is mounted on the Columbus module of the International Space Station (*Neubert et al.*, 2019). In Figure 4.6 ASIM is shown in the new placement, after it was moved in 2022, from the rig on the right. This figure was chosen to better show the individual components of the instruments, which during the data gathering period used in this work were facing downwards. ASIM is the first instrument designed to look for TGFs and Transient luminous events (TLEs), and consists of two instruments: 1) the Modular X- and Gamma-ray Sensor (MXGS), and 2) The Modular Multispectral Imaging Array (MMIA).

The MXGS (*Østgaard et al.*, 2019c) consists of the High-Energy Detector (HED), and the Low Energy Detector (LED). HED is made up of 12 Bismuth-Germanium-oxide (BGO) detector bars, with a photomultiplier tube (PMT) attached to each, resulting in a geometrical sensitive area of 900 cm^2 . HED has a temporal resolution of 28.7 ns, with a dead-time of $\sim 550 \text{ ns}$ for detections by the same BGO-bar, and can measure energies from 300 keV up to 30 MeV. HED is active both night and day, as long as it is outside of the South Atlantic Anomaly (SAA). LED consists of a pixelated layer of 16384 pixels made of Cadmium-Zinc-Telluride (CZT) detector crystals, spanning a 1024 cm^2 geometrical sensitive area. LED can detect energies between $\sim 20 \text{ keV}$ to 400 keV and has a time resolution of $1 \mu\text{s}$. A coded mask was placed in front of the LED, making it capable of imaging and localisation of TGFs. LED is not active during daytime, due to optical photon contamination. A summary of the HED and LED characteristics can be found in table 4.1.

Table 4.1: Summary of HED and LED characteristics

	Energy range	Sensitive Area	Temporal resolution	Active period
HED	300 keV - 30 MeV	900 cm^2	28.7 ns	All the time
LED	20 - 400 keV	1024 cm^2	$1 \mu\text{s}$	Not during daytime

The MMIA instrument (*Chanrion et al.*, 2019) consists of two cameras and three photometers, mounted with a 5 degree tilt upwards, to avoid potential obstructions from other payloads lower on the mounting platform of the ISS. The cameras operate in the 337 nm (blue) and 777 nm (red) bands, with a bandwidth of 5 and 3 nm respectively. The cameras have a $400 \times 400 \text{ m}$ resolution at nadir, and can capture up to 12 frames per second. The photometers operate in the 180-230 nm (UV), 337 nm (4 nm bandwidth) and 777 nm (5 nm bandwidth) bands. The UV photometer has a circular FoV, with a 80° diameter, while the 337 nm and 777 nm photometers and cameras have 80° diagonal square FoVs. The 337 nm band is mostly associated with streamer activity, and is caused by radiation from the N_2 second positive band, excited by supra-thermal electrons. The 777 nm band is associated with the existence of atomic oxygen (OI), which is created from dissociation of O_2 when the lightning leader heats up. The 180-230 nm UV band is heavily absorbed in the atmosphere, and is therefore mostly observed in association with high-altitude TLEs such as Elves. Slight hints of UV light can sometimes be picked up in the 337 nm band as well. The MMIA instrument is only active during night time, as to prevent damage by sunlight. Table 4.2 shows a summary of

some of the MMIA camera and photometer characteristics. The ASIM instrument is built with a cross-triggering system between the two instruments, so that if either triggers, data from both instruments will be kept for a period of ± 1 second with respect to the trigger time. The relative timing accuracy between the MMIA and MXGS instrument was originally $\pm 80 \mu\text{s}$, but was improved to $\pm 5 \mu\text{s}$ after a software patch in April 2019. The absolute timing accuracy of ASIM varies between -10 to $+40$ ms, due to the lack of a dedicated GPS and a non-optimal interface to the Columbus module on the ISS. However, the absolute timing accuracy can be improved to ± 1 ms by aligning optical pulses detected by MMIA with lightning radio atmospheric (*Bjørge-Engeland et al., 2022; Heumesser et al., 2021; Maiorana et al., 2021; Skeie et al., 2022* In review).

Table 4.2: Summary of Camera and photometer characteristics

	Band/bandwidth [nm]	Temporal resolution	FoV
Camera 1 (blue)	337/5	>83 ms	Square (80° diagonal)
Camera 2 (red)	777.4/3	>83 ms	Square (80° diagonal)
Photometer 1 (blue)	337/4	10 μs	Square (80° diagonal)
Photometer 2 (UV)	180-230	10 μs	Circular (80° diameter)
Photometer 3 (red)	777.4/5	10 μs	Square (80° diagonal)



Figure 4.6: Picture of the ASIM instrument, after it was moved in 2022. The previous location was on the platform to the right, pointing downwards. The MXGS is behind the reflective square, and the MMIA is seen on the right, consisting of the 3 photometers (three circles towards the bottom of the picture) and 2 cameras (two circles above the other three). Image from <https://asim.dk/images.php>, visited 20.05.2022

Since the start of operations in 2018, ASIM has detected more than a thousand TGFs, hundreds of which have associated optical data. Figure 4.7 shows a TGF observed by the MXGS instrument of ASIM. In panel a) the coloured dots show HED data, where each colour correspond to a different BGO bar. Channel 1000 corresponds approximately to 10 MeV photon energies. The smaller yellow circles mark the events termed "fast" events, which are events sitting on top of the tail of a previous event. The

smaller black circles without filling show LED data, where channel 1000 corresponds to ~ 300 keV. A small tail of LED counts can be seen after the main bulk of the TGF, caused by compton scattering. Panel b) shows histograms of the number of photons detected by HED (blue) and LED (orange) in $10 \mu\text{s}$ bins. This event is considered a long TGF, lasting $\sim 400 \mu\text{s}$. Figure 4.8 shows the same TGF as in Figure 4.7, with accompanying optical data. As seen in both 337 nm and 777 nm bands, the optical pulse appears after the onset of the TGF. This event, as well as 71 more like it, are the focus of *Skeie et al. (2022 In review)*, in which the order of TGF and optical signal is addressed, as well as the relationship between the duration of TGFs and the time separation between onset of TGF and optical pulse.

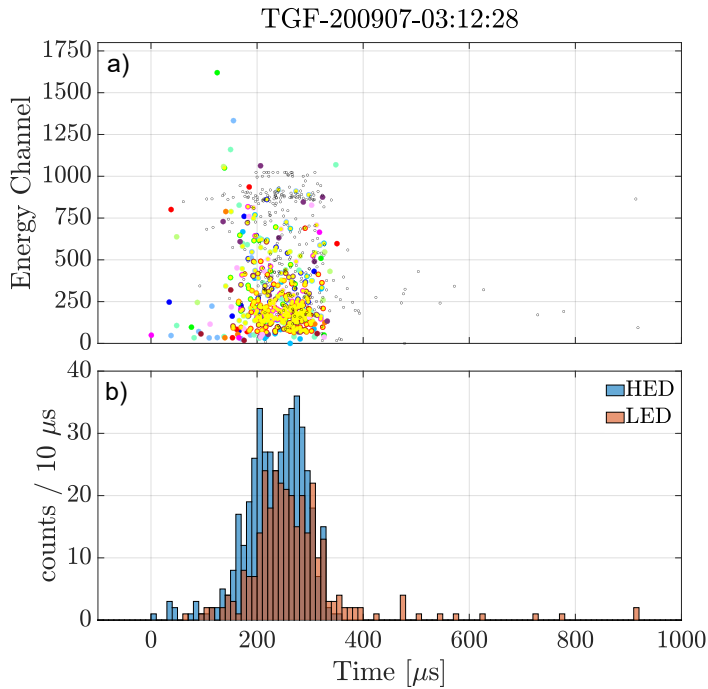


Figure 4.7: Plot showing the energy measurement of an ASIM detected TGF. The filled coloured circles are from the HED instrument, while the smaller unfilled black circles are from the LED instrument. Event from *Skeie et al. (2022 In review)*.

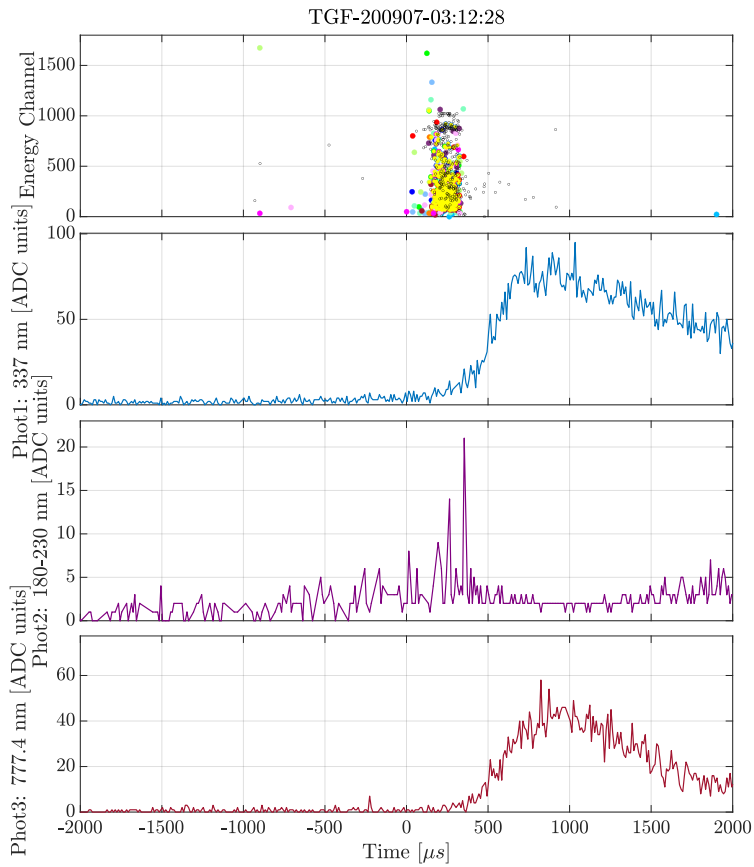


Figure 4.8: Plot showing MXGS and MMIA data of an ASIM detected TGF. a) Shows the energy channels of the detected photons by HED and LED. Panels b) to d) shows the photometer data of the 337, 180-230, and 777 nm bands. Event from Skeie et al. (2022 In review).

Chapter 5

Introduction to the papers

Paper I: Constraints on Recoil Leader Properties Estimated from X-ray Emissions in Aircraft-triggered Discharges

C. A. Skeie, N. Østgaard, N. G. Lehtinen, D. Sarria, P. Kochkin, A. I. de Boer, M. Bardet, C. Allasia, F. Flourens (2020), Journal of Geophysical Research: Atmospheres, 125(14)

The first paper, (Skeie *et al.*, 2020), reports observations of X-ray bursts associated with recoil events during aircraft triggered lightning. In it, the X-ray observations are used to define a constraint on recoil leader properties such as leader length and distance between recoil leader and aircraft. Over 120 aircraft triggered lightning strikes were observed during multiple aircraft campaigns over Southern Europe and Northern Australia in 2014-2016. 54 recoil events were found to be associated with bursts of high-energy X-rays, where the majority of bursts consisted of 1-3 X-ray pulses, but bursts up to 29 X-ray pulses were also observed. The recoil events were all accompanied by large, sudden changes in the measured local electric field on board the aircraft, and large, long-lasting current pulses through the aircraft. A total of 245 X-ray pulses were observed during the bursts, where 175 pulses were detected before the current pulses were observed. The pulses observed after the current pulses are believed to be produced by the change in surface potential at sharper extremities of the aircraft, and not by the recoil leaders. The observed X-ray pulses had energies up to 500 keV. This is a real cutoff, since the onboard high-energy detectors can measure up to 10 MeV.

By using 3 different consecutive models, where the results of each model are used as input or as a constraint of the next, we constrain some properties of the recoil leaders. Model 1) is a GEANT4 model where 20 keV seed electrons were accelerated over 10 cm length in different electric fields. This model showed that most electrons were accelerated to the full potential over the 10 cm distance, and as such, these accelerated electrons were used as a source of the observed X-ray pulses in the next model. Model 2) is a GEANT4 model of the detector and aircraft was used to model the X-ray spectra of the differently accelerated electrons from the first GEANT4 model. The different spectra were then compared to the observed superposed spectrum of observed X-ray pulses, and the best fits were determined using a Pearson χ^2 and a likelihood analysis as outlined in *Mailyan et al.* (2016). This determined the most likely potentials for

the production of the observed X-rays. 3) A model of the electric field, potential and charge transfer between the negative recoil leader and the aircraft was created, using the method of moments, as described in *Harrington (1993)*; *Lehtinen (2020)*; *Skeltved et al. (2017)*. Using gap lengths and potentials from the method of moments model, it was possible to determine a solution space for the gap and recoil leader lengths, which were limited by the potentials found in the second GEANT4 model, as well as the observed minimum and maximum times between onsets of the X-ray bursts and current pulses. The result showed that the recoil leaders are between 1 and ~ 240 m long, with gap lengths (distance between recoil leader and aircraft) of 1 to 93 m.

Paper II: Production of Terrestrial Gamma-ray Flashes During the Early Stages of Lightning Flashes

A. Lindanger, C. A. Skeie, M. Marisaldi, I. Bjørge-Engeland, N. Østgaard, A. Mezentsev, V. Reglero, O. Chanrion, T. Neubert (2022), Journal of Geophysical Research: Atmospheres, 127(8)

The second paper, *Lindanger et al. (2022)*, investigates the time of the TGF in relation to the lightning flash. A typical lightning flash lasts a few hundred milliseconds and consists of multiple discharges, which can all create detectable radio atmospherics. This work finds that the TGFs are typically associated with both lightning activity and optical measurements in the beginning of lightning flashes. This is done using two methods, where the first relies on TGF observations from AGILE, Fermi, RHESSI, and ASIM paired with lightning radio atmospherics close in time to the TGFs. The second method uses ASIM detected TGFs with optical emissions, where the TGFs are determined to be from within the MMIA photometer (337 and 777 nm) FoV.

The results show an excess of lightning radio atmospherics are detected between 150 to 750 ms after the TGF, which is termed "second peak", in agreement with the findings of *Smith et al. (2016)*. The TGF sample shows a quick decay of lightning activity after the first stroke associated with the TGF, before the activity increases forming a second peak. The lightning radio atmospherics produced during this second peak are shown to be located at the production location of the TGFs, within the uncertainties of the lightning atmospheric detection networks. The analysis shows that an average of 13% of TGFs which have an associated WWLLN radio atmospheric also have a WWLLN detection in the second peak interval. This is further increased to 51% for TGFs associated with a GLD360 radio spheric association. The peak currents from the closest radio atmospherics in time around the TGFs are found to be larger than those of the second peak. Random lightning data were then used to perform a blind search, investigating if the second peak is a general characteristic of lightning flashes. The random sample found no signs of this phenomena, and shows a gradual decay of radio atmospherics without any secondary peak, whichever selection in peak current and polarity is chosen. This could indicate that the flashes which are associated with TGFs have large initial discharges, and need more time before the electric activity can start up again. It is also shown that TGFs observed by ASIM appear together with the first optical signals of lightning flashes, which is confirmed using the on board photometers and optical cameras, as well as location information from radio atmospherics when

available.

Paper III: The temporal relationship between Terrestrial Gamma-ray flashes and associated optical pulses from lightning

C. A. Skeie, N. Østgaard, A. Mezentssev, I. Bjørge-Engeland, M. Marisaldi, N. Lehtinen, V. Reglero, T. Neubert (2022), Journal of Geophysical Research: Atmospheres - in review,

The third paper, *Skeie et al. (2022 In review)*, uses ASIM data of TGFs with accompanying optical data to investigate the temporal relationship between TGFs and associated optical pulses. The work investigates 221 TGFs with accompanying optical data, from a period with relative uncertainty between the instruments of 5 μs . By applying a consistency check based on TGF characteristics, such as fluence and photon energies, as well as surrounding lightning detections, we determine if the TGFs are likely to be inside the MMIA photometer (337 and 777 nm) FoV. The consistency check builds on the assumption that the TGF fluence is reduced as the distance between the TGF and ISS footpoint increases, due to scattering of photons in the atmosphere. Based on a TGF production cone of 30-40° as suggested by previous studies, we expect the TGFs detected within the MMIA FoV to have more high energy photons. This is due to the TGFs more likely being observed from within the production cone, which is similar in its opening to the MMIA FoV (40° diagonal angle). As the TGFs are observed from within the production cone, they will have undergone less Compton scattering, therefore having higher energies (*Carlson et al., 2007; Gjesteland et al., 2011; Lindanger et al., 2021*). The lightning activity surrounding the TGF is also investigated, and can in some instances be associated to certain optical pulses, by aligning the radio signals to the optical pulses of MMIA. Using the aligned radio atmospherics we determine the absolute timing accuracy to be between -11.5 to $+40$ ms, which is improved to ± 1 ms for the events where we can make alignments between radio atmospherics and optical pulses.

Out of the starting 221 events, we determine that there are 72 events where the TGF is most likely inside the MMIA FoV and associated to the observed optical pulse. The sequence of TGF and optical pulse, as well as the connection between TGF duration and time between onset of TGF and optical pulse is then addressed using this sample. It is found that all events have TGF onsets before the onset of the optical pulses. By assuming a typical delay of observed optical onset due to cloud scattering of 100 μs (based on a uniform cloud with particle radius 10 μm and particle density of 100 cm^{-3} (*Luque et al., 2020*)), it is found that $\sim 51\%$ of the events have TGF onset before or simultaneously with the optical onset, where some of these events could have optical onsets before the TGFs end. 21% of the events have longer delays than can be explained by cloud scattering (even at extreme values), which points to the TGFs ending before a large current surge in the leader initiates. It is also found that longer duration TGFs show a tendency to have longer delays between the onset of TGFs and optical pulses.

Chapter 6

Conclusions

The goal of the work in this thesis has been to investigate and improve our understanding of high-energy radiation phenomena associated with lightning leaders, which has been done using both instruments on aircraft and spacecraft.

Paper I presents observations of X-ray emissions associated with recoil processes during aircraft-triggered lightning flashes. The X-ray observations are consistent with previous observations, regarding energy and duration. A model of the acceleration of electrons over short distances show that all electrons are accelerated to the full potential. From the second model we find that the most likely source potential is between 1000 to 3500 kV, with a best fit for 1500 kV. Using these potentials as minimum and maximum, together with the determined potentials between leader and aircraft for different leader lengths, we find that the lightning leaders are between 1 and 240 meters, (assuming a recoil leader speed of 10^7 m/s, and that the gap between X-ray source of the leader and aircraft is most likely between 1 and 93 meters.

Paper I is to my knowledge the only paper using observations of X-rays from recoil processes to constrain the properties of the lightning leader. The work uses the IL-DAS instruments on board an Airbus aircraft, which is one of the few modern aircraft campaigns that studies lightning and thundercloud environments. A side goal of using ILDAS data was to look into and investigate aircraft charge-control strategies. For this purpose external electric field mills would have been a good addition to the instrument package, making ILDAS capable of mapping the external electric fields of the thunderclouds, while observing the associated effects on the aircraft. Another challenge is that the local electric field capacitive probe onboard the aircraft is time differentiated, and we do not know the total charge accumulated at any given time. At present times, aircraft that have initiated or intercepted a lightning flash have to undergo rigorous inspection to check for any potential damage, this is both time-consuming and expensive. Therefore a charge control strategy, where the number of aircraft incidents caused by lightning are minimised, as well as where the attachment locations could be identified without the need of large amounts of scientific instruments, would be a huge step forwards. Although the radiation observed from recoil leaders is not considered particularly dangerous to passengers, a lightning strike to the aircraft has the potential to cause expensive damage or even accidents, although rarely. Therefore, improving our knowledge of the interaction between aircraft and the electric field of thunderclouds can only help to improve flight safety.

Paper II uses radio and optical measurements together with TGF detections to in-

investigate when in the lightning flash the TGF is observed. Based on a large sample of TGFs from different instruments, with sferic data, and for a smaller sample of TGFs, optical data, the study finds that the TGFs are produced in the beginning of the lightning flashes. An excess of sferics are detected between 150 and 750 ms after the observations of TGFs, which were found to be from a location compatible with that of the TGF. The fraction of TGFs with radio signals in this time period was found to be dependent on the sensitivity of the lightning detection network. As such, only by stacking the TGFs is the peak of sferics found in this time period after the TGF. A blind search using randomised data does not show such a sferic peak, indicating that the second peak is likely tied to the characteristics of lightning which are associated to TGFs.

Paper III further investigates the relationship between the TGFs and lightning. A sample of TGFs with accompanying optical measurements by ASIM is used to determine the sequence of TGF and optical pulse, as well as the relationship between the TGF duration and delay between onset of TGF and optical signal. We group the events of the sample by using a novel method to determine whether the TGF is most likely inside or outside the photometer FoV. Using the events determined to be inside the MMIA FoV, we find that all observed TGFs have onsets before the onset of the optical pulse. Taking into account a typical delay of optical light due to cloud scattering of 100 μs (Luque *et al.*, 2020), we find that $\sim 51\%$ of the events have TGF onsets before or at the same time of the onset of the optical pulse. A further 28% of the events fit with this scenario if the delay due to cloud scattering is increased to 200 μs , which is a bit extreme. 21% of the events are found to have delays which are longer than what can be explained by cloud scattering, where the TGFs end before the leader current occurs. It is also found that longer-duration TGFs tend to have longer delays between the onsets.

Both Paper II and III use data from ASIM, which is the first mission designed specifically to observe TGFs, as well as optical signals associated with lightning and TLEs. Having both optical and high-energy detections from the same instrument has been an enormous asset, and has been important to minimise the relative timing uncertainties in the comparison and association of detected events. Good absolute timing accuracy is also fundamental when considering the sequence of events. Due to a non-optimal interface between ASIM and the Columbus module on the ISS, and the lack of a dedicated GPS, the ASIM instrument did not achieve the full potential for absolute timing accuracy. This led us to use sferics to improve the absolute timing for the events where that was possible. A dedicated GPS or clock would have been a great help for the work done in both papers II and III, and should therefore be considered by all future missions. Paper III is the first paper to show that there are no TGF onsets observed after the onset of the optical pulses. This has been ambiguous in previous works, in part due to the problems with absolute timing.

Bibliography

- Abbasi, R. U., T. Abu-Zayyad, M. Allen, E. Barcikowski, J. W. Belz, D. R. Bergman, S. A. Blake, M. Byrne, R. Cady, B. Cheon, J. Chiba, M. Chikawa, T. Fujii, M. Fukushima, G. Furlich, T. Goto, W. Hanlon, Y. Hayashi, N. Hayashida, K. Hibino, K. Honda, D. Ikeda, N. Inoue, T. Ishii, H. Ito, D. Ivanov, S. Jeong, C. C. H. Jui, K. Kadota, F. Kakimoto, O. Kalashev, K. Kasahara, H. Kawai, S. Kawakami, K. Kawata, E. Kido, H. B. Kim, J. H. Kim, J. H. Kim, S. S. Kishigami, P. R. Krehbiel, V. Kuzmin, Y. J. Kwon, J. Lan, R. LeVon, J. P. Lundquist, K. Machida, K. Martens, T. Matuyama, J. N. Matthews, M. Minamino, K. Mukai, I. Myers, S. Nagataki, R. Nakamura, T. Nakamura, T. Nonaka, S. Ogio, M. Ohnishi, H. Ohoka, K. Oki, T. Okuda, M. Ono, R. Onogi, A. Oshima, S. Ozawa, I. H. Park, M. S. Pshirkov, J. Remington, W. Rison, D. Rodeheffer, D. C. Rodriguez, G. Rubtsov, D. Ryu, H. Sagawa, K. Saito, N. Sakaki, N. Sakurai, T. Seki, K. Sekino, P. Shah, F. Shibata, T. Shibata, H. Shimodaira, B. K. Shin, H. S. Shin, J. D. Smith, P. Sokolsky, R. W. Springer, B. T. Stokes, T. A. Stroman, H. Takai, M. Takeda, R. Takeishi, A. Taketa, M. Takita, Y. Tameda, H. Tanaka, K. Tanaka, M. Tanaka, R. J. Thomas, S. B. Thomas, G. B. Thomson, P. Tinyakov, I. Tkachev, H. Tokuno, T. Tomida, S. Troitsky, Y. Tsunesada, Y. Uchihori, S. Udo, F. Urban, G. Vasiloff, T. Wong, M. Yamamoto, R. Yamane, H. Yamaoka, K. Yamazaki, J. Yang, K. Yashiro, Y. Yoneda, S. Yoshida, H. Yoshii, and Z. Zundel (2018), Gamma ray showers observed at ground level in coincidence with downward lightning leaders, *Journal of Geophysical Research: Atmospheres*, 123(13), 6864–6879, doi:<https://doi.org/10.1029/2017JD027931>. 4.2
- Babich, L. P., E. N. Donskoy, R. I. Il'kaev, I. M. Kutsyk, and R. A. Roussel-Dupre (2004), Fundamental parameters of a relativistic runaway electron avalanche in air, *Plasma Physics Reports*, 30(7), 616–624, doi:[10.1134/1.1778437](https://doi.org/10.1134/1.1778437). 4.2.1
- Babich, L. P., E. I. Bochkov, E. N. Donskoi, and I. M. Kutsyk (2010), Source of prolonged bursts of high-energy gamma rays detected in thunderstorm atmosphere in japan at the coastal area of the sea of japan and on high mountaintop, *Journal of Geophysical Research: Space Physics*, 115(A9), doi:<https://doi.org/10.1029/2009JA015017>. 1
- Bazelyan, E., and Y. Raizer (2000), *Lightning Physics and Lightning Protection*, IOP Publishing. 2.2.3
- Biagi, C. J., M. A. Uman, J. D. Hill, D. M. Jordan, V. A. Rakov, and J. Dwyer (2010), Observations of stepping mechanisms in a rocket-and-wire triggered lightning flash, *Journal of Geophysical Research: Atmospheres*, 115(D23), doi:<https://doi.org/10.1029/2010JD014616>. 2.2.3

- Bjørge-Engeland, I., N. Østgaard, A. Mezentsev, C. A. Skeie, D. Sarria, J. Lapierre, A. Lindanger, T. Neubert, M. Marisaldi, O. Chanrion, K. Ullaland, S. Yang, G. Genov, F. Christiansen, and V. Reglero (2022), Terrestrial gamma-ray flashes with accompanying elves, detected by asim, *Journal of Geophysical Research: Atmospheres*, p. e2021JD036368, doi:10.1029/2021JD036368. 4.2.4
- Boissin, J., F. Flourens, A. de Boer, M. Bardet, A. Herve, G. Perez, and L. Riccio (2012), In-flight lightning measurements and reconstruction on a metallic and composite aircraft, may 2012 esa workshop on aerospace emc. 4.1.3
- Bowers, G. S., D. M. Smith, N. A. Kelley, G. F. Martinez-McKinney, S. A. Cummer, J. R. Dwyer, S. Heckman, R. H. Holzworth, F. Marks, P. Reasor, J. Gamache, J. Dunion, T. Richards, and H. K. Rassoul (2018), A terrestrial gamma-ray flash inside the eyewall of hurricane patricia, *Journal of Geophysical Research: Atmospheres*, 123(10), 4977–4987, doi:https://doi.org/10.1029/2017JD027771. 4.2
- Briggs, M. S., G. J. Fishman, V. Connaughton, P. N. Bhat, W. S. Paciasas, R. D. Preece, C. Wilson-Hodge, V. L. Chaplin, R. M. Kippen, A. von Kienlin, C. A. Meegan, E. Bissaldi, J. R. Dwyer, D. M. Smith, R. H. Holzworth, J. E. Grove, and A. Chekhtman (2010), First results on terrestrial gamma ray flashes from the fermi gamma-ray burst monitor, *Journal of Geophysical Research: Space Physics*, 115(A7), doi:https://doi.org/10.1029/2009JA015242. 4.2.3
- Briggs, M. S., S. Xiong, V. Connaughton, D. Tierney, G. Fitzpatrick, S. Foley, J. E. Grove, A. Chekhtman, M. Gibby, G. J. Fishman, S. McBreen, V. L. Chaplin, S. Guiriec, E. Layden, P. N. Bhat, M. Hughes, J. Greiner, A. von Kienlin, R. M. Kippen, C. A. Meegan, W. S. Paciasas, R. D. Preece, C. Wilson-Hodge, R. H. Holzworth, and M. L. Hutchins (2013), Terrestrial gamma-ray flashes in the fermi era: Improved observations and analysis methods, *Journal of Geophysical Research: Space Physics*, 118(6), 3805–3830, doi:https://doi.org/10.1002/jgra.50205. 4.2
- Brunetti, M., S. Cecchini, M. Galli, G. Giovannini, and A. Pagliarin (2000), Gamma-ray bursts of atmospheric origin in the mev energy range, *Geophysical Research Letters*, 27(11), 1599–1602, doi:https://doi.org/10.1029/2000GL003750. 1
- Carlson, B. E., N. G. Lehtinen, and U. S. Inan (2007), Constraints on terrestrial gamma ray flash production from satellite observation, *Geophysical Research Letters*, 34(8), doi:https://doi.org/10.1029/2006GL029229. 1, 4.2.3, 5
- Celestin, S., and V. P. Pasko (2011), Energy and fluxes of thermal runaway electrons produced by exponential growth of streamers during the stepping of lightning leaders and in transient luminous events, *Journal of Geophysical Research: Space Physics*, 116(A3), doi:https://doi.org/10.1029/2010JA016260. 1, 4.2.1
- Celestin, S., W. Xu, and V. P. Pasko (2015), Variability in fluence and spectrum of high-energy photon bursts produced by lightning leaders, *Journal of Geophysical Research: Space Physics*, 120(12), 10,712–10,723, doi:https://doi.org/10.1002/2015JA021410. 4.2.3
- Cember, H., and T. Johnson (2009), *Introduction to Health Physics*, McGraw-Hill. 4

- Chanrion, O., T. Neubert, R. Lundgaard, C. Stoltze, D. Tcherniak, N. Jessen, J. Polny, P. Brauer, J. Balling, S. Savstrup Kristensen, S. Forchhammer, P. Hofmeyer, P. David-
sen, O. Mikkelsen, D. Bo Hansen, D. Bhanderi, C. Petersen, and M. Lorenzen (2019),
The modular multispectral imaging array (mmia) of the asim payload on the interna-
tional space station, *Space Science Reviews*, 215, doi:10.1007/s11214-019-0593-y.
2.2.2, 2.2.3, 4.2.4
- Chilingarian, A., A. Daryan, K. Arakelyan, A. Hovhannisyanyan, B. Mailyan,
L. Melkumyan, G. Hovsepyan, S. Chilingaryan, A. Reymers, and L. Vanyan (2010),
Ground-based observations of thunderstorm-correlated fluxes of high-energy elec-
trons, gamma rays, and neutrons, *Phys. Rev. D*, 82, 043,009, doi:10.1103/PhysRevD.
82.043009. 1
- Chubenko, A., V. Antonova, S. Kryukov, V. Piskal, M. Ptitsyn, A. Shepetov, L. Vil-
danova, K. Zybin, and A. Gurevich (2000), Intensive x-ray emission bursts dur-
ing thunderstorms, *Physics Letters A*, 275(1), 90–100, doi:https://doi.org/10.1016/
S0375-9601(00)00502-8. 1
- Connaughton, V., M. S. Briggs, R. H. Holzworth, M. L. Hutchins, G. J. Fishman,
C. A. Wilson-Hodge, V. L. Chaplin, P. N. Bhat, J. Greiner, A. von Kienlin, R. M.
Kippen, C. A. Meegan, W. S. Paciesas, R. D. Preece, E. Cramer, J. R. Dwyer,
and D. M. Smith (2010), Associations between fermi gamma-ray burst monitor
terrestrial gamma ray flashes and sferics from the world wide lightning location
network, *Journal of Geophysical Research: Space Physics*, 115(A12), doi:https:
//doi.org/10.1029/2010JA015681. 4.2.2
- Cooray, V. (2004), *The Lightning Flash*, The Institution of Engineering and Technol-
ogy, London, United Kingdom. 2.1, 2.2.3
- Cummer, S. A., M. S. Briggs, J. R. Dwyer, S. Xiong, V. Connaughton, G. J. Fish-
man, G. Lu, F. Lyu, and R. Solanki (2014), The source altitude, electric current, and
intrinsic brightness of terrestrial gamma ray flashes, *Geophysical Research Letters*,
41(23), 8586–8593, doi:https://doi.org/10.1002/2014GL062196. 1, 4.2.3
- Cummer, S. A., F. Lyu, M. S. Briggs, G. Fitzpatrick, O. J. Roberts, and J. R.
Dwyer (2015), Lightning leader altitude progression in terrestrial gamma-ray
flashes, *Geophysical Research Letters*, 42(18), 7792–7798, doi:https://doi.org/10.
1002/2015GL065228. 1, 4.2.2
- de Boer, A., M. Bardet, C. Escure, G. Peres, V. Srithammavanh, K. Abboud, T. Abboud,
J. Boissin, F. Flourens, T. Vorreux, and L. a. Riccio (2011), In-flight lightning damage
assessment system (ILDAS): Initial in-flight lightning tests and improvement of the
numerical methods, in *Proceedings of the International Conference On Lightning
and Static Electricity 2011 (ICOLSE 2011)*, 6-8 September 2011, Oxford, UK. 4.1.3
- de Boer, A., J. Boissin, A. van Deursen, F. Flourens, A. Herve, and R. Zwemmer
(2013a), In-flight lightning damage assessment system (ILDAS) : in-flight verifica-
tion of multi-sensor measurement, in *Proceedings of the 2013 International Confer-
ence on Lightning and Static Electricity (ICOLSE)*, 18-20 September 2013, Seattle,
Washington. 4.1.3

- de Boer, A., M. Bardet, J. Boissin, A. van Deursen, F. Flourens, and A. Herve (2013b), In-flight lightning damage assessment system (ILDAS): Further in-flight verification, with multi-sensor configuration., in *Proceedings of the 2013 International Conference on Lightning and Static Electricity (ICOLSE), 18-20 September 2013, Seattle, Washington*. 4.1.3
- de Boer, A., F. Flourens, A. Hervé, M. Bardet, and J. Boissin (2015), ILDAS2: From the laboratory to operations - benefits and performance of the in-flight lightning damage assessment system in support of flight test campaigns. 4.1.3
- Demetriades, N., H. Pohjola, M. Murphy, and J. Cramer (2010), Validation of vaisalas global lightning dataset (gld360), *Conference paper: Technical Conference on Meteorological and Environmental Instruments and Methods of Observation*. 2.2.5
- Dowden, R. L., J. B. Brundell, and C. J. Rodger (2002), Vlf lightning location by time of group arrival (toga) at multiple sites, *Journal of Atmospheric and Solar-Terrestrial Physics*, 64(7), 817–830, doi:[https://doi.org/10.1016/S1364-6826\(02\)00085-8](https://doi.org/10.1016/S1364-6826(02)00085-8). 2.2.5, 2.2.5
- Dubinova, A. A. (2016), *Modeling of streamer discharges near dielectrics*, Technische Universiteit Eindhoven. 2.3
- Dwyer, J. (2004), Implications of X-ray emission from lightning, *Geophysical Research Letters*, 31(12), L12,102, doi:[10.1029/2004GL019795](https://doi.org/10.1029/2004GL019795). 4.1
- Dwyer, J., H. Rassoul, M. Al-Dayeh, L. Caraway, B. Wright, and A. Chrest (2004), Measurements of X-ray emission from rocket-triggered lightning, *Geophysical Research Letters*, 31(5), doi:[10.1029/2003GL018770](https://doi.org/10.1029/2003GL018770). 1, 4.1, 4.2
- Dwyer, J., H. Rassoul, M. Al-Dayeh, L. Caraway, A. Chrest, B. Wright, and E. Kozak (2005), X-ray bursts associated with leader steps in cloud-to-ground lightning, *Geophysical Research Letters*, 32(1), 1–4, doi:[10.1029/2004GL021782](https://doi.org/10.1029/2004GL021782). 1, 4.1, 4.1.1
- Dwyer, J., M. Schaal, H. Rassoul, M. Uman, D. Jordan, and D. Hill (2011), High-speed X-ray images of triggered lightning dart leader, *Journal of Geophysical Research Atmospheres*, 116(20), doi:[10.1029/2011JD015973](https://doi.org/10.1029/2011JD015973). 4.1
- Dwyer, J. R. (2003), A fundamental limit on electric fields in air, *Geophysical Research Letters*, 30(20), doi:<https://doi.org/10.1029/2003GL017781>. 1, 4.2.1, 4.2.1
- Dwyer, J. R. (2008), Source mechanisms of terrestrial gamma-ray flashes, *Journal of Geophysical Research: Atmospheres*, 113(D10), doi:<https://doi.org/10.1029/2007JD009248>. 4.2.1
- Dwyer, J. R., and D. M. Smith (2005), A comparison between monte carlo simulations of runaway breakdown and terrestrial gamma-ray flash observations, *Geophysical Research Letters*, 32(22), doi:<https://doi.org/10.1029/2005GL023848>. 1, 4.2.1, 4.2.3
- Dwyer, J. R., M. A. Uman, H. K. Rassoul, M. Al-Dayeh, L. Caraway, J. Jerauld, V. A. Rakov, D. M. Jordan, K. J. Rambo, V. Corbin, and B. Wright (2003), Energetic radiation produced during rocket-triggered lightning, *Science*, 299(5607), 694–697, doi:[10.1126/science.1078940](https://doi.org/10.1126/science.1078940). 4.1

- Dwyer, J. R., M. M. Schaal, E. Cramer, S. Arabshahi, N. Liu, H. K. Rassoul, J. D. Hill, D. M. Jordan, and M. A. Uman (2012a), Observation of a gamma-ray flash at ground level in association with a cloud-to-ground lightning return stroke, *Journal of Geophysical Research: Space Physics*, 117(A10), doi:<https://doi.org/10.1029/2012JA017810>. 4.2
- Dwyer, J. R., D. M. Smith, and S. Cummer (2012b), High-energy atmospheric physics: Terrestrial gamma-ray flashes and related phenomena, *Space Science Reviews*, 173, 133–196, doi:[10.1007/s11214-012-9894-0](https://doi.org/10.1007/s11214-012-9894-0). 4.5, 4.2.3
- Eack, K. B., W. H. Beasley, W. D. Rust, T. C. Marshall, and M. Stolzenburg (1996a), Initial results from simultaneous observation of x-rays and electric fields in a thunderstorm, *Journal of Geophysical Research: Atmospheres*, 101(D23), 29,637–29,640, doi:<https://doi.org/10.1029/96JD01705>. 1
- Eack, K. B., W. H. Beasley, W. D. Rust, T. C. Marshall, and M. Stolzenburg (1996b), X-ray pulses observed above a mesoscale convective system, *Geophysical Research Letters*, 23(21), 2915–2918, doi:<https://doi.org/10.1029/96GL02570>. 1
- Eack, K. B., D. M. Suszcynsky, W. H. Beasley, R. Roussel-Dupre, and E. Symbal-isty (2000), Gamma-ray emissions observed in a thunderstorm anvil, *Geophysical Research Letters*, 27(2), 185–188, doi:<https://doi.org/10.1029/1999GL010849>. 1
- Fisher, B., P. Brown, J. Plumer, and A. Wunschel Jr. (1988), Final results of the NASA storm hazards program, *Conference paper*. 3, 4.1
- Fisher, F., J. Plumer, and R. Perala (1977), Lightning protection of aircraft, *NASA Reference Publication*, (1008). 3, 3.1
- Fishman, G. J., P. N. Bhat, R. Mallozzi, J. M. Horack, T. Koshut, C. Kouveliotou, G. N. Pendleton, C. A. Meegan, R. B. Wilson, W. S. Paciesas, S. J. Goodman, and H. J. Christian (1994), Discovery of intense gamma-ray flashes of atmospheric origin, *Science*, 264(5163), 1313–1316, doi:[10.1126/science.264.5163.1313](https://doi.org/10.1126/science.264.5163.1313). 1, 4.2, 4.2.2, 4.2.3
- Foley, S., G. Fitzpatrick, M. S. Briggs, V. Connaughton, D. Tierney, S. McBreen, J. R. Dwyer, V. L. Chaplin, P. N. Bhat, D. Byrne, E. Cramer, G. J. Fishman, S. Xiong, J. Greiner, R. M. Kippen, C. A. Meegan, W. S. Paciesas, R. D. Preece, A. von Kienlin, and C. Wilson-Hodge (2014), Pulse properties of terrestrial gamma-ray flashes detected by the fermi gamma-ray burst monitor, *Journal of Geophysical Research: Space Physics*, 119(7), 5931–5942, doi:<https://doi.org/10.1002/2014JA019805>. 4.2.3
- Gallimberti, I., G. Bacchiega, A. Bondiou-Clergerie, and P. Lalande (2002), Fundamental processes in long air gap discharges, *Comptes Rendus Physique*, 3(10), 1335–1359, doi:[https://doi.org/10.1016/S1631-0705\(02\)01414-7](https://doi.org/10.1016/S1631-0705(02)01414-7). 2.2.3
- Gjesteland, T., N. Østgaard, P. H. Connell, J. Stadsnes, and G. J. Fishman (2010), Effects of dead time losses on terrestrial gamma ray flash measurements with the burst and transient source experiment, *Journal of Geophysical Research: Space Physics*, 115(A5), doi:<https://doi.org/10.1029/2009JA014578>. 4.2.3

- Gjesteland, T., N. Østgaard, A. B. Collier, B. E. Carlson, M. B. Cohen, and N. G. Lehtinen (2011), Confining the angular distribution of terrestrial gamma ray flash emission, *Journal of Geophysical Research: Space Physics*, 116(A11), doi:<https://doi.org/10.1029/2011JA016716>. 4.2.3, 5
- Gjesteland, T., N. Østgaard, P. Bitzer, and H. Christian (2017), On the timing between terrestrial gamma ray flashes, radio atmospherics, and optical lightning emission, *Journal of Geophysical Research: Space Physics*, 112(7), doi:[10.1002/2017JA024285](https://doi.org/10.1002/2017JA024285). 4.2.2
- Gorin, B., V. Levitov, and A. Shkilev (1976), *Some principles of leader discharge of air gaps with a strong non-uniform field*, vol. 143, 274-279 pp., Institution of Electrical Engineers. 2.2.3, 2.2.3, 2.4
- Grefenstette, B. W., D. M. Smith, J. R. Dwyer, and G. J. Fishman (2008), Time evolution of terrestrial gamma ray flashes, *Geophysical Research Letters*, 35(6), doi:<https://doi.org/10.1029/2007GL032922>. 4.2.3
- Grefenstette, B. W., D. M. Smith, B. J. Hazelton, and L. I. Lopez (2009), First rhesi terrestrial gamma ray flash catalog, *Journal of Geophysical Research: Space Physics*, 114(A2), doi:<https://doi.org/10.1029/2008JA013721>. 4.2, 4.2.3
- Gurevich, A., G. Milikh, and R. Roussel-Dupre (1992), Runaway electron mechanism of air breakdown and preconditioning during a thunderstorm, *Physics Letters A*, 165(5), 463–468, doi:[https://doi.org/10.1016/0375-9601\(92\)90348-P](https://doi.org/10.1016/0375-9601(92)90348-P). 1, 4.2.1
- Hare, B. M., M. A. Uman, J. R. Dwyer, D. M. Jordan, M. I. Biggerstaff, J. A. Caicedo, F. L. Carvalho, R. A. Wilkes, D. A. Kotovsky, W. R. Gameraota, J. T. Pilkey, T. K. Ngin, R. C. Moore, H. K. Rassoul, S. A. Cummer, J. E. Grove, A. Nag, D. P. Betten, and A. Bozarth (2016), Ground-level observation of a terrestrial gamma ray flash initiated by a triggered lightning, *Journal of Geophysical Research: Atmospheres*, 121(11), 6511–6533, doi:<https://doi.org/10.1002/2015JD024426>. 4.2
- Harrington, R. (1993), *Field Computation by Moment Methods*, IEEE Press. 5
- Hazelton, B. J., B. W. Grefenstette, D. M. Smith, J. R. Dwyer, X.-M. Shao, S. A. Cummer, T. Chronis, E. H. Lay, and R. H. Holzworth (2009), Spectral dependence of terrestrial gamma-ray flashes on source distance, *Geophysical Research Letters*, 36(1), doi:<https://doi.org/10.1029/2008GL035906>. 1, 4.2.3
- Hervé, A., G. Peres, A. de Boer, M. Bardet, F. Flourens, and J. Boissin (2014), In-flight lightning damage assessment system (ILDAS): Diagnostic performance assessment with in-flight lightning data, in *2014 International Symposium on Electromagnetic Compatibility*, pp. 589–594, doi:[10.1109/EMCEurope.2014.6930974](https://doi.org/10.1109/EMCEurope.2014.6930974). 4.1.3
- Heumesser, M., O. Chanrion, T. Neubert, H. J. Christian, K. Dimitriadou, F. J. Gordillo-Vazquez, A. Luque, F. J. Pérez-Invernón, R. J. Blakeslee, N. Østgaard, V. Reglero, and C. Köhn (2021), Spectral observations of optical emissions associated with terrestrial gamma-ray flashes, *Geophysical Research Letters*, 48(4), doi:<https://doi.org/10.1029/2020GL090700>. 4.2.2, 4.2.4

- Howard, J., M. Uman, C. Biagi, D. Hill, J. Jerauld, V. Rakov, J. Dwyer, Z. Saleh, and H. Rassoul (2010), Rf and X-ray source locations during the lightning attachment process, *Journal of Geophysical Research Atmospheres*, 115(6), 1–25, doi:10.1029/2009JD012055. 1, 4.1
- Hutchins, M. L., R. H. Holzworth, J. B. Brundell, and C. J. Rodger (2012), Relative detection efficiency of the world wide lightning location network, *Radio Science*, 47(6), doi:https://doi.org/10.1029/2012RS005049. 2.2.5
- Jayaratne, E. R., C. P. R. Saunders, and J. Hallett (1983), Laboratory studies of the charging of soft-hail during ice crystal interactions, *Quarterly Journal of the Royal Meteorological Society*, 109(461), 609–630, doi:https://doi.org/10.1002/qj.49710946111. 2.1
- Kasemir, H. (1960), A contribution to the electrostatic theory of a lightning discharge, *Journal of Geophysical Research*, 65(7), 1873–1878. 3.1
- Kasemir, H. (2012), *Static Discharge and Triggered Lightning*, chap. 29, pp. 418–428, American Geophysical Union (AGU), doi:https://doi.org/10.1002/9781118704813.ch29. 3.1
- Kelley, N. (2014), Long duration gamma-ray emissions from thunderclouds, Ph.D. thesis, University of California, Santa Cruz, United States of America. 1
- Kochkin, P., A. P. J. van Deursen, A. de Boer, M. Bardet, and J.-F. Boissin (2015), In-flight measurements of energetic radiation from lightning and thunderclouds, *Journal of Physics D: Applied Physics*, 48(42), 425,202, doi:10.1088/0022-3727/48/42/425202. 1, 3.2.2, 4.1, 4.1.3, 4.3
- Kochkin, P., A. P. J. van Deursen, M. Marisaldi, A. Ursi, A. I. de Boer, M. Bardet, C. Allasia, J.-F. Boissin, F. Flourens, and N. Østgaard (2017), In-flight observation of gamma ray glows by ildas, *Journal of Geophysical Research: Atmospheres*, 122(23), 12,801–12,811, doi:https://doi.org/10.1002/2017JD027405. 1
- Lalande, P., A. Bondiou-Clergerie, and P. Laroche (1999), Analysis of available in-flight measurements of lightning strikes to aircraft, in *International Conference on Lightning and Static Electricity*, SAE International, doi:https://doi.org/10.4271/1999-01-2397. 3.2.2
- Laroche, P., P. Blanchet, A. Delannoy, and F. Issac (2012), Experimental studies of lightning strikes to aircraft, *Aerospace Lab Journal*, (5), 1–13. 3.2.2
- Lay, E., C. Rodger, R. Holzworth, and R. Dowden (2005), Introduction to the world wide lightning location network (wwlln), *Geophysical Research Abstracts*. 2.2.5
- Lehtinen, N. (2021), Physics and mathematics of electric streamers, *Radiophysics and Quantum Electronics*, 64(1), 11–25, doi:10.1007/s11141-021-10108-5. 2.2.2, 2.2.2, 3.1
- Lehtinen, N. G. (2020), Method of moments (MoM), https://gitlab.com/nleht/small-projects/-/tree/main/Method_of_Moments commit: 609acfb4e38b1679e414a72d5dca3f314f567102. 5

- Lehtinen, N. G., and R. Marskar (2021), What determines the parameters of a propagating streamer: A comparison of outputs of the streamer parameter model and of hydrodynamic simulations, *Atmosphere*, 12(12), doi:10.3390/atmos12121664. 3.1
- Lehtinen, N. G., M. Walt, U. S. Inan, T. F. Bell, and V. P. Pasko (1996), -ray emission produced by a relativistic beam of runaway electrons accelerated by quasi-electrostatic thundercloud fields, *Geophysical Research Letters*, 23(19), 2645–2648, doi:https://doi.org/10.1029/96GL02573. 1
- Lehtinen, N. G., and N. Østgaard (2018), X-ray emissions in a multiscale fluid model of a streamer discharge, *Journal of Geophysical Research: Atmospheres*, 123(13), 6935–6953, doi:https://doi.org/10.1029/2018JD028646. 4.2.1
- Lindanger, A., M. Marisaldi, C. Maiorana, D. Sarria, K. Albrechtsen, N. Østgaard, M. Galli, A. Ursi, C. Labanti, M. Tavani, C. Pittori, and F. Verrecchia (2020), The 3rd agile terrestrial gamma ray flash catalog. part i: Association to lightning sferics, *Journal of Geophysical Research: Atmospheres*, 125(11), e2019JD031,985, doi:https://doi.org/10.1029/2019JD031985. 4.2.2, 4.2.3
- Lindanger, A., M. Marisaldi, D. Sarria, N. Østgaard, N. Lehtinen, C. A. Skeie, A. Mezentzev, P. Kochkin, K. Ullaland, S. Yang, G. Genov, B. E. Carlson, C. Köhn, J. Navarro-Gonzalez, P. Connell, V. Reglero, and T. Neubert (2021), Spectral analysis of individual terrestrial gamma-ray flashes detected by asim, *Journal of Geophysical Research: Atmospheres*, 126(23), doi:https://doi.org/10.1029/2021JD035347. 1, 4.2.3, 5
- Lindanger, A., C. A. Skeie, M. Marisaldi, I. Bjørge-Engeland, N. Østgaard, A. Mezentsev, D. Sarria, N. Lehtinen, V. Reglero, O. Chanrion, and T. Neubert (2022), Production of terrestrial gamma-ray flashes during the early stages of lightning flashes, *Journal of Geophysical Research: Atmospheres*, 127(8), doi:https://doi.org/10.1029/2021JD036305. 4.2.2, 5
- Loeb, L., and J. Meek (1941), *The mechanism of the electric spark*, Stanford University Press, Stanford. 2.2.2
- Lu, G., R. J. Blakeslee, J. Li, D. M. Smith, X.-M. Shao, E. W. McCaul, D. E. Buechler, H. J. Christian, J. M. Hall, and S. A. Cummer (2010), Lightning mapping observation of a terrestrial gamma-ray flash, *Geophysical Research Letters*, 37(11), doi:https://doi.org/10.1029/2010GL043494. 1, 4.2, 4.2.2
- Luque, A., F. J. Gordillo-Vázquez, D. Li, A. Malagón-Romero, F. J. Pérez-Invernón, A. Schmalzried, S. Soler, O. Chanrion, M. Heumesser, T. Neubert, V. Reglero, and N. Østgaard (2020), Modeling lightning observations from space-based platforms (cloudscat.jl 1.0), *Geoscientific Model Development*, 13(11), 5549–5566, doi:10.5194/gmd-13-5549-2020. 5, 6
- Mailyan, B., M. Stanbro, M. S. Briggs, S. Cummer, J. R. Dwyer, O. J. Roberts, and R. Holzworth (2021), Radio frequency emissions associated with multi-pulsed terrestrial gamma-ray flashes, *Journal of Geophysical Research: Space Physics*, 126(2), e2020JA027,928, doi:https://doi.org/10.1029/2020JA027928. 4.2.3

- Mailyan, B. G., M. S. Briggs, E. S. Cramer, G. Fitzpatrick, O. J. Roberts, M. Stanbro, V. Connaughton, S. McBreen, P. N. Bhat, and J. R. Dwyer (2016), The spectroscopy of individual terrestrial gamma-ray flashes: Constraining the source properties, *Journal of Geophysical Research: Space Physics*, *121*(11), 11,346–11,363, doi:<https://doi.org/10.1002/2016JA022702>. 1, 4.2.3, 5
- Mailyan, B. G., W. Xu, S. Celestin, M. S. Briggs, J. R. Dwyer, E. S. Cramer, O. J. Roberts, and M. Stanbro (2019), Analysis of individual terrestrial gamma-ray flashes with lightning leader models and fermi gamma-ray burst monitor data, *Journal of Geophysical Research: Space Physics*, *124*(8), 7170–7183, doi:<https://doi.org/10.1029/2019JA026912>. 4.2.3
- Maiorana, C., M. Marisaldi, A. Lindanger, N. Østgaard, A. Ursi, D. Sarria, M. Galli, C. Labanti, M. Tavani, C. Pittori, and F. Verrecchia (2020), The 3rd agile terrestrial gamma-ray flashes catalog. part ii: Optimized selection criteria and characteristics of the new sample, *Journal of Geophysical Research: Atmospheres*, *125*(11), e2019JD031,986, doi:<https://doi.org/10.1029/2019JD031986>. 4.2.3
- Maiorana, C., M. Marisaldi, M. Füllekrug, S. Soula, J. Lapierre, A. Mezentsev, C. A. Skeie, M. Heumesser, O. Chanrion, N. Østgaard, T. Neubert, and V. Reglero (2021), Observation of terrestrial gamma-ray flashes at mid latitude, *Journal of Geophysical Research: Atmospheres*, *126*(18), e2020JD034,432, doi:<https://doi.org/10.1029/2020JD034432>. 4.2.4
- Marisaldi, M., F. Fuschino, C. Labanti, M. Galli, F. Longo, E. Del Monte, G. Barbiellini, M. Tavani, A. Giuliani, E. Moretti, S. Vercellone, E. Costa, S. Cutini, I. Donnarumma, Y. Evangelista, M. Feroci, I. Lapshov, F. Lazzarotto, P. Lipari, S. Mereghetti, L. Pacciani, M. Rapisarda, P. Soffitta, M. Trifoglio, A. Argan, F. Boffelli, A. Bulgarelli, P. Caraveo, P. W. Cattaneo, A. Chen, V. Cocco, F. D'Ammando, G. De Paris, G. Di Cocco, G. Di Persio, A. Ferrari, M. Fiorini, T. Froyland, F. Gianotti, A. Morselli, A. Pellizzoni, F. Perotti, P. Picozza, G. Piano, M. Pilia, M. Prest, G. Pucella, A. Rappoldi, A. Rubini, S. Sabatini, E. Striani, A. Trois, E. Vallazza, V. Vittorini, A. Zambra, D. Zanello, L. A. Antonelli, S. Colafrancesco, D. Gasparrini, P. Giommi, C. Pittori, B. Preger, P. Santolamazza, F. Verrecchia, and L. Salotti (2010), Detection of terrestrial gamma ray flashes up to 40 mev by the agile satellite, *Journal of Geophysical Research: Space Physics*, *115*(A3), doi:<https://doi.org/10.1029/2009JA014502>. 4.2, 4.2.3
- Marisaldi, M., F. Fuschino, M. Tavani, S. Dietrich, C. Price, M. Galli, C. Pittori, F. Verrecchia, S. Mereghetti, P. W. Cattaneo, S. Colafrancesco, A. Argan, C. Labanti, F. Longo, E. Del Monte, G. Barbiellini, A. Giuliani, A. Bulgarelli, R. Campana, A. Chen, F. Gianotti, P. Giommi, F. Lazzarotto, A. Morselli, M. Rapisarda, A. Rappoldi, M. Trifoglio, A. Trois, and S. Vercellone (2014), Properties of terrestrial gamma ray flashes detected by agile mcal below 30 mev, *Journal of Geophysical Research: Space Physics*, *119*(2), 1337–1355, doi:<https://doi.org/10.1002/2013JA019301>. 4.2, 4.2.3
- Marisaldi, M., A. Argan, A. Ursi, T. Gjesteland, F. Fuschino, C. Labanti, M. Galli, M. Tavani, C. Pittori, F. Verrecchia, F. D'Amico, N. Østgaard, S. Mereghetti, R. Cam-

- pana, P. Cattaneo, A. Bulgarelli, S. Colafrancesco, S. Dietrich, F. Longo, F. Gianotti, P. Giommi, A. Rappoldi, M. Trifoglio, and A. Trois (2015), Enhanced detection of terrestrial gamma-ray flashes by agile, *Geophysical Research Letters*, 42(21), 9481–9487, doi:<https://doi.org/10.1002/2015GL066100>. 4.2.2
- Mazur, V. (1989a), A physical model of lightning initiation on aircraft in thunderstorms, *Journal of Geophysical Research: Atmospheres*, 94(D3), 3326–3340, doi:<https://doi.org/10.1029/JD094iD03p03326>. 3.1, 3.2.1, 3.2.2
- Mazur, V. (1989b), Triggered lightning strikes to aircraft and natural intracloud discharges, *Journal of Geophysical Research: Atmospheres*, 94(D3), 3311–3325, doi:[10.1029/JD094iD03p03311](https://doi.org/10.1029/JD094iD03p03311). 3.2.2
- Mazur, V. (2002), Physical processes during development of lightning flashes, *Applied Physics*, 3, 1393–1409, doi:[10.1016/S1631-0705\(02\)01412-3](https://doi.org/10.1016/S1631-0705(02)01412-3). 3.2.2
- Mazur, V., and J. Moreaut (1992), Aircraft-triggered lightning: Processes following strike initiation that affect aircraft, *Journal of Aircraft*, 29(4), 575–580, doi:[10.2514/3.46204](https://doi.org/10.2514/3.46204). 3.2.2
- Mazur, V., and L. Ruhnke (1993), Common physical processes in natural and artificially triggered lightning, *Journal of Geophysical Research*, 98, 12,913–12,930, doi:[10.1111/j.1555-2934.2009.01042.x](https://doi.org/10.1111/j.1555-2934.2009.01042.x). 3.2.2
- Mazur, V., L. H. Ruhnke, T. A. Warner, and R. E. Orville (2013), Recoil leader formation and development, *Journal of Electrostatics*, 71, 763–768, doi:[10.1016/j.elstat.2013.05.001](https://doi.org/10.1016/j.elstat.2013.05.001). 3.2.2
- McCarthy, M., and G. Parks (1985), Further observations of x-rays inside thunderstorms, *Geophysical Research Letters*, 12(6), 393–396, doi:[10.1029/GL012i006p00393](https://doi.org/10.1029/GL012i006p00393). 1, 4.1
- Meek, J. M. (1940), A theory of spark discharge, *Phys. Rev.*, 57, 722–728, doi:[10.1103/PhysRev.57.722](https://doi.org/10.1103/PhysRev.57.722). 2.2.2
- Mehranzamid, K., H. N. Afrouzi, Z. Abdul-Malek, Z. Nawawi, M. A. B. Sidik, and M. I. Jambak (2019), Hardware and software implementation of magnetic direction finding sensors, in *2019 International Conference on Electrical Engineering and Computer Science (ICECOS)*, pp. 23–28, doi:[10.1109/ICECOS47637.2019.8984532](https://doi.org/10.1109/ICECOS47637.2019.8984532). 2.2.5
- Miller, E. (1968), Synopsis of a thunderstorm research program (roughrider) for 1966–1967, *Technical Report ASD-TR-68-29*. 3, 4.1
- Montanyà, J., F. Fabró, O. van der Velde, D. Romero, G. Solà, J. R. Hermoso, S. Soula, E. R. Williams, and N. Pineda (2014), Registration of x-rays at 2500 m altitude in association with lightning flashes and thunderstorms, *Journal of Geophysical Research: Atmospheres*, 119(3), 1492–1503, doi:[10.1002/2013JD021011](https://doi.org/10.1002/2013JD021011). 4.1
- Moore, C., K. Eack, G. Aulich, and W. Rison (2001), Energetic radiation associated with lightning stepped-leaders, *Geophysical Research Letters*, 28(11), 2141–2144, doi:[10.1029/2001GL013140](https://doi.org/10.1029/2001GL013140). 1, 4.1, 4.1.1

- Moreaut, J., J. Alliot, and V. Mazur (1992), Aircraft lightning initiation and interception from in situ electric measurements and fast video observations, *Journal of Geophysical Research*, 97(D14), 15,903–15,912, doi:10.1029/92JD01077. 3.2.2
- Morgan, D., C. Hardwick, S. Haigh, and A. Meakins (2012), The interaction of lightning with aircraft and the challenges of lightning testing, *Journal Aerospace Lab*, (5), 1–10. 3, 3.1, 3.1
- Moss, G. D., V. P. Pasko, N. Liu, and G. Veronis (2006), Monte carlo model for analysis of thermal runaway electrons in streamer tips in transient luminous events and streamer zones of lightning leaders, *Journal of Geophysical Research: Space Physics*, 111(A2), doi:https://doi.org/10.1029/2005JA011350. 1, 4.2.1, 4.4, 4.2.1
- Nemiroff, R. J., J. T. Bonnell, and J. P. Norris (1996), Temporal and spectral characteristics of terrestrial gamma flashes, *AIP Conference Proceedings*, 384(1), 990–994, doi:10.1063/1.51633. 1, 4.2.3
- Neubert, T., N. Østgaard, V. Reglero, E. Blanc, O. Chanrion, C. Oxborrow, A. Orr, M. Tacconi, O. Hartnack, and D. Bhandari (2019), The asim mission on the international space station, *Space Science Reviews*, 215(26), doi:https://doi.org/10.1007/s11214-019-0592-z. 1, 2.5, 4.2.4
- Neubert, T., N. Østgaard, V. Reglero, O. Chanrion, M. Heumesser, K. Dimitriadou, F. Christiansen, C. Budtz-Jørgensen, I. Kuvvetli, I. L. Rasmussen, A. Mezentsev, M. Marisaldi, K. Ullaland, G. Genov, S. Yang, P. Kochkin, J. Navarro-Gonzalez, P. H. Connell, and C. J. Eyles (2020), A terrestrial gamma-ray flash and ionospheric ultraviolet emissions powered by lightning, *Science*, 367(6474), 183–186, doi:10.1126/science.aax3872. 4.2.2
- Ogawa, T., and M. Brook (1964), The mechanism of the intracloud lightning discharge, *Journal of Geophysical Research*, 69(24), 5141–5150, doi:10.1029/JZ069i024p05141. 3.2.2
- Parks, G., B. H. Mauk, R. Spiger, and J. Chin (1981), X-ray enhancements detected during thunderstorm and lightning activities, *Geophysical Research Letters*, 8(11), 1176–1179, doi:10.1029/GL008i011p01176. 1, 4.1
- Pu, Y., S. A. Cummer, F. Lyu, M. Briggs, B. Mailyan, M. Stanbro, and O. Roberts (2019), Low frequency radio pulses produced by terrestrial gamma-ray flashes, *Geophysical Research Letters*, 46(12), 6990–6997, doi:https://doi.org/10.1029/2019GL082743. 1, 4.2, 4.2.2, 4.2.3
- Raizer, Y. P. (1992), *Gas Discharge Physics*, Springer Berlin, Heidelberg. 2.2.1, 2.2.2, 2.2.2
- Rakov, V., and M. Uman (2003), *Lightning: Physics and Effects*, Cambridge University Press. 2.1, 2.2, 2.2, 2.2.3, 2.2.3, 2.2.5, 3, 3.1, 4.2.1
- Reazer, J. S., A. V. Serrano, L. C. Walko, and C. H. D. Burket (1987), Analysis of correlated electromagnetic fields and current pulses during airborne lightning attachments, *Electromagnetics*, 7(3-4), 509–539, doi:10.1080/02726348708908196. 3

- Roberts, O. J., G. Fitzpatrick, G. Priftis, K. Bedka, T. Chronis, S. McBreen, M. S. Briggs, E. Cramer, B. Mailyan, and M. Stanbro (2017), Terrestrial gamma ray flashes due to particle acceleration in tropical storm systems, *Journal of Geophysical Research: Atmospheres*, 122(6), 3374–3395, doi:<https://doi.org/10.1002/2016JD025799>. 4.2.3
- Rodger, C. J., J. B. Brundell, and R. L. Dowden (2005), Location accuracy of vlf worldwide lightning location (wwll) network: Post-algorithm upgrade, *Annales Geophysicae*, 23(2), 277–290, doi:[10.5194/angeo-23-277-2005](https://doi.org/10.5194/angeo-23-277-2005). 2.2.5
- Said, R., and M. Murphy (2016), Gld360 upgrade: Performance analysis and applications, *Conference paper: 24th International Lightning Detection Conference 6th International Lightning Meteorology Conference*. 2.2.5
- Said, R. K., U. S. Inan, and K. L. Cummins (2010), Long-range lightning geolocation using a vlf radio atmospheric waveform bank, *Journal of Geophysical Research: Atmospheres*, 115(D23), doi:<https://doi.org/10.1029/2010JD013863>. 2.2.5
- Said, R. K., M. B. Cohen, and U. S. Inan (2013), Highly intense lightning over the oceans: Estimated peak currents from global gld360 observations, *Journal of Geophysical Research: Atmospheres*, 118(13), 6905–6915, doi:<https://doi.org/10.1002/jgrd.50508>. 2.2.5
- Saleh, Z., J. Dwyer, J. Howard, M. Uman, M. Bakhtiari, D. Concha, M. Stapleton, D. Hill, C. Biagi, and H. Rassoul (2009), Properties of the X-ray emission from rocket-triggered lightning as measured by the Thunderstorm Energetic Radiation Array (TERA), *Journal of Geophysical Research*, 114(17), doi:[10.1029/2008JD011618](https://doi.org/10.1029/2008JD011618). 1, 4.1
- Schaal, M., J. Dwyer, Z. Saleh, H. Rassoul, J. Hill, D. Jordan, and M. Uman (2012), Spatial and energy distributions of X-ray emissions from leaders in natural and rocket triggered lightning, *Journal of Geophysical Research*, 117(15), D15,201, doi:[10.1029/2012JD017897](https://doi.org/10.1029/2012JD017897). 1, 4.1
- Shao, X.-M., T. Hamlin, and D. M. Smith (2010), A closer examination of terrestrial gamma-ray flash-related lightning processes, *Journal of Geophysical Research: Space Physics*, 115(A6), doi:<https://doi.org/10.1029/2009JA014835>. 1, 4.2, 4.2.2
- Skeie, C. A. (2018), Aircraft interaction with electric field of thundercloud and observations of hard radiation, Masters-thesis, University of Bergen, doi:<https://hdl.handle.net/1956/18377>. 3, 4.1.1
- Skeie, C. A., N. Østgaard, N. G. Lehtinen, D. Sarria, P. Kochkin, A. I. de Boer, M. Bardet, C. Allasia, and F. Flourens (2020), Constraints on recoil leader properties estimated from x-ray emissions in aircraft-triggered discharges, *Journal of Geophysical Research: Atmospheres*, 125(14), e2019JD032,151, doi:<https://doi.org/10.1029/2019JD032151>. 3.4, 4.1.2, 4.1.3, 4.2, 5
- Skeie, C. A., N. Østgaard, A. Mezentsev, I. Bjørge-Engeland, M. Marisaldi, N. Lehtinen, V. Reglero, and T. Neubert (2022 In review), The temporal relationship between

- terrestrial gamma-ray flashes and associated optical pulses from lightning, *Journal of Geophysical Research: Atmospheres*, 4.2.2, 4.2.4, 4.2.4, 4.7, 4.8, 5
- Skeltved, A. B., N. Østgaard, A. Mezentsev, N. Lehtinen, and B. Carlson (2017), Constraints to do realistic modeling of the electric field ahead of the tip of a lightning leader, *Journal of Geophysical Research: Atmospheres*, 122(15), 8120–8134, doi: <https://doi.org/10.1002/2016JD026206>. 4.2.3, 5
- Smith, D. M., L. I. Lopez, R. P. Lin, and C. P. Barrington-Leigh (2005), Terrestrial gamma-ray flashes observed up to 20 mev, *Science*, 307(5712), 1085–1088, doi: [10.1126/science.1107466](https://doi.org/10.1126/science.1107466). 4.2, 4.2.3
- Smith, D. M., J. R. Dwyer, B. J. Hazelton, B. W. Grefenstette, G. F. M. Martinez-McKinney, Z. Y. Zhang, A. W. Lowell, N. A. Kelley, M. E. Splitt, S. M. Lazarus, W. Ulrich, M. Schaal, Z. H. Saleh, E. Cramer, H. K. Rassoul, S. A. Cummer, G. Lu, and R. J. Blakeslee (2011), The rarity of terrestrial gamma-ray flashes, *Geophysical Research Letters*, 38(8), doi:<https://doi.org/10.1029/2011GL046875>. 4.2
- Smith, D. M., P. Buzbee, N. A. Kelley, A. Infanger, R. H. Holzworth, and J. R. Dwyer (2016), The rarity of terrestrial gamma-ray flashes: 2. rhesi stacking analysis, *Journal of Geophysical Research: Atmospheres*, 121(19), 11,382–11,404, doi: <https://doi.org/10.1002/2016JD025395>. 5
- Smith, D. M., N. A. Kelley, P. Buzbee, A. Infanger, M. Splitt, R. H. Holzworth, and J. R. Dwyer (2020), Special classes of terrestrial gamma ray flashes from rhesi, *Journal of Geophysical Research: Atmospheres*, 125(20), doi:<https://doi.org/10.1029/2020JD033043>. 4.2, 4.2.3
- Stanley, M. A., X.-M. Shao, D. M. Smith, L. I. Lopez, M. B. Pongratz, J. D. Harlin, M. Stock, and A. Regan (2006), A link between terrestrial gamma-ray flashes and intracloud lightning discharges, *Geophysical Research Letters*, 33(6), doi:<https://doi.org/10.1029/2005GL025537>. 1, 4.2.2, 4.2.3
- Takahashi, T. (1978), Riming electrification as a charge generation mechanism in thunderstorms, *Journal of Atmospheric Sciences*, 35(8), 1536 – 1548, doi:[10.1175/1520-0469\(1978\)035<1536:REAACG>2.0.CO;2](https://doi.org/10.1175/1520-0469(1978)035<1536:REAACG>2.0.CO;2). 2.1
- Tierney, D., M. S. Briggs, G. Fitzpatrick, V. L. Chaplin, S. Foley, S. McBreen, V. Connaughton, S. Xiong, D. Byrne, M. Carr, P. N. Bhat, G. J. Fishman, J. Greiner, R. M. Kippen, C. A. Meegan, W. S. Paciesas, R. D. Preece, A. von Kienlin, and C. Wilson-Hodge (2013), Fluence distribution of terrestrial gamma ray flashes observed by the fermi gamma-ray burst monitor, *Journal of Geophysical Research: Space Physics*, 118(10), 6644–6650, doi:<https://doi.org/10.1002/jgra.50580>. 4.2.3
- Torii, T., M. Takeishi, and T. Hosono (2002), Observation of gamma-ray dose increase associated with winter thunderstorm and lightning activity, *Journal of Geophysical Research: Atmospheres*, 107(D17), ACL 2–1–ACL 2–13, doi:<https://doi.org/10.1029/2001JD000938>. 1

- Torii, T., T. Nishijima, Z.-I. Kawasaki, and T. Sugita (2004), Downward emission of runaway electrons and bremsstrahlung photons in thunderstorm electric fields, *Geophysical Research Letters*, 31(5), doi:<https://doi.org/10.1029/2003GL019067>. 1
- Torii, T., T. Sugita, S. Tanabe, Y. Kimura, M. Kamogawa, K. Yajima, and H. Yasuda (2009), Gradual increase of energetic radiation associated with thunderstorm activity at the top of mt. fuji, *Geophysical Research Letters*, 36(13), doi:<https://doi.org/10.1029/2008GL037105>. 1
- Tran, M., V. Rakov, S. Mallick, J. Dwyer, A. Nag, and S. Heckman (2015), A terrestrial gamma-ray flash recorded at the lightning observatory in gainesville, florida, *Journal of Atmospheric and Solar-Terrestrial Physics*, 136, 86–93, doi:<https://doi.org/10.1016/j.jastp.2015.10.010>. 4.2
- Tsuchiya, H., T. Enoto, S. Yamada, T. Yuasa, M. Kawaharada, T. Kitaguchi, M. Kokubun, H. Kato, M. Okano, S. Nakamura, and K. Makishima (2007), Detection of high-energy gamma rays from winter thunderclouds, *Phys. Rev. Lett.*, 99, doi:10.1103/PhysRevLett.99.165002. 1
- Uman, M., and V. Rakov (2003), The interaction of lightning with airborne vehicles, *Progress in Aerospace Sciences*, 39(1), 61–81, doi:10.1016/S0376-0421(02)00051-9. 3, 4.1
- van Deursen, A. P. J., A. de Boer, M. Bardet, and J. Boissin (2013), Window sensor for the a350 and a380 aircraft, in *2013 International Conference on Electromagnetics in Advanced Applications (ICEAA)*, pp. 1000–1003, doi:10.1109/ICEAA.2013.6632391. 4.1.3
- Wada, Y., T. Enoto, Y. Nakamura, Y. Furuta, T. Yuasa, K. Nakazawa, T. Morimoto, M. Sato, T. Matsumoto, D. Yonetoku, T. Sawano, H. Sakai, M. Kamogawa, T. Ushio, K. Makishima, and H. Tsuchiya (2019), Gamma-ray glow preceding downward terrestrial gamma-ray flash, *Communications Physics*, 2(67), doi:<https://doi.org/10.1038/s42005-019-0168-y>. 4.2
- Williams, E. R. (1989), The tripole structure of thunderstorms, *Journal of Geophysical Research: Atmospheres*, 94(D11), 13,151–13,167, doi:<https://doi.org/10.1029/JD094iD11p13151>. 2.1
- Wilson, C. (1924), The electric field of a thundercloud and some of its effects, *Proc. Phys. Soc. London.*, 32D(37). 1, 4, 4.2.1
- Xu, W., S. Celestin, and V. P. Pasko (2012), Source altitudes of terrestrial gamma-ray flashes produced by lightning leaders, *Geophysical Research Letters*, 39(8), doi:<https://doi.org/10.1029/2012GL051351>. 1, 4.2.3
- Zwemmer, R., M. Bardet, A. de Boer, J. Hardwick, D. Hawking, K. Morgan, M. Latorre, N. Marchand, J. Ramos, I. Revel, and W. Tauber (2013a), In-flight lightning damage assessment system (ILDAS), in *Proceedings of the 2013 International Conference on Lightning and Static Electricity (ICOLSE), 18-20 September 2013, Seattle, Washington*. 4.1.3

- Zwemmer, R., M. Bardet, A. de Boer, J. Hardwick, D. Hawking, K. Morgan, M. Latorre, N. Marchand, J. Ramos, I. Revel, and W. Tauber (2013b), In-flight lightning damage assessment system (ILDAS); results of the concept prototype tests., in *Proceedings of the 2013 International Conference on Lightning and Static Electricity (ICOLSE), 18-20 September 2013, Seattle, Washington*. 4.1.3
- Østgaard, N., T. Gjesteland, J. Stadsnes, P. H. Connell, and B. Carlson (2008), Production altitude and time delays of the terrestrial gamma flashes: Revisiting the burst and transient source experiment spectra, *Journal of Geophysical Research: Space Physics*, 113(A2), doi:<https://doi.org/10.1029/2007JA012618>. 4.2.3
- Østgaard, N., T. Gjesteland, R. S. Hansen, A. B. Collier, and B. Carlson (2012), The true fluence distribution of terrestrial gamma flashes at satellite altitude, *Journal of Geophysical Research: Space Physics*, 117(A3), doi:<https://doi.org/10.1029/2011JA017365>. 4.2.3
- Østgaard, N., T. Gjesteland, B. E. Carlson, A. B. Collier, S. A. Cummer, G. Lu, and H. J. Christian (2013), Simultaneous observations of optical lightning and terrestrial gamma ray flash from space, *Geophysical Research Letters*, 40(10), 2423–2426, doi:<https://doi.org/10.1002/grl.50466>. 1, 4.2.2
- Østgaard, N., H. J. Christian, J. E. Grove, D. Sarria, A. Mezentsev, P. Kochkin, N. Lehtinen, M. Quick, S. Al-Nussirat, E. Wulf, G. Genov, K. Ullaland, M. Marisaldi, S. Yang, and R. J. Blakeslee (2019a), Gamma ray glow observations at 20-km altitude, *Journal of Geophysical Research: Atmospheres*, 124(13), 7236–7254, doi:<https://doi.org/10.1029/2019JD030312>. 1
- Østgaard, N., T. Neubert, V. Reglero, K. Ullaland, S. Yang, G. Genov, M. Marisaldi, A. Mezentsev, P. Kochkin, N. Lehtinen, D. Sarria, B. H. Qureshi, A. Solberg, C. Maiorana, K. Albrechtsen, C. Budtz-Jørgensen, I. Kuvvetli, F. Christiansen, O. Chanrion, M. Heumesser, J. Navarro-Gonzalez, P. Connell, C. Eyles, H. Christian, and S. Al-nussirat (2019b), First 10 months of tgf observations by asim, *Journal of Geophysical Research: Atmospheres*, 124(24), 14,024–14,036, doi:<https://doi.org/10.1029/2019JD031214>. 4.2, 4.2.2, 4.2.3
- Østgaard, N., J. E. Balling, T. Bjørnsen, P. Brauer, C. Budtz-Jørgensen, W. Bu-jwan, B. Carlson, F. Christiansen, P. Connell, C. Eyles, D. Fehlker, G. Genov, P. Grudziski, P. Kochkin, A. Kohfeldt, I. Kuvvetli, P. L. Thomsen, S. M. Pedersen, J. Navarro-Gonzalez, T. Neubert, K. Njøten, P. Orleanski, B. H. Qureshi, L. R. Cenkeramaddi, V. Reglero, M. Reina, J. M. Rodrigo, M. Rostad, M. D. Sabau, S. S. Kristensen, Y. Skogseide, A. Solberg, J. Stadsnes, K. Ullaland, and S. Yang (2019c), The modular x- and gamma-ray sensor (mxgs) of the asim payload on the international space station, *Space Science Reviews*, 215(23), doi:<https://doi.org/10.1007/s11214-018-0573-7>. 4.2.4
- Østgaard, N., S. A. Cummer, A. Mezentsev, A. Luque, J. Dwyer, T. Neubert, V. Reglero, M. Marisaldi, P. Kochkin, D. Sarria, N. Lehtinen, K. Ullaland, S. Yang, G. Genov, O. Chanrion, F. Christiansen, and Y. Pu (2021), Simultaneous observations of eip, tgf, elve, and optical lightning, *Journal of Geophysical Research: Atmospheres*, 126(11), doi:<https://doi.org/10.1029/2020JD033921>. 4.2

Chapter 7

Scientific results

Paper I

Constraints on Recoil Leader Properties Estimated from X-ray Emissions in Aircraft-triggered Discharges

C. A. Skeie, N. Østgaard, N. G. Lehtinen, D. Sarria, P. Kochkin, A. I. de Boer, M. Bardet, C. Allasia, F. Flourens

Journal of Geophysical Research: Atmospheres, **125** (2020)



RESEARCH ARTICLE

10.1029/2019JD032151

Key Points:

- Observations of 54 X-ray bursts associated with recoil events during aircraft-triggered lightning are presented
- Using three models, we find constraints to the gap and leader length of the recoil events
- We find that the gap length is restricted from 1 to 93 m and the leader length is from 1 to 240 m

Correspondence to:

C. A. Skeie,
Chris.Skeie@uib.no

Citation:

Skeie, C. A., Østgaard, N., Lehtinen, N. G., Sarria, D., Kochkin, P., de Boer, A. I., et al. (2020). Constraints on recoil leader properties estimated from X-ray emissions in aircraft-triggered discharges. *Journal of Geophysical Research: Atmospheres*, 125, e2019JD032151. <https://doi.org/10.1029/2019JD032151>

Received 3 DEC 2019

Accepted 9 JUN 2020

Accepted article online 10 JUN 2020

Constraints on Recoil Leader Properties Estimated from X-ray Emissions in Aircraft-Triggered Discharges

C. A. Skeie¹ , N. Østgaard¹ , N. G. Lehtinen¹ , D. Sarria¹ , P. Kochkin¹ , A. I. de Boer² , M. Bardet² , C. Allasia³ , and F. Flourens³ 

¹Birkeland Centre for Space Science, Institute of Physics and Technology, University of Bergen, Bergen, Norway, ²Royal Netherlands Aerospace Centre, Amsterdam, Netherlands, ³Airbus, Toulouse, France

Abstract During Airbus aircraft campaigns flying into thunderstorms in 2014–2016, X-rays were observed during two stages of aircraft-triggered lightning: nanosecond pulses of X-rays associated with negative leader steps and bursts of X-rays during recoil events. This work will focus on the observations of X-ray bursts associated with recoils. Recoils are observed as microsecond-fast changes in the local electric field, associated with large currents passing through the aircraft, and are found to sometimes be associated with bursts of X-rays. From over 200 aircraft-triggered lightning strikes, 54 recoil events were found to be associated with microsecond bursts of X-rays. The majority of the bursts consist of 1–3 X-ray pulses, with some bursts containing as many as 29 X-ray pulses. We compare the observed superposed X-ray spectrum with modeled spectra using a GEANT4 model of the detector and aircraft, to determine the source potential needed to accelerate the electrons that produce the observed X-rays. A model of the recoil leader was made to determine the gap distance and gap potential between the recoil leader and the aircraft. From the modeling, we determine a solution space for the gap and leader lengths where the gap length is constrained by the observed minimum and maximum times between the onset of the X-ray pulses and the onset of the current pulses detected at the aircraft (1 to 93 m). We also find two constraints from the fitting of the modeled spectra to the superposed spectrum, limiting the leader length to between 1 and ~240 m.

1. Introduction

Most lightning strikes to aircraft are not intercepted but triggered by the aircraft itself. The triggering of a lightning strike happens as the aircraft enters a sufficiently large ambient electric field, such as those found in thunder clouds. In the presence of the ambient electric field, the aircraft will be polarized, and the local electric field on the aircraft and its vicinity will become amplified. The sharper parts of the aircraft (nose, tail, and wing tips) will experience the most intense amplifications, as they will enhance the electric field the most. This intensification can lead to the triggering of a lightning discharge from the aircraft. The triggered lightning will consist of a bidirectional leader originating from the aircraft. Commonly, the bidirectional leader will start with a positive leader initiating at one extremity of the aircraft, which propagates in the direction of the ambient electric field. This will further polarize the aircraft, and a negative leader will shortly after be initiated at a different extremity, which will propagate in the opposite direction of the ambient electric field. The bidirectional leaders may then connect to oppositely charged regions in the thunderclouds and trigger a lightning flash, with the aircraft as part of the lightning channel (Mazur, 1989a).

There have been four major airborne lightning-characterization studies that have laid the groundwork for our understanding of the aircraft-lightning relationship. These are as follows: Rough Rider project in the 1960s, NASA's Storm Hazards Program, the Lightning Characterisation Program, and the Transall Program in the 1980s. These four programs collected data on the various stages of thunderstorms, lightning attachment points and current measurements on the aircraft during lightning strikes, ambient and local electric field measurements, X-ray measurements, and optical observations (Fisher et al., 1988; McCarthy & Parks, 1985; Miller, 1968; Parks et al., 1981; Uman & Rakov, 2003). There has also been three aircraft campaigns (ALOFT, ADELE, and ILDAS) dedicated to the study of high-energy emissions from lightning and thunderclouds, such as terrestrial gamma-ray flashes (TGFs), gamma-ray glows, and X-rays generated

©2020. The Authors.

This is an open access article under the terms of the Creative Commons Attribution-NonCommercial-NoDerivs License, which permits use and distribution in any medium, provided the original work is properly cited, the use is non-commercial and no modifications or adaptations are made.

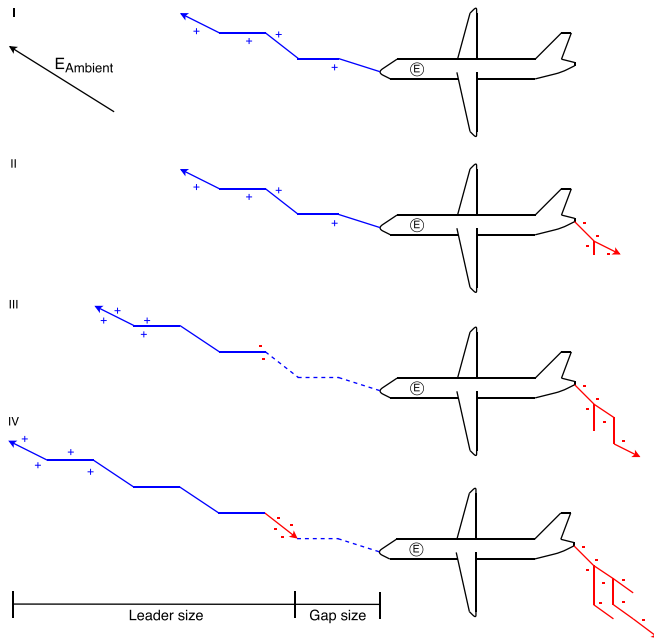


Figure 1. Figure illustrating the initiation of an aircraft-triggered lightning strike and the formation of a recoil leader. (I) The aircraft initiates the positive leader (blue line) after becoming charged and polarized. (II) A few milliseconds later, the negative leader (red line) is launched from an opposite extremity of the aircraft. (III) Tens of milliseconds later, after the current cutoff, the positive leader will continue to propagate, while the lower end (dotted blue line) will cool down and lose conductivity. The leader will obtain induced charges, which will be distributed as a dipole. (IV) The induced charges may lead to negative electric breakdown at the lower end of the positive channel, initiating an ionization wave, which will form a negative recoil leader (red arrow on the left side of the aircraft), which will propagate back toward the aircraft inside the cooled channel (Mazur & Ruhnke, 1993).

during aircraft-triggered lightning strikes (Dwyer et al., 2012; Kelley et al., 2015; Kochkin et al., 2015, 2017, 2018; Østgaard et al., 2019).

In the early 2000s, it was discovered that both natural and triggered lightning can generate microsecond-fast bursts of X-rays (Dwyer, 2004, 2003; Dwyer et al., 2004, 2005, 2011; Howard et al., 2010; Kochkin et al., 2015; Montanyà et al., 2014; Moore et al., 2001; Saleh et al., 2009; Schaal et al., 2012). The observed energies of the bursts are typically in the range of a few hundreds of keV. The bursts of radiation have since been tied to the stepping of negative leaders and to the so-called recoil events during a lightning flash.

According to Mazur (2002) and Mazur et al. (2013), recoil events are a collective term for dart and recoil leaders observed during a lightning flash. During recoil events, large currents pass through an already existing leader channel. These events are some of the most luminous and noticeable parts of a lightning flash. Ogawa and Brook (1964) suggest that the events known as K-changes are negative recoil leaders occurring when a positive leader propagates into a negative charge in a cloud. From analysis of aircraft-triggered lightning flashes, it was hypothesized that recoil leaders are initiated when the positive part of a bidirectional leader extends into a region of negative charge, where an ionizing wave will initiate and propagate back toward the aircraft, along the channel of the preceding positive part of the bidirectional leader attached to the aircraft. The mechanism for the occurrence of a recoil leader is still unknown. Figure 1 shows an illustration of the steps from lightning initiation to recoil leader formation, which we observe in most aircraft-triggered lightning strikes. In Step I, the aircraft has entered a thundercloud, been polarized, and initiated a positive leader. The positive leader will travel in the direction of the ambient electric field and causes negative charge to

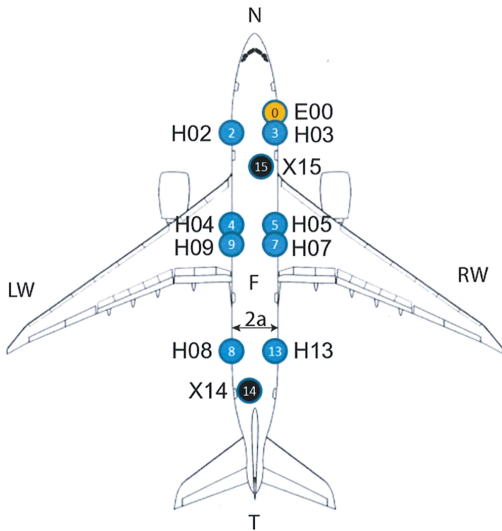


Figure 2. Distribution of the ILDA sensors on board the Airbus aircraft in 2014 to 2016. The sensor named E00 is the onboard local electric field sensor, HXX sensors are the H-field sensors, and the XXX sensors are the X-ray sensors. Image from Kochkin et al. (2015).

accumulate on the aircraft. Step II happens a few milliseconds after Step I, when the aircraft launches a negative leader from a different extremity. The negative leader will propagate in the opposite direction of the ambient electric field and remove negative charge from the aircraft. Step III happens tens of milliseconds later, after the current cutoff. Now the positive leader channel continues to extend away from the aircraft, while the connected end cools down and loses conductivity, all the while maintaining its net positive charge. The positive leader will obtain induced charges, which will be distributed as a dipole. Step IV shows how the charging may lead to negative electrical breakdown at the active part of the positive leader end close to the aircraft, initiating an ionizing wave, which forms the negative recoil leader. This negative recoil leader will propagate backwards through the cooled channel, until it reaches the origin of the positive leader (the aircraft) (Kochkin et al., 2015; Lalande et al., 1999; Laroche et al., 2012; Mazur, 1989a, 1989b; Mazur & Moreaut, 1992; Mazur & Ruhnke, 1993; Moreaut et al., 1992).

In this paper, we will report observations of X-rays associated with lightning recoil events during aircraft-triggered lightning and use these observations to define a constraint on recoil leader properties.

2. Instruments and Data

During 2014–2016, three thunderstorm-penetrating aircraft campaigns were conducted by Airbus. The aircraft was equipped with the In-flight Lightning Damage Assessment System (ILDAS) (Royal Netherlands Aerospace Centre, 2015), which consisted of one local electric field sensor,

two X-ray detectors, and eight H-field detectors, distributed as shown in Figure 2. The system was created by the Royal Netherlands Aerospace Centre in collaboration with 12 partners to measure lightning flash parameters and to determine lightning leader entry and exit points on the aircraft. This system is extensively described in Boissin et al. (2012), Deursen (2011), de Boer et al. (2011), de Boer, Boissin, et al. (2013), de Boer, Bardet, et al. (2013, 2015), van Deursen et al. (2013), Herv et al. (2014), and Zwemmer et al. (2009).

Both the E- and H-field detectors are differential detectors with a frequency band from 10 Hz to 500 kHz for the E-field sensor and 100 Hz to 50 MHz for the H-field sensor. Both sensors have a sampling rate of 83.3 MHz, which corresponds to a sampling interval of 12 ns. The main purpose of the E-field sensor is to act as a trigger for data recording during lightning flashes. The E-field sensor is mounted on the edge of a window toward the front of the aircraft, where it enhances the local electric field over the homogeneous electric field of the fuselage. As the local electric field signal is time differentiated, the zero value for the electric field is of an unknown magnitude. The polarity of the E-field sensor signal is chosen such that a positive signal corresponds to electric field lines pointed toward the detector (Kochkin et al., 2015). The H-field sensors are used to find the current passing through the hull of the aircraft. Six of the detectors are set up to measure the current passing from nose to tail, and sensors H04 and H05 measure the current entering the main fuselage from the wings. The X-ray detectors consist of two cylindrical LaBr₃(Ce) scintillators of 38 × 38 mm² size, connected to photomultipliers. The photomultiplier has a rise time of 11 ns, during which we cannot distinguish single photons. The sampling rate of the X-ray detectors is 100 MHz, which corresponds to a sampling interval of 10 ns. The X-ray detectors can measure up to 10 MeV, but the sensitivity of the instrument decreases from ~550 keV, as seen in Figure 10 in Kochkin et al. (2018).

The measurements are continuously stored in a 1.2 s ring buffer memory. When a lightning flash occurs, the local electric field sensor will trigger, and data will be collected and saved for all the sensors for a period of 0.2 s before the trigger and up to 1 s after the trigger. Most data used in this paper were obtained from the 2014–2015 campaigns, consisting of 9 days where the aircraft flew into thunderclouds at an average altitude of 4 km over southern Europe and the Mediterranean Sea. Six X-ray-producing recoil events were also found in the 2016 campaign data, consisting of 6 days where the aircraft flew at 10 km altitudes over northern Australia.

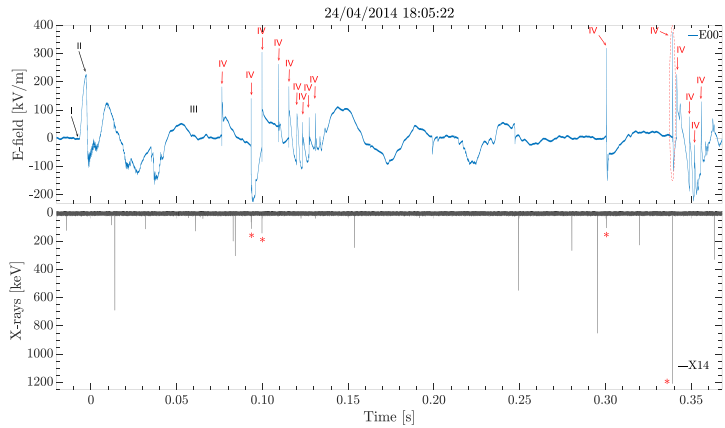


Figure 3. (Top panel) Local electric field measurements during the aircraft-triggered lightning on board the aircraft. The number I and II arrows show when the positive and negative lightning leaders are initiated, the number III arrow indicates the time of the current cutoff, and the red arrows show 15 recoil events. The dotted red ellipse shows a recoil event with associated X-ray burst. (Bottom panel) X-ray measurements during the aircraft-triggered lightning, with red asterisks showing nonbackground X-ray bursts.

3. Observations

During the ILDAS campaign, over 120 aircraft-triggered lightning strikes were observed over 15 days. Figure 3 shows the local electric field signature and accompanying X-ray measurements of one of these aircraft-triggered lightning strikes, with numbers indicating the different steps, as shown in Figure 1. The lightning strike is initiated as the positive leader is launched (I), which results in the local electric field increasing as the aircraft accumulates negative charge. A few milliseconds later, the negative leader is initiated (II), followed by a decline in the local electric field. Approximately 80 ms later, after the current cutoff (III), the first of 15 recoil processes are seen (red IVs) as a fast and large pulse in the local electric field, caused by the wave of negative charges passing through the aircraft. In the bottom panel, 12 background bursts with X-ray energies over 50 keV and multiple with lower energy can be seen. We define background as any count without an associated change in the local electric field. The red asterisks show the X-ray bursts associated with changes in the local electric field during the aircraft-triggered lightning strike. The majority of these background events stem from cosmic-ray background, but some are also from the radioactivity of the scintillation crystal. The background counts are heavily dependent on the flight altitude, with average values of 37 and 45 background counts per second for the 2014 and 2015 campaigns.

The recoil event marked with the dotted red ellipse is shown with a finer timescale in Figure 4. The top panel shows a ~ 400 kV/m change in local electric field caused by the sudden influx of negative charge from the recoil leader. The middle panel shows the currents passing through the aircraft as the recoil leader connects to the aircraft. The bottom panel shows the associated burst of five X-ray pulses. The dotted red lines show the delay of ~ 0.6 μ s between the onset of the X-ray observations and the onset of the current pulse. This type of delay was manually identified for all the recoil processes that had associated bursts of X-rays and were found to vary from 0.1 to 9.3 μ s with a mean of 1.75 μ s.

During the test flights, a total of 54 recoil events were found to be accompanied by detectable X-ray bursts. These recoil events produce microsecond-fast bursts of multiple nanosecond-fast X-ray pulses. The majority of these bursts consists of 1–3 pulses, but some were found to contain as many as 29 pulses. Due to instrumental limitations, the nanosecond-fast X-ray pulses can consist of multiple X-ray photons. The recoil events are all associated with large (average of 240 kV/m) changes in the local electric field, happening on a scale of microseconds, and with large (hundreds to thousands of amperes) long-lasting (microseconds long) current pulses flowing over the aircraft body. From the 54 observed recoil events, we identified 245 individual

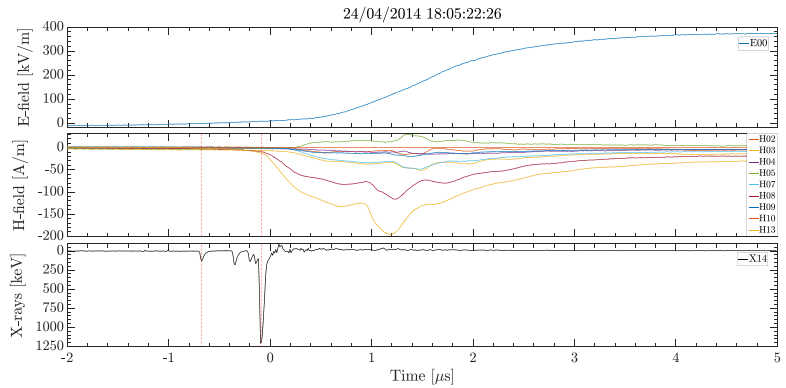


Figure 4. (Top panel) Local electric field signature of connecting recoil leader as observed on the aircraft. Electric field is plotted in such a way that a positive signal corresponds to electric field lines pointed toward the detector. (Middle panel) Measurements of the current passing through the aircraft fuselage during the recoil event. (Bottom panel) Associated X-ray burst, consisting of five pulses lasting approximately 1 μ s. The dotted red lines show the onset of the X-ray burst and the onset of the current pulses.

nanosecond pulses of X-rays. Out of the 245 ns pulses, 175 of them were observed before the current wave entered the aircraft. The X-rays produced after the current entered the aircraft are believed to be produced at different extremities of the aircraft by sparks, created by the change in surface potential on the aircraft by the connecting recoil leader. The full width at half the maximum of the X-rays pulses were then compared to each other and to a ^{137}Cs calibration source of 662 keV photons. Pulses with widths found to be over 25% broader than the calibration pulse were removed (19 such pulses were found), as they likely consist of multiple X-rays of lower energies. Figure 5 shows the energy spectra of the nanosecond X-ray pulses observed before the current wave enters the aircraft. As observed, there is a cutoff at 500 keV, which is a real cutoff, as the X-ray detectors can measure energies up to 10 MeV. The error bars are calculated as the square root of the counts of each bin of the spectrum. A bootstrapping method applied to the same modeled spectra (not shown) also gave the same error bars, except for the last two bins where they were a bit larger with the bootstrapping method.

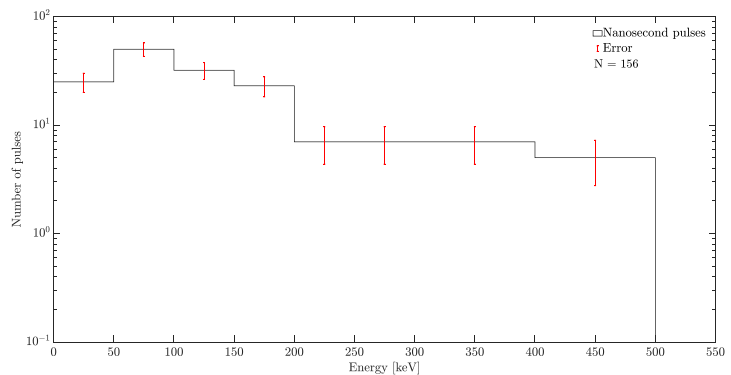


Figure 5. Superposed spectrum of 156 X-ray pulses associated with recoil processes in aircraft-triggered lightning, binned to 50 keV from 0 to 300, and 100 keV bins from 300 to 500, with error bars.

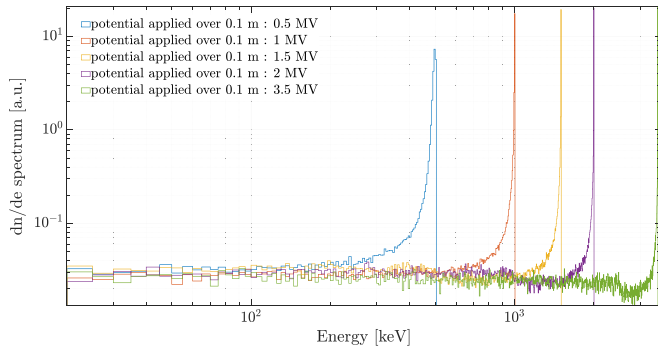


Figure 6. Modeled spectra of 20 keV seed electrons accelerated 0.5, 1, 1.5, 2, and 3.5 MV potentials over a 10 cm distance.

4. Method and Modeling

Our modeling efforts to find the potential difference in the gap between the recoil leader and aircraft, and recoil leader lengths are performed in three steps: (1) a GEANT4 model of the acceleration of 20 keV seed electrons over a small length analogue to the streamer zone, to ascertain if the electrons would all be accelerated to the full applied potential. (2) A second GEANT4 model of the detector and aircraft to model the X-ray spectra that should be detected with the various accelerated electrons from the first GEANT4 model as the input. We then use these modeled spectra to find the best fits to the superposed X-ray spectrum. (3) An electrostatic conductor model (ECM) of a converging lightning leader and aircraft in an ambient electric field, to obtain the potential in the gap between them. Using the potentials found from the second GEANT4 model as potential limits, together with the results of the ECM model and the time difference between the onset of the X-ray bursts and the onset of the currents, we find a solution space for the gap and recoil leader length limited by the lowest potential fit.

4.1. GEANT4 Model 1

A GEANT4 model (Agostinelli et al., 2003; Allison et al., 2006, 2016) was made to model the acceleration of electrons for different potentials over a short distance, analog to the streamer zone, to ascertain if the electrons would be accelerated to the full applied potential. In this model, we start with 20 keV seed electrons (we assume that the electrons have attained this energy from cold runaway, but we do not model this mechanism ourselves). We accelerated the electrons in an electric field that extend over 10 cm. Figure 6 shows the modeled electron spectra of the 20 keV seed electrons accelerated by potentials from 500 to 3,500 kV over a 10 cm distance, normalized by seed number. The figure shows that most electrons are accelerated to the full potential. Going forward, we use the accelerated electrons as a source of the observed X-rays in the second GEANT4 model of the Airbus test aircraft, with the ILDAS equipment on board (as previously used by Kochkin et al., 2018).

4.2. GEANT4 Model 2

In the second GEANT4 model, we model and fit the detected X-ray spectra, with the various accelerated electrons from the first GEANT4 model as input. In this model, we have included the response of our instrument with the aircraft fuselage. Considering that most electrons were accelerated to the full potential in the first GEANT4 model, we assume a monoenergetic electron source as input for this second model. The gap between the leader tip and the aircraft nose was set to 17.5 m, which corresponds to the average observed time between the onset of the X-ray bursts and the onset of the current pulse. A change of up to some tens of meters in the gap distance would not significantly affect the results of this model as it would be much less than the photons mean free path at 4 km altitude in air. In order for the X-rays to reach the detector, the initial electrons have to be within an approximately 20° half angle cone. Outside of this cone, the probability to observe an X-ray photon from the seed electrons is negligible. Therefore, only electrons within the

Table 1
Constant Parameters Used in the Modeling of the Electric Field and Potential Between the Approaching Negative Recoil Leader and the Aircraft

$r_{c.core}$ [m]	$r_{aircraft}$ [m]	$L_{aircraft}$ [m]	$E_{ambient}$ [kV/m]	$Q_{leaders}$ [C]	Altitude scaling factor
0.1	3	67	-24	0	~0.607

Note. r is the conductive core/aircraft radius, L is the aircraft length, E is the assumed ambient electric field, and Q is the assumed leader charge.

half-angle cone were modeled. For the smallest gap distance we use, it is possible for electrons to reach the aircraft itself and interact with the fuselage and detector; this is accounted for in the model.

4.3. ECM Model

A model of the electric field, potential, and charge transferred between the aircraft and the approaching negative leader was created, using the method of moments code as described in Harrington (1993) and Skeltved et al. (2017). The method of moments allows electrostatic modeling of an axially symmetric system of conductors. Multiple disconnected

conductors were modeled by having the corresponding number of constraints as a part of the system of equations A4 in Skeltved et al. (2017), which fix the total charge on each of the conductors. The rest of the system is obtained by minimization of the function A5 in Skeltved et al. (2017). The minimization with constraints requires use of Lagrange multipliers, which are the unknown potentials at each of the conductors. When the two disconnected conductors (aircraft and approaching negative leader) electrically connect, their potentials will equalize, while the sum of the charges will stay the same (mathematically, this means that the two constraints become a single constraint). This causes a charge transfer from the conductor that previously had the higher potential to the one with the lower potential. We model both the approaching negative leader and the aircraft as conducting cylinders with hemispherical caps at both ends, with a shared axis of symmetry. The leader channel during the recoil process is analogous to that of a return stroke in cloud-to-ground lightning and has a highly conductive core, with a conductive corona sheath of several meter diameter around it (Lehtinen, 2012). The length and position of the negative recoil leader in the model is variable, while the constant parameters are shown in Table 1.

In the model, we use a leader with conductive core radius of 10 cm, which is somewhat wider than the commonly accepted width of a leader channel; this radius was used because there is high conductivity also around the channel in the corona sheath. To check the results, a conductive core radius of 1 cm was also modeled, in which case the resulting gap potentials showed a mean difference less than 0.1%. The model does not take into consideration the corona sheath, same as in Skeltved et al. (2017). The aircraft is modeled as a conductive cylinder of 67 m length and 3 m radius, which is the actual length and radius of the Airbus A350-900 test aircraft. As the ambient electric field was not measured during the ILDAS campaign, we have chosen to set the value to -24 kV/m. This is the streamer propagation field, scaled to 4 km altitude (average flight altitude) using the scale height of Earth's atmosphere and reduced by a factor of 10, which corresponds to the amplification caused by the geometry of the aircraft (calculated from the ECM model). The initial charges of both the aircraft and the leader were set to zero, as we neglect them compared to the charge separation on both the leader and the aircraft, due to the ambient electric field. These assumptions may slightly affect the gap potential. Figure 7 shows the modeled electric field in the gap between the incoming negative recoil leader and the aircraft. Using the modeled electric field in the gap, we calculate the potential difference between the two leaders for gap distances between 1 and 93 m (from the minimum and maximum time between the onset of the X-ray bursts and the onset of the current pulses) and various recoil leader lengths.

5. Results

An important constraint is the time between the onset of the X-ray observations and the onset of the current pulse through the aircraft, which varies from 0.1 to $9.3 \mu\text{s}$, with an average value of $1.75 \mu\text{s}$. We assume that the recoil leader speed is similar to that of a dart leader, 10^7 m/s (Howard et al., 2010; Mazur & Moreaut, 1992; Rakov & Uman, 2003), as both leaders are initiated and propagate through an already existing semi-conductive channel. From this time span and a recoil leader speed of 10^7 m/s, we get a gap distance between the recoil leader and aircraft ranging from 1 to 93 m, with an average gap distance of 17.5 m. Using the GEANT4 model, we simulate X-ray spectra from electrons accelerated in the average gap of 17.5 m between the aircraft and the recoil leader, to get the spectral shapes for the different potentials. This was done using different leader-to-aircraft potentials ranging from 500 to 1,000 kV in steps of 250 kV and from 1,000 to 4,000 kV in steps of 500 kV.

Figure 8 shows the modeled spectra (dotted lines) for 500, 750, 1,000, 1,500, 2,000, 2,500, 3,000, 3,500, and 4,000 kV potentials in the top panel. The bottom panel shows the results of a likelihood analysis in black,

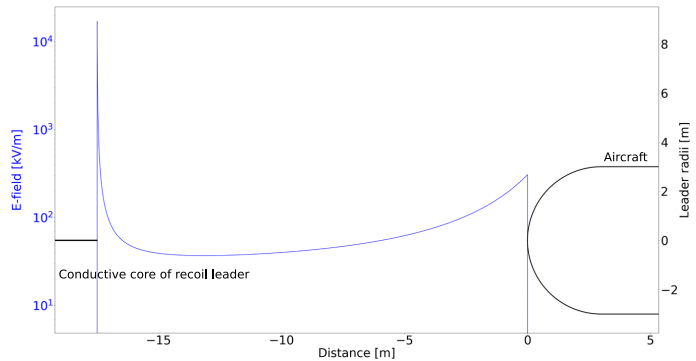


Figure 7. Electric field between lightning leader (left side) and aircraft (right side) in a 17.5 m gap, at 4 km altitude in a -24 kV/m ambient electric field.

performed as in Mailyan et al. (2016); see their Equation 1. According to this test, the best fit is given by minimizing $-2\log(L)$, and a difference in $-2\log(L)$ larger than 5 means that the minimum value, in this case 1,500 kV, is the preferred solution with a confidence level of 99%, compared to the values above 5 (the dotted black line). We consider all the solutions below the dotted line to be possible solutions (1,000 to 3,500 kV). In the plot, the black line is showing the calculated $-2\log(L)$ values subtracted by the minimum $-2\log(L)$ value. The bottom panel shows the values of the Pearson χ^2 test in blue (Hauschild & Jentschel, 2001). The test has a critical value of 12.6 (using a 95% threshold) shown as a dotted blue line. The test indicates that the models with potentials between 1,500 and up to 3,500 kV are good fits to our measured data. Due to instrumental limitations, only energies over 50 keV were included in the modeling and calculations of the fits. When calculating the Pearson χ^2 value, we have merged the 300 to 400 keV and the 400 to 500 keV bins, to get at least five measured counts in each bin (Eadie et al., 1971). The modeling also shows X-ray counts over 500 keV, which we have included in a large bin spanning from 500 to 4,000 keV. The calculated Pearson χ^2 values are not dependent on the size of the bins, and as such, the difference in bin widths does not affect the χ^2 value. The minimum potential to yield a fit was found to be 1,500 kV for the Pearson χ^2 analysis, while the likelihood analysis results in a minimum potential of 1,000 kV. As seen in Figure 8, the Pearson χ^2 value crosses the target threshold a bit before 1,500 kV, but we have chosen to use 1,500 kV as the lowest potential fit as this is the first tested value under the target threshold. The maximum potential to yield a fit was found to be 3,500 kV for both Pearson χ^2 and the likelihood analysis.

Using the GEANT4 model, we also estimate the number of 20 keV electrons needed to produce a single detected bremsstrahlung photon of minimum 50 keV for the different source potentials, within the 20° half angle. In a 1,500 kV potential, approximately 1.5×10^9 electrons were needed, while for a 3,500 kV potential, the amount of electrons needed is reduced to approximately 1.1×10^8 . The calculated luminosity for the observed recoil leaders with minimum energies of 50 keV are then found to vary from 2.8×10^8 electrons per microsecond for the 3,500 kV source potential up to 3.9×10^9 electrons per microsecond for electrons accelerated in the 1,500 kV source potential.

Using the ECM model, we estimate the relationship of the gap potential and the recoil leader lengths for certain chosen gap distances. This is done by keeping the gap distances fixed and adjusting the recoil leader length. The increase in length results in an increase of the gap potential. Figure 9 shows the relationship between the estimated gap potentials and recoil leader lengths for gap distances between 1 and 75 m, shown by the solid colored lines. The dotted black lines represent the minimum and maximum fit potentials (1,000 and 3,500 kV) found from the GEANT4 model that fit the observed spectrum.

From the intersects of the potential fits found from the GEANT4 model and the solid lines, we find the relationship between the gap and leader lengths for a given source potential. Figure 10 shows the relationship

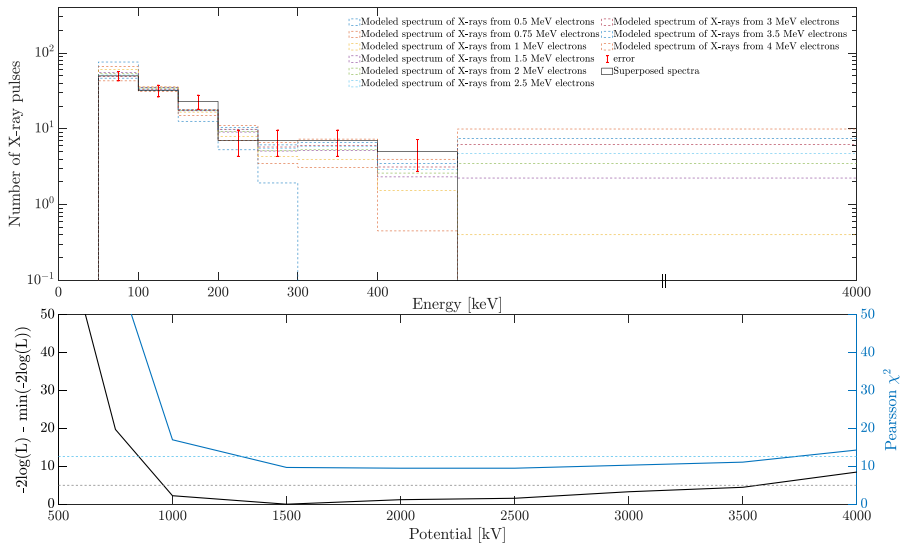


Figure 8. (Top) Observed (black) and modeled (dotted) X-ray spectra with minimum energies of 50 keV, with accompanying error bars in red. The modeled spectra sources are 500, 1,000, 1,500, 2,000, 2,500, 3,000, 3,500, and 4,000 keV electrons, accelerated in a 17.5 m gap between the recoil leader and the aircraft. (Bottom) Fit values for Pearson χ^2 and likelihood analysis, with accompanying dotted lines representing the target values.

between the gap and leader length for 1,500, 2,000, 2,500, 3,000, and 3,500 kV potentials, where the dotted line represents the average measured gap distance calculated from the time between the onset of the X-ray observation and the onset of the current pulse.

6. Discussion

The observed X-ray emissions are all found to be associated with the onset of recoil leaders during aircraft-triggered lightning. A total of 54 X-ray emissions was found, where the emissions consist of submicrosecond bursts of nanosecond-short X-ray pulses. The average burst lasts for $\sim 2 \mu\text{s}$ and consists of ~ 4.5 pulses, which is similar to the observations reported by Dwyer et al. (2004), who found submicrosecond bursts of X-rays associated with dart leaders with lightning.

The measured energy spectra extend up to 500 keV, with an average energy ~ 130 keV. X-rays with higher energies are ruled out, and not included as the few cases where these have been found the measured width of the X-ray pulse is found to be broader than for the calibration pulses, indicating that these X-ray pulses most likely consist of multiple X-rays of lower energies detected within a single sample period.

For the GEANT4 X-ray spectrum, we assumed a recoil leader speed similar to that of a dart leader as both are leaders developing in an already existing conductive lightning channel. With a recoil leader speed of 10^7 m/s combined with the average observed duration between the onset of the X-rays and the onset of the current pulse gives us a gap distance of 17.5 m. The time delays between the onset of the X-ray emissions and the onset of the current pulse vary from 0.1 to $9.3 \mu\text{s}$, where the majority of events have delays of less than $2 \mu\text{s}$. With the assumed recoil leader speed, this would make the gap distance between 1 and 93 m, with the majority of events having gap distances less than 20 m. As the measured

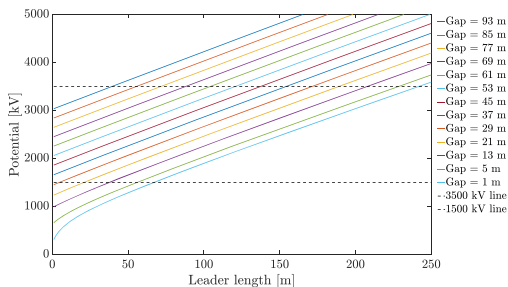


Figure 9. Gap potential as a function of leader length at different gap lengths. The dotted lines represent potentials of 1,500 and 3,500 kV, which is the minimum and maximum potential found to fit the superposed X-ray spectrum.

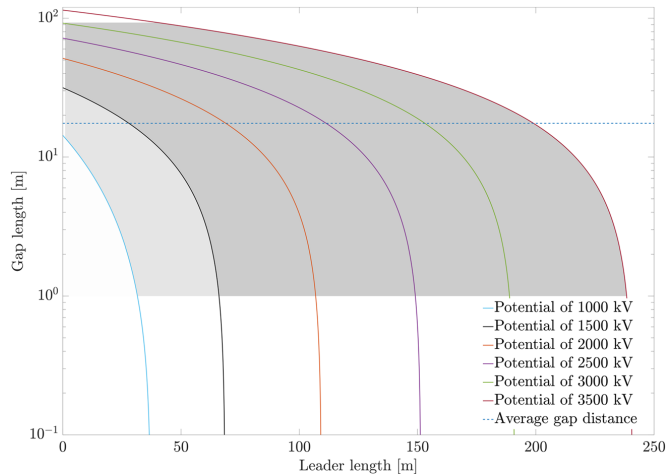


Figure 10. Potential limitations of the gap and leader lengths. The colored lines symbolize the potentials found to fit the superposed spectrum (1,000 up to 3,500 kV) from the second GEANT4 model. The gray areas represent our solution spaces with gap distances restricted by the minimum and maximum measured time between the onset of the X-rays and the onset of the current pulses, as well as the minimum and maximum potential found to fit the superposed spectrum (black/blue and red line). The light gray area is only valid from the likelihood analysis, while the darker gray area is valid for both the likelihood and Pearson χ^2 analysis. The dotted blue line represents the average gap distance also found from the time between onset times.

gap distance is only an indication of the distance to the X-ray source, we cannot conclude that this is the location of the recoil leader head. However, the recoil leader head is the most likely candidate to produce the observed X-rays, and the gap distance is therefore used as the location of the recoil leader head in our models. Changing the gap distance toward either the minimum or maximum value would result in a change of the hardness of the GEANT4 spectra, as the amount of air the X-rays would travel through would change. Another factor that would lead to a softer spectrum is if the X-rays were not produced by a monoenergetic source of electrons; however as seen in Figure 6, the majority of the modeled source electrons are accelerated to the full potential for a length equal to the assumed leader radius.

From our comparison of the measured X-ray spectrum to the GEANT4 X-ray spectra, we observe that the source of the X-rays is consistent with bremsstrahlung from electrons accelerated in potentials between 1,000 (likelihood)/1,500 (Pearson χ^2) and 3,500 kV. Based on the electron energies, it is thought that the initial seed electrons needed to produce the observed X-rays are most likely accelerated by the strong electric field in front of the recoil leader and streamers (cold runaway mechanism) as the leader travels back through the still conductive, but somewhat cooled leader channel toward the aircraft (Dwyer, 2004; Moss et al., 2006). The calculated electron luminosity for the X-ray source was found to be 3.9×10^9 electrons per microsecond for the minimum potential of 1,500 kV and 2.8×10^8 electrons per microsecond for the best fit potential of 3,500 kV, which is similar to what Saleh et al. (2009) and Schaal et al. (2012) report for X-ray sources in stepped and dart stepped leaders in rocket-triggered lightning. The calculated electron luminosities of the events are based on the assumption that the X-rays are emitted isotropically within the 20° half angle cone; if the emissions were completely isotropic, it would change the calculated luminosities, but it would not affect the modeled spectra and therefore not affect the constraint of the gap and leader lengths.

From the cutoff value in the superposed energy spectrum, we find that there is a limited amount of potentials from the second GEANT4 model that will fit the superposed spectrum. As the modeled potentials increase, so does the amount of modeled X-rays with energies over 500 keV, which increases our Pearson χ^2 and likelihood analysis values over the target values.

In Figure 10, we find a solution space for viable leader lengths and gap lengths. In the figure, the gap distances are constrained by the observed minimum and maximum times between the onset of the X-ray bursts and the onset of the current pulses (1 to 93 m with the assumed dart leader speed of 10^7 m/s). Furthermore, the solution space has a lower and upper constraint found from the lowest and highest potential fit from the second GEANT4 model. These potentials limit the leader length to between 1 and ~ 240 m. Together, these four constraints limit our solution space to the gray-shaded areas. The model does not give a preferred solution within this solution space; however, from the average time between the onset of the X-ray bursts and the onset of the current pulses, we find the average gap distance (dotted blue line) to be 17.5 m, which limits the average leader length to between ~ 1 (likelihood)/25 (Pearson χ^2) to 200 m depending on selection of fitting method.

Data Availability Statement

The supporting data used in this paper are published on Zenodo (<http://doi.org/10.5281/zenodo.3878590>).

Acknowledgments

This study was supported by the European Research Council under the European Union's Seventh Framework Programme (FP7/2007–2013)/ERC Grant Agreement 320839 and the Research Council of Norway under Contracts 208028/F50 and 223252/F50.

References

- Agostinelli, S., Allison, J., Amako, K., Apostolakis, J., Araujo, H., Arce, P., et al. (2003). Geant4—A simulation toolkit. *Nuclear Instruments and Methods in Physics Research Section A: Accelerators, Spectrometers, Detectors and Associated Equipment*, 506(3), 250–303. [https://doi.org/10.1016/S0168-9002\(03\)01368-8](https://doi.org/10.1016/S0168-9002(03)01368-8)
- Allison, J., Amako, K., Apostolakis, J., Araujo, H., Arce Dubois, P., Asai, M., et al. (2006). Geant4 developments and applications. *IEEE Transactions on Nuclear Science*, 53(1), 270–278. <https://doi.org/10.1109/TNS.2006.869826>
- Allison, J., Amako, K., Apostolakis, J., Arce, P., Asai, M., Aso, T., et al. (2016). Recent developments in Geant4. *Nuclear Instruments and Methods in Physics Research Section A: Accelerators, Spectrometers, Detectors and Associated Equipment*, 835, 186–225. <https://doi.org/10.1016/j.nima.2016.06.125>
- Boissin, J. F., Flourens, F., de Boer, A., Bardet, M., Herve, A., Perez, G., & Riccio, L. (2012). In-flight lightning measurements and reconstruction on a metallic and composite aircraft, 2012 ESA Workshop on Aerospace EMC, Venice, pp. 1–6.
- de Boer, A., Bardet, M., Boissin, J. F., van Deursen, A. P. J., Flourens, F., & Herve, A. (2013). In-flight Lightning Damage Assessment System (ILDAS): Further in-flight verification, with multi-sensor configuration. *Proceedings of the 2013 International Conference on Lightning and Static Electricity (ICOLSE)*, 18–20 September 2013, Seattle, Washington. *Conference paper*.
- de Boer, A., Bardet, M., Escure, C., Peres, G., Srithammavanh, V., Abboud, K., et al. (2011). In-flight Lightning Damage Assessment System (ILDAS): Initial in-flight lightning tests and improvement of the numerical methods. *Proceedings of the International Conference on Lightning and Static Electricity 2011 (ICOLSE 2011)*, 6–8 September 2011, Oxford, UK. *Conference paper*.
- de Boer, A., Boissin, J. F., van Deursen, A. P. J., Flourens, F., Herve, A., & Zwemmer, R. (2013). In-flight Lightning Damage Assessment System (ILDAS): In-flight verification of multi-sensor measurement. *Proceedings of the 2013 International Conference on Lightning and Static Electricity (ICOLSE)*, 18–20 September 2013, Seattle, Washington. *Conference paper*.
- de Boer, A., Flourens, F., Herv, A., Bardet, M., & Boissin, J. F. (2015). ILDAS2: From the laboratory to operations—Benefits and performance of the In-flight Lightning Damage Assessment System in support of flight test campaigns. *Proceedings of the 2015 International Conference on Lightning and Static Electricity (ICOLSE 2015)*, 9–11 September 2015, Toulouse, France. *Conference paper*. <https://doi.org/10.1049/ic.2015.0198>
- Deursen, A. (2011). Inductive sensor for lightning current measurement, fitted in aircraft windows—Part II: Measurements on an a320 aircraft. *Sensors Journal, IEEE*, 11, 205–209. <https://doi.org/10.1109/JSEN.2010.2055559>
- Dwyer, J. R. (2003). Energetic radiation produced during rocket-triggered lightning. *Science*, 299, 694–698.
- Dwyer, J. R. (2004). Implications of X-ray emission from lightning. *Geophysical Research Letters*, 31, L12102. <https://doi.org/10.1029/2004GL019795>
- Dwyer, J. R., Rassoul, H. K., Al-Dayeh, M., Caraway, L., Chrest, A., Wright, B., & Kozak, E. (2005). X-ray bursts associated with leader steps in cloud-to-ground lightning. *Geophysical Research Letters*, 32, L01803. <https://doi.org/10.1029/2004GL021782>
- Dwyer, J. R., Rassoul, H. K., Al-Dayeh, M., Caraway, L., Wright, B., & Chrest, A. (2004). Measurements of X-ray emission from rocket-triggered lightning. *Geophysical Research Letters*, 31, L12102. <https://doi.org/10.1029/2004GL019795>
- Dwyer, J. R., Schaal, M., Rassoul, H. K., Uman, M. A., Jordan, D. M., & Hill, D. (2011). High-speed X-ray images of triggered lightning dart leader. *Journal of Geophysical Research*, 116, D20208. <https://doi.org/10.1029/2011JD015973>
- Dwyer, J., Smith, D., & Cummer, S. (2012). High-energy atmospheric physics: Terrestrial gamma-ray flashes and related phenomena. *Space Science Reviews*, 173, 133–196.
- Eadie, W. T., Drijard, D., James, F. E., Roos, M., & Sadoulet, B. (1971). *Statistical methods in experimental physics*. Amsterdam: North-Holland Publishing.
- Fisher, B. D., Brown, P. W., Plumer, J. A., & Wunschel, A. J. Jr. (1988). Final results of the NASA storm hazards program. *Proceedings of the 1988 International Conference on Lightning and Static Electricity (ICOLSE 1988)*, 19–21 April 1988, Oklahoma City, Oklahoma. *Conference paper*.
- Harrington, R. F. (1993). *Field computation by moment methods*. New Jersey: IEEE Press.
- Hauschild, T., & Jentschel, M. (2001). Comparison of maximum likelihood estimation and chi-square statistics applied to counting experiments. *Nuclear Instruments and Methods in Physics Research Section A: Accelerators, Spectrometers, Detectors and Associated Equipment*, 457(1–2), 384–401. [https://doi.org/10.1016/S0168-9002\(00\)00756-7](https://doi.org/10.1016/S0168-9002(00)00756-7)
- Hervé, A., Peres, G., de Boer, A., Bardet, M., Flourens, F., & Boissin, J. F. (2014). In-flight Lightning Damage Assessment System (ILDAS): Diagnostic performance assessment with in-flight lightning data. *2014 International Symposium on Electromagnetic Compatibility, 1–4 September 2014, Gothenburg, Sweden* (pp. 589–594). Institute of Electrical and Electronics Engineers. <https://doi.org/10.1109/EMCEurope.2014.6930974>

- Howard, J., Uman, M. A., Biagi, C., Hill, D., Jerauld, J., Rakov, V. A., et al. (2010). RF and X-ray source locations during the lightning attachment process. *Journal of Geophysical Research*, *115*, D06204. <https://doi.org/10.1029/2009JD012055>
- Kelley, N., Smith, D. M., Dwyer, J. R., Splitt, M., Lazarus, S., Martinez-McKinney, F., et al. (2015). Relativistic electron avalanches as a thunderstorm discharge competing with lightning. *Nature Communications*, *6*, 1–7. <https://doi.org/10.1038/ncomms8845>
- Kochkin, P., Sarria, D., Skeie, C. A., van Deursen, A. P. J., de Boer, A. I., Bardet, M., et al. (2018). In-flight observation of positron annihilation by ILDAS. *Journal of Geophysical Research: Atmospheres*, *123*, 8074–8090. <https://doi.org/10.1029/2018JD028337>
- Kochkin, P., van Deursen, A. P. J., de Boer, A., Bardet, M., & Boissin, J.-F. (2015). In-flight measurements of energetic radiation from lightning and thunderclouds. *Journal of Physics D: Applied Physics*, *48*, 425,202. <https://doi.org/10.1088/0022-3727/48/42/425202>
- Kochkin, P., van Deursen, A. P. J., Marisaldi, M., de Boer, A. I., Bardet, M., Allasia, C., et al. (2017). In-flight observation of gamma ray glows by ILDAS. *Journal of Geophysical Research: Atmospheres*, *122*, 12,801–12,811. <https://doi.org/10.1002/2017JD027405>
- Lalande, P., Bondiou-Clergerie, A., & Laroche, P. (1999). Analysis of available in-flight measurements of lightning strikes to aircraft. *SAE Technical Paper Series*, *724*. <https://doi.org/10.4271/1999-01-2397>
- Laroche, P., Blanchet, P., Delannoy, A., & Issac, F. (2012). Experimental studies of lightning strikes to aircraft. *Aerospace Lab Journal*, *5*, 1–13.
- Lehtinen, N. G. (2012). A waveguide model of the return stroke channel with a “metamaterial” corona. *Radio Science*, *47*, RS1003. <https://doi.org/10.1029/2011RS004749>
- Mailyan, B. G., Briggs, M. S., Cramer, E. S., Fitzpatrick, G., Roberts, O. J., Stanbro, M., et al. (2016). The spectroscopy of individual terrestrial gamma-ray flashes: Constraining the source properties. *Journal of Geophysical Research: Space Physics*, *121*, 11,346–11,363. <https://doi.org/10.1002/2016JA022702>
- Mazur, V. (1989a). A physical model of lightning initiation on aircraft in thunderstorms. *Journal of Geophysical Research*, *94*, 3326–3340. <https://doi.org/10.1029/JD094ID03p03326>
- Mazur, V. (1989b). Triggered lightning strikes to aircraft and natural intracloud discharges. *Journal of Geophysical Research*, *94*(D3), 3311–3325. <https://doi.org/10.1029/JD094ID03p03311>
- Mazur, V. (2002). Physical processes during development of lightning flashes. *Applied Physics*, *3*, 1393–1409. [https://doi.org/10.1016/S1631-0705\(02\)01412-3](https://doi.org/10.1016/S1631-0705(02)01412-3)
- Mazur, V., & Moreaut, J. P. (1992). Aircraft-triggered lightning: Processes following strike initiation that affect aircraft. *Journal of Aircraft*, *29*(4), 575–580. <https://doi.org/10.2514/3.46204>
- Mazur, V., & Ruhnke, L. H. (1993). Common physical processes in natural and artificially triggered lightning. *Journal of Geophysical Research*, *98*, 12,913–12,930. <https://doi.org/10.1111/j.1555-2934.2009.01042.x>
- Mazur, V., Ruhnke, L. H., Warner, T. A., & Orville, R. E. (2013). Recoil leader formation and development. *Journal of Electrostatics*, *71*, 763–768. <https://doi.org/10.1016/j.elstat.2013.05.001>
- McCarthy, M., & Parks, G. K. (1985). Further observations of X-rays inside thunderstorms. *Geophysical Research Letters*, *12*, 393–396. <https://doi.org/10.1029/GL012i006p00393>
- Miller, E. (1968). Synopsis of a thunderstorm research program (Roughrider) for 1966–1967 (*Technical Report ASD-TR-68-29*).
- Montanyà, J., Fabró, F., van der Velde, O., Romero, D., Solà, G., Hermoso, J. R., et al. (2014). Registration of X-rays at 2500 m altitude in association with lightning flashes and thunderstorms. *Journal of Geophysical Research: Atmospheres*, *119*, 1492–1503. <https://doi.org/10.1002/2013JD021011>
- Moore, C. B., Eack, K. B., Aulich, G. D., & Rison, W. (2001). Energetic radiation associated with lightning stepped-leaders. *Geophysical Research Letters*, *28*, 2141–2144. <https://doi.org/10.1029/2001GL013140>
- Moreaut, J. P., Alliot, J. C., & Mazur, V. (1992). Aircraft lightning initiation and interception from in situ electric measurements and fast video observations. *Journal of Geophysical Research*, *97*(D14), 15,903–15,912. <https://doi.org/10.1029/92JD01077>
- Moss, G. D., Pasko, V. P., Liu, N., & Veronis, G. (2006). Monte Carlo model for analysis of thermal runaway electrons in streamer tips in transient luminous events and streamer zones of lightning leaders. *Journal of Geophysical Research*, *111*, A02307. <https://doi.org/10.1029/2005JA011350>
- Ogawa, T., & Brook, M. (1964). The mechanism of the intracloud lightning discharge. *Journal of Geophysical Research*, *69*(24), 5141–5150. <https://doi.org/10.1029/JZ069i024p05141>
- Østgaard, N., Christian, H. J., Grove, J. E., Sarria, D., Mezentsev, A., Kochkin, P., et al. (2019). Gamma ray glow observations at 20-km altitude. *Journal of Geophysical Research: Atmospheres*, *124*, 7236–7254. <https://doi.org/10.1029/2019JD030312>
- Parks, G. K., Mauk, B. H., Spiger, R., & Chin, J. (1981). X-ray enhancements detected during thunderstorm and lightning activities. *Geophysical Research Letters*, *8*, 1176–1179. <https://doi.org/10.1029/GL008i011p01176>
- Rakov, V. A., & Uman, M. A. (2003). *Lightning: Physics and effects*. Cambridge: Cambridge University Press.
- Royal Netherlands Aerospace Laboratory (2015). Accurate measurements during multiple lightning strikes. <https://ildas.nlr.nl>
- Saleh, Z., Dwyer, J., Howard, J., Uman, M., Bakhtiari, M., Concha, D., et al. (2009). Properties of the X-ray emission from rocket-triggered lightning as measured by the Thunderstorm Energetic Radiation Array (TERA). *Journal of Geophysical Research*, *114*, D17210. <https://doi.org/10.1029/2008JD011618>
- Schaal, M. M., Dwyer, J. R., Saleh, Z. H., Rassoul, H. K., Hill, J. D., Jordan, D. M., & Uman, M. A. (2012). Spatial and energy distributions of X-ray emissions from leaders in natural and rocket triggered lightning. *Journal of Geophysical Research*, *117*, D15201. <https://doi.org/10.1029/2012JD017897>
- Skelved, A. B., Østgaard, N., Mezentsev, A., Lehtinen, N., & Carlson, B. (2017). Constraints to do realistic modeling of the electric field ahead of the tip of a lightning leader. *Journal of Geophysical Research: Atmospheres*, *122*, 8120–8134. <https://doi.org/10.1002/2016JD026206>
- Uman, M. A., & Rakov, V. A. (2003). The interaction of lightning with airborne vehicles. *Progress in Aerospace Sciences*, *39*(1), 61–81. [https://doi.org/10.1016/S0376-0421\(02\)00051-9](https://doi.org/10.1016/S0376-0421(02)00051-9)
- van Deursen, A. P. J., de Boer, A., Bardet, M., & Boissin, J. F. (2013). Window sensor for the a350 and a380 aircraft, *2013 International Conference on Electromagnetics in Advanced Applications (ICEAA)* (pp. 1000–1003).
- Zwemmer, R., Bardet, M., de Boer, A., Hardwick, J., Hawking, D. K. M., Latorre, M., et al. (2009). In-flight Lightning Damage Assessment System (ILDAS): results of the concept prototype tests. *Proceedings of the 2009 International Conference on Lightning and Static Electricity (ICOLSE)*, 15–17 September 2009, Pittsfield, Massachusetts. *Conference paper*.

Paper II

Production of Terrestrial Gamma-ray Flashes During the Early Stages of Lightning Flashes

A. Lindanger, C. A. Skeie, M. Marisaldi, I. Bjørge-Engeland, N. Østgaard, A. Mezentsev, V. Reglero, O. Chanrion, T. Neubert

Journal of Geophysical Research: Atmospheres, **127/8** (2022)



RESEARCH ARTICLE

10.1029/2021JD036305

Key Points:

- VLF radio and optical measurements show that upward TGFs are typically produced in the beginning of a lightning flash
- Stacking analysis confirms an excess of lightning activity 150–750 ms after the TGFs
- When a TGF is simultaneous to a lightning stroke, the enhanced activity after is usually co-located with the first lightning stroke

Supporting Information:

Supporting Information may be found in the online version of this article.

Correspondence to:

A. Lindanger,
anders511@protonmail.com

Citation:











Lindanger, A., Skeie, C. A., Marisaldi, M., Bjørge-Engeland, I., Østgaard, N., Mezentsev, A., et al. (2022). Production of terrestrial gamma-ray flashes during the early stages of lightning flashes. *Journal of Geophysical Research: Atmospheres*, 127, e2021JD036305. <https://doi.org/10.1029/2021JD036305>

Received 3 DEC 2021
Accepted 31 MAR 2022

© 2022. The Authors.

This is an open access article under the terms of the [Creative Commons Attribution License](https://creativecommons.org/licenses/by/4.0/), which permits use, distribution and reproduction in any medium, provided the original work is properly cited.

Production of Terrestrial Gamma-Ray Flashes During the Early Stages of Lightning Flashes

A. Lindanger¹ , C. A. Skeie¹ , M. Marisaldi^{1,2} , I. Bjørge-Engeland¹ , N. Østgaard¹ , A. Mezentsev¹ , D. Sarria¹ , N. Lehtinen¹ , V. Reglero³, O. Chanrion⁴ , and T. Neubert⁴ 

¹Department of Physics and Technology, Birkeland Centre for Space Science, University of Bergen, Bergen, Norway, ²INAF-OAS Bologna, Bologna, Italy, ³University of Valencia, Paterna, Spain, ⁴National Space Institute, Technical University of Denmark, Kgs. Lyngby, Denmark

Abstract Terrestrial Gamma-ray Flashes (TGFs) are short emissions of high energy photons associated with thunderstorms. It has been known since the discovery of TGFs that they are associated with lightning, and several case studies have shown that the TGFs are produced at the initial phase of the lightning flash. However, it has not been tested whether this is true in general. By using the largest TGF sample up to date, combined with ground-based radio lightning detection data, we perform a statistical study to test this. One of the TGF missions is the Atmosphere-Space Interactions Monitor (ASIM) consisting of the innovative combination of X- and gamma-ray detectors, optical photometers and cameras. This allows us to investigate the temporal relation between gamma-rays produced by TGFs and the optical signal produced by lightning discharges. Based on stacking analysis of the TGF sample and ground-based measurements of associated lightning activity, together with the high temporal resolution of the optical signal from the ASIM photometers, it is shown that TGFs are produced in the beginning of the lightning flashes. In addition, for a significant fraction of the TGFs, the lightning activity detected in radio is enhanced in an interval between 150 and 750 ms following the TGFs, and is co-located with the lightning associated with the TGFs. The enhanced lightning activity is not evident in a randomly selected sample of flashes. This indicates that the activity between 150 and 750 ms is a characteristic property of a significant fraction of flashes that start with a TGF.

1. Introduction

Terrestrial gamma-ray flashes (TGFs) are sub-millisecond bursts of energetic photons up to several tens of MeV produced in the atmosphere. The energy spectra of TGFs are compatible with the Relativistic Runaway Electron Avalanche (RREA) process followed by bremsstrahlung emissions (Dwyer, 2003; Dwyer & Smith, 2005; Gurevich et al., 1992; Lindanger et al., 2021; Mailyan et al., 2016). The connection between TGFs and thunderstorm regions has been suggested since the first TGFs were detected by the BATSE instrument onboard the Compton Gamma-ray Observatory (Fishman et al., 1994). TGFs have since been detected from space by RHESSI (Smith et al., 2005), Fermi (Briggs et al., 2013), AGILE (Marisaldi et al., 2010), BeppoSAX (Ursi et al., 2017), the RELEC space experiment on the Vernov satellite (Bogomolov et al., 2017), and ASIM (Østgaard, Neubert, et al., 2019).

Case studies have shown that TGFs can be observed in association with positive Intra-Cloud (IC+) lightning, and several case studies have shown that TGFs are typically produced in the initial phase of lightning flashes during the upward propagation of leaders (Cummer et al., 2015; Lu et al., 2010; Shao et al., 2010; Stanley et al., 2006; Østgaard et al., 2013). Connaughton et al. (2010, 2013) used very low frequency (VLF) radio atmospheric, so-called sferics, produced by lightning and detected by the World Wide Lightning Location Network (WWLLN) together with TGFs detected by Fermi to show that a significant fraction of TGFs is simultaneous with a sferic detection within a few hundred microseconds. This strict association has been confirmed by RHESSI (Mezentsev et al., 2016) and AGILE (Lindanger et al., 2020; Marisaldi et al., 2015). Connaughton et al. (2013) inferred that the radio signal simultaneous with the TGF is produced by the TGF-current itself, and Dwyer and Cummer (2013) modeled this. Østgaard et al. (2021), using a combination of ASIM gamma-ray data, optical data and LF-radio measurements concluded that the TGF-associated radio signal was produced by either the hot-leader lightning channel or the TGF, or a combination of the two. Smith et al. (2016) identified three types of associations between TGFs and sferics; simultaneous association, few milliseconds difference, and those where the radio signals are hundreds of milliseconds after the TGF. The last category will be further investigated in this study.

This likely places the TGF at the beginning of a lightning flash, during the upward propagation of a leader that continues propagating after the TGF. However, this is only based on case studies and has not been shown for a large sample of TGFs. As recent scientific efforts have been focused on the “simultaneity” of TGFs and the temporally closest radio measurement (Connaughton et al., 2010, 2013; Cummer et al., 2011; Lindanger et al., 2020; Mailyan et al., 2020; Marisaldi et al., 2015; Mezentsev et al., 2016), this work will take a step back and focus on TGFs and *all* lightning detections associated to the TGF on 100’s ms scale. This will follow up the enhanced lightning activity detected hundreds milliseconds after the TGFs reported by Omar et al. (2014); Smith et al. (2016). Using a large data set of TGF catalogs together with ground-based lightning radio data and optical data from ASIM, we will answer the question: when does the TGF occur in the sequence of discharges constituting a lightning flash and are there any special characteristics with those flashes?

2. Data and Method

This study uses four TGF catalogs from different instruments, lightning data from WWLLN and GLD360, and optical data from the Modular Multispectral Imaging Array (MMIA) instrument onboard ASIM. The TGF catalogs are obtained from the TGF detecting space missions RHESSI, Fermi, AGILE, and ASIM. There are 2824 TGFs (August 2004 to November 2013) from the RHESSI TGF catalog (Smith et al., 2020), 4774 TGFs (August 2008 to July 2016) from the first Fermi-GBM TGF catalog (Roberts et al., 2018), 3473 TGFs (March 2015 to October 2020) from the 3rd AGILE TGF catalog (Lindanger et al., 2020; Maiorana et al., 2020), and 729 ASIM TGFs (June 2018 to September 2020) available from <https://asdc.space.dtu.dk>. The ASIM instrument is described in detail in Chanrion et al. (2019); Neubert et al. (2019); Østgaard, Balling, et al. (2019). TGFs detected by the same instrument occurring within 5 ms of the previous TGF are removed so that multi-pulse TGFs are counted as a single entry, corresponding to the first TGF. The timing resolution provided by the RHESSI TGF catalog is 1 ms and the absolute timing accuracy is corrected to ~ 1 ms by the timing correction provided by Mezentsev et al. (2016). The 3rd AGILE TGF catalog is updated including WWLLN-identified TGFs up to October 2020. We also remove TGFs detected by AGILE between July 2015 and December 2017 because AGILE experienced a degradation of the absolute timing accuracy during that period (Lindanger et al., 2020).

Lightning data are obtained from WWLLN (Rodger et al., 2009) and GLD360 provided by Vaisala Inc. (Said & Murphy, 2016). Both lightning networks detect sferics produced by lightning discharges and provides geolocation and timestamps of the sferics. GLD360 also provides peak current values for their detections. WWLLN data from August 2004 and onward are compared to the RHESSI, Fermi, AGILE, and ASIM TGF catalogs. Abarca et al. (2010) and Hutchins et al. (2012) found the location accuracy of WWLLN to be ~ 5 km for the continental United States, and Østgaard et al. (2013) assumed a global WWLLN location accuracy of 15 km. Comparing WWLLN with Lightning Imaging Sensor (LIS), Bürgesser (2017) estimated a detection efficiency between 1% and 10% for continental regions, and 20% for oceanic regions worldwide. Through the ASIM Science Data Center, GLD360 data are only available for the ASIM mission, therefore it will be used only in association with ASIM data. Using one month of NLDN data over the United States, Said and Murphy (2016) reported the median location accuracy of GLD360 to be ~ 2 km and the 90th percentile is ~ 6 km. The detection efficiency was estimated to be $\sim 80\%$ for CG flashes and $\sim 45\%$ for IC flashes.

The time difference between the TGF and the sferic is defined by Equation 1. The time of the sferic is the time of lightning discharge. The propagation time of photons traveling from the lightning location to the satellite is calculated assuming a TGF production altitude of 12 km. Moving three km down or up is only a maximum time difference of 10 μ s.

$$\delta t = \text{time}_{\text{sferic}} + \text{time}_{\text{propagation}} - \text{time}_{\text{TGF}} \quad (1)$$

For all the TGFs we keep track of: TGF time and its associated lightning information including the radial distance between the subsatellite point and the location of the sferic source lightning discharge, δt of all sferics, δt of the temporally closest sferic match, and the radial distance between the temporally closest sferic match and the other surrounding sferics. The radial distance is the distance along the surface of the Earth between two coordinates.

Due to instrument sensitivity and efficiency of the various instruments most TGFs are detected within ~ 500 km from the subsatellite point (Collier et al., 2011; Cummer et al., 2005; Lindanger et al., 2020; Marisaldi et al., 2019; Smith et al., 2016). Therefore, we only consider sferics within 500 km from the subsatellite point to ensure a

Table 1
Overview of the Data Sets and the Sferic Match Criteria Corresponding to Each Space Mission

Instrument	Lightning network	Sferic match criteria	Number of TGFs with sferic match
RHESSI	WWLLN	$ \delta t < 1$ ms	441
Fermi	WWLLN	$ \delta t < 0.2$ ms	948
AGILE	WWLLN	$ \delta t < 0.2$ ms	619
ASIM	WWLLN	0 ms $< \delta t < 30$ ms	230
ASIM	GLD360	0 ms $< \delta t < 30$ ms	477

Note. We require the sferic match to be within 500 km from the subsatellite point.

high signal-to-noise ratio in the stacking analysis. We define a sferic match as the sferic with the smallest $|\delta t|$ value but not larger than the following sferic match criteria. The sferic match criteria depend on the absolute timing accuracy of the instrument we consider. For RHESSI we require δt to be within ± 1 ms, and for Fermi and AGILE we use a sferic match criteria of ± 0.2 ms as their onboard clocks are on microsecond level. The absolute timing accuracy of ASIM varies stochastically between 0 and 30 ms and we chose this as the sferic match criterion. The location of the sferic match is assumed to be the production location of the TGF. An overview of the datasets and their sferic match criteria is shown in Table 1.

This analysis also includes optical data from the MMIA instrument onboard ASIM. MMIA consists of two cameras providing 12 images per second, and three high-speed photometers with a 100 kHz sampling rate. The instrument is described in detail in Chanrion et al. (2019). The two cameras are sensitive in 337.0 and 777.4 nm bands, and the photometers are sensitive in 337.0 nm,

180–240 nm (UV), and 777.4 nm bands. The bandwidths of 337 and 777.4 nm cameras are 5 and 3 nm, respectively. The bandwidths of 337 and 777.4 nm photometers are 4 and 5 nm, respectively. The 777 nm emission is due to atomic oxygen in hot lightning channels and is weakly absorbed in the atmosphere. The UV is strongly absorbed in the atmosphere and is therefore most sensitive to high altitude phenomena such as Elves and other Transient Luminous Events (TLEs). The 337 nm is most sensitive to lightning but will also see some signal from TLEs as it is close to the UV band. The 337 nm is more absorbed in the atmosphere compared to 777 nm. MMIA data acquisition is triggered, and a trigger is generated if the signal is larger than a threshold over a dynamically calculated background. There is also a cross-trigger system that stores MMIA data if the companion instrument, the Modular X- and Gamma-ray Sensor (MXGS), onboard ASIM triggers independently of the MMIA signal. MMIA is only active during nighttime, meaning that we only have optical data for TGFs detected during nighttime. The cameras and the photometers field of view (FOV) is a square 80° diagonal, except the UV photometer that has a circular 80° full cone angle. The relative timing accuracy between MXGS and MMIA was ± 80 μ s before March 2019 and ± 5 μ s after.

In this study we investigate 71 ASIM detected TGF events with MMIA optical data. These 71 events have been found by Skeie et al., manuscript in preparation, to have optical data associated with the detected TGFs, that is, a clean sample with the TGF produced well inside MMIA FOV and photometer data associated to the TGF. This sample was determined using the photometers, cameras, the high and low energy detector data, as well as lightning sferic activity and TGFs characteristics. For 45 of the TGF events it was also possible to use the GLD360-detected sferics to correct the absolute timing of ASIM down to a few milliseconds, by aligning several photometer pulses with the sferics, similar to what was done in Heumesser et al. (2021); Østgaard et al. (2021); Maiorana et al. (2021).

3. Results

3.1. Stacking Analysis of Lightning Data

To determine whether the TGFs are in the beginning of the lightning flash we did a stacking analysis of sferics. Figure 1 shows a stacking plot of sferics relative to the time of the TGFs, as detected by RHESSI, Fermi, AGILE, and ASIM. The right panels are a close-up version of the left panels. The black histograms shows all sferics without applying the sferic match criteria of Table 1. The first peak at $\delta t \approx 0$ consists mostly of sferics associated with the TGFs. We emphasize that we include *all* sferics within 500 km from the subsatellite point in the stacking analysis, not just the temporally closest sferic. Using a 50 ms bin size means that sferics 25 ms before and after the TGF will be included in the central bin. This implies that the bin will also include some sferics that are not directly associated to the TGF. Note also that the lightning networks sometimes detect the same sferic several times. Therefore, the central bin has more counts than the number of TGFs stacked. Note the enhanced signal from sferics between ~ 150 and ~ 750 ms, evident for all instruments. We will call this enhanced signal the “second peak” hereafter. The blue histograms are a sub-selection of events that have a sferic match (Table 1) within 500 km of the subsatellite point, and where only sferics within 20 km radius of the sferic match are included. A schematic of the selection of the two histograms is shown in Figure 2 and the 20 km limit will

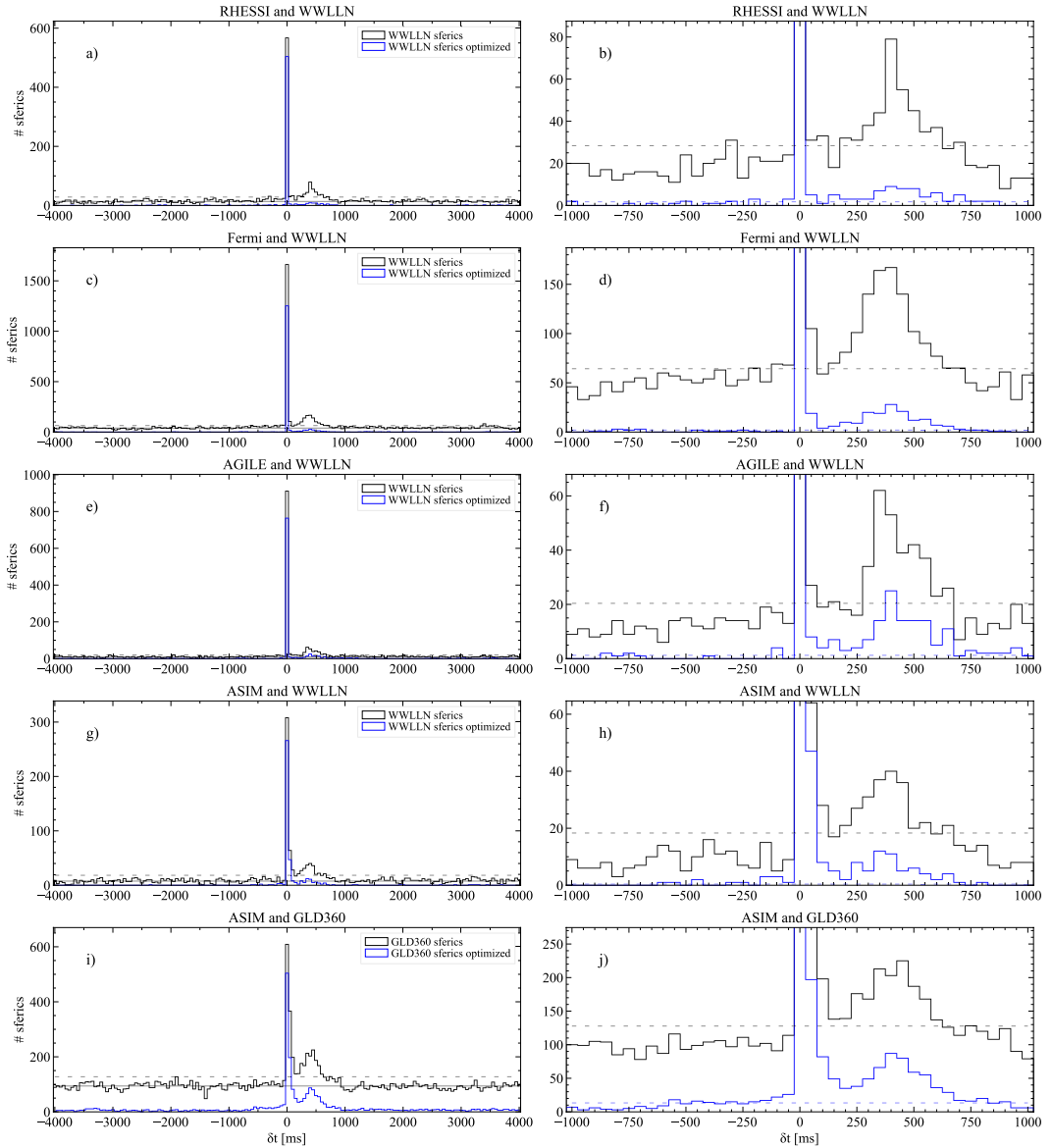


Figure 1. Stacking analysis of sferics as a function of time. $\delta t = 0$ is the TGF time (Equation 1). The right panels are a close-up version of the left panels. The black histograms show *all* sferics within 500 km and the blue histograms show the sferics within 20 km of the TGF-sferic match (Table 1). The selection is illustrated in Figure 2. The solid black line in the left panels is the average background during δt between -4 to -1 s and the black dashed line marks the 3σ level above background assuming Poisson distribution in counts per bin. The dashed blue line in the right panels is 3σ above the background for the blue histograms. Note that the dashed blue line is very close to the x -axis for (b, d, f, and h). The bin size is 50 ms.

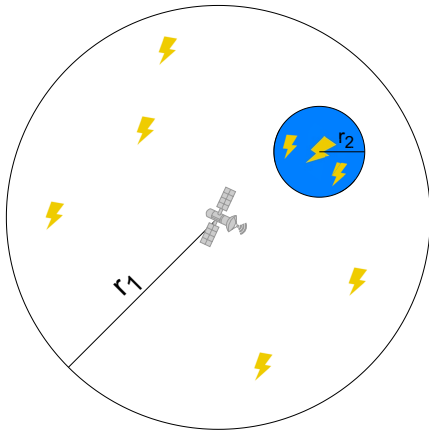


Figure 2. Figure illustrating the selection of sferics for the black and blue histograms in Figure 1. The black histograms consist of all sferics within $r_1 = 500$ km of the subsatellite point. The blue histograms consist of sferics within $r_2 = 20$ km of the sferic match in the middle of the blue circle in the illustration. The illustration is not to scale.

be justified in the next paragraph. The blue histograms show a higher signal-to-noise ratio for the second peak than the black histogram. The 3σ significance level is shown as a dashed line for the black and the blue histograms. Figure S1 in Supporting Information S1, shows a zoomed view of the same data as in Figures 1c and 1e with a bin size of $50 \mu\text{s}$ instead of a bin size of 50 ms as in Figure 1.

Figure 3 shows the radial distance between the sferic match and the sferics in the second peak, where the second peak is defined to be δt between 150 and 750 ms. The bin size is chosen so that the area corresponding to each bin is constant, meaning that $A_1 = \pi r_1^2 = A_n = \pi(r_n^2 - r_{(n-1)}^2) = \text{constant}$, where n is the bin index. We see that there is an excess of sferics, within 5–10 km of the location of the sferic match, showing that most activity related to the lightning flash starting with a TGF occur within a radial distance of 20 km. This result is the reason for the 20 km limit to enhance the signal-to-noise ratio in the second peak for the blue histograms in Figure 1.

3.2. Analysis of Optical Data

A sample of 71 ASIM detected TGF events with associated optical data is used to investigate the lightning activity at times close to the TGFs. The TGF production locations are inside the FOV of MMIA. For 13 of the events, several cells were active at the same time of the TGF, which made it impossible to determine at what time they occur in the progression of a flash from measurements by the photometers. One example is shown in Figure S2 in Supporting Information S1. The 13 events are removed from the analysis and we are left with 58 TGF events.

The TGF precedes the large MMIA optical pulse associated with the TGF in 57 cases. Some of the TGFs have a weak optical signal a few milliseconds before the large optical pulse associated with the TGF. This is compatible with lightning leader propagation (Cummer et al., 2015) and has been termed preactivity in earlier studies (Heumesser et al., 2021; Neubert et al., 2020; Østgaard, Neubert, et al., 2019; Østgaard et al., 2021). For the 57 TGFs there are either only one large optical pulse following the TGF (42 events), or there are several optical pulses (15 events) following the pulse associated with the TGF. An example of these is shown in Figure 4. In Figures 4a–4d it is clear that there are no signals detected by MMIA up to ~ 100 ms before the TGF. The TGF is indicated in (a and b) as a magenta vertical line at time = 0. There is a clear 337 and 777 nm peak associated with the TGF, and following optical pulses are evident in both photometers up to ~ 400 ms after the TGF. The cropped camera (CHU1 and CHU2) images in Figures 4f and 4g show only one active area that corresponds well with the position of the sferic associated with the TGF in Figure 4e).

In Figure 5, photometer data for 777 nm are shown for 8 (out of 15) TGF events with several pulses following the first pulse associated with the TGF. The TGF time is centered at time = 0, and it is evident that there is no lightning activity before the TGF.

In one of the 58 TGF events, the TGF seems to be in the middle of the flash where we have three optical pulses between 70 and 50 ms before the TGF, not placing the TGF in the beginning of the flash. This TGF event is shown in Figure S3 in Supporting Information S1, and will be discussed later.

4. Discussion

4.1. The TGF Time Relative to the Lightning Flash

Considering first the results of Fermi and AGILE that have the best absolute timing accuracy of $\sim 2 \mu\text{s}$, it is clear from Figure 1 that the TGF is produced in the beginning of the flash as there is no signal from sferics before the TGF.

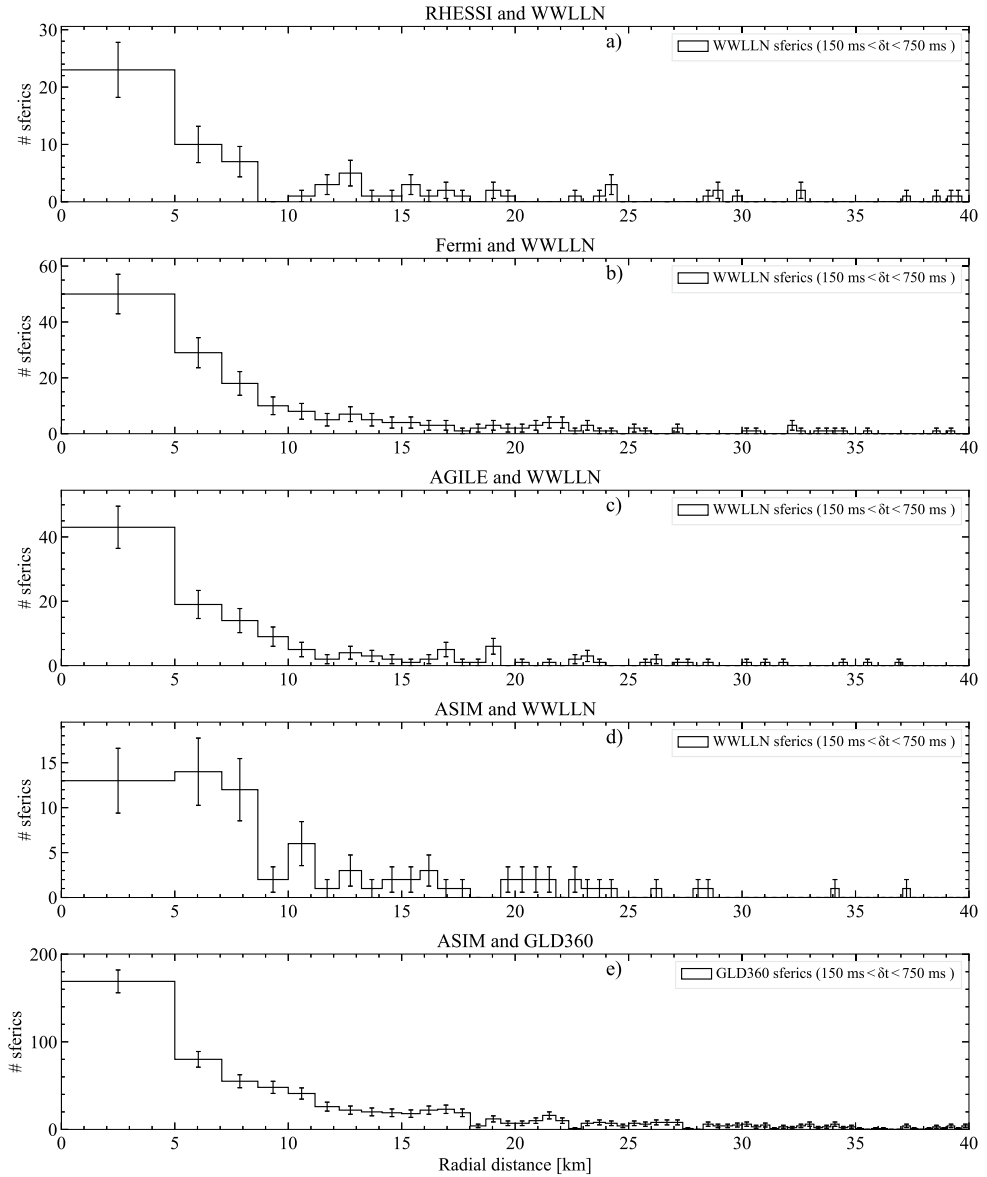


Figure 3. Stack plot showing the radial distance between the spheric matches associated to the TGFs and the sferics in the second peak. The plot shows that most activity related to the lightning flash that starts with a TGF, occur within a radial distance of 20 km. Only TGFs with a spheric match within 500 km of the subsatellite point are stacked. The bin size is chosen so that the area corresponding to each bin is constant. The uncertainty of the data points is ± 1 standard deviation assuming Poisson statistics.

The TGFs of ASIM precede the optical pulses for 57 of 58 events left in the analysis. Out of these, 42 are followed by several optical pulses. For these cases it is clear that the TGF is produced in the beginning of the lightning flash. Figure 5 shows examples of 8 of these events. For 15 of the 57 TGFs there are no additional pulses

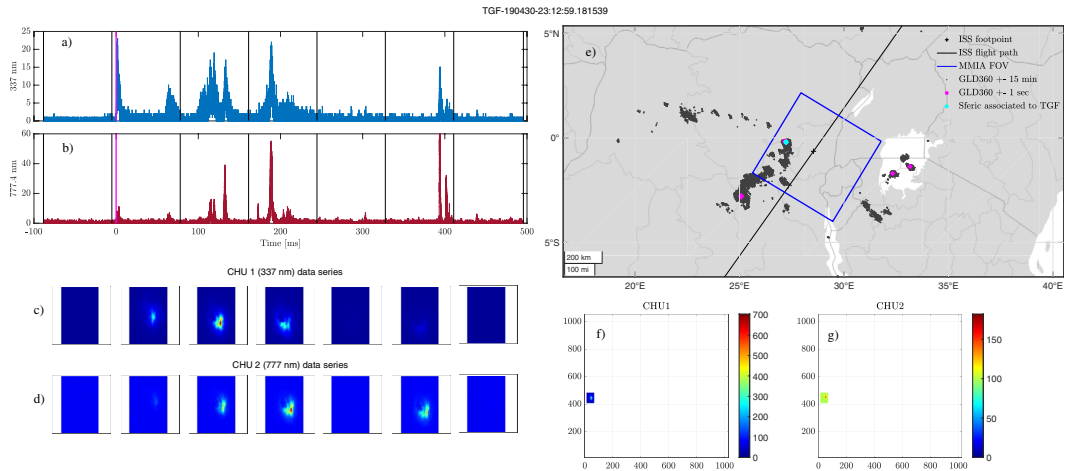


Figure 4. Overview over MMIA data at the time of a TGF that is in the beginning of a lightning flash. Panels (a and b) show the 337 and 777 nm photometer data with ADC units on the y-axis. The vertical black lines indicate the camera frames. The first peak in the 6th frame (~ 400 ms) in 777 nm peaks at ADC unit 100. The start of the TGF is indicated as a magenta vertical line at time = 0. Panels (c and d) show the corresponding CHU 1 and CHU 2 close-up camera frames. Panel (e) shows a map with MMIA FOV (blue square), ISS position and flight path, and sferics detected by GLD360. The velocity direction of ISS is to the right. Panels (f and g) show the CHU1 and CHU 2 camera frames at the time of the TGF. The full plot is the MMIA FOV and the velocity direction of ISS is in the positive vertical axes.

following the first optical pulse after the TGF. For one event we have optical pulses tens of milliseconds before and after the TGF and its large optical pulse. The time delay between the TGF and the optical pulse is ~ 1.4 ms. However, we cannot exclude the possibility that the TGF is produced outside MMIA FOV, as there exist active lightning cells outside MMIA FOV as well. This would mean that the detected flash in the photometer data is not correlated with the TGF and it is a chance coincidence. As there is only 1 of the 58 TGFs in the sample with lightning activity before the TGF, it does not change the conclusion that the TGF is produced in the beginning of the lightning flash, especially if we consider that this event may be a timing chance coincidence given the ~ 1.4 ms delay of the optical pulse relative to the TGF, the active lightning cells outside MMIA FOV, and the rarity of these events in the sample.

Based on the two different, but complementary approaches, where one approach makes use of a large TGF data set with associated sferics, and the other approach makes use of a selected TGF data set with high resolution optical measurements, we conclude that the TGF is produced in the beginning of a lightning flash.

4.2. Increased Lightning Activity After the TGF

It is evident in Figure 1 that we have a second peak of sferics between 150 and 750 ms after the TGF for all TGF catalogs. This is much later than expected for sferics counted twice by lightning detection networks as this happens on less than 100 μ s scale, thus it must be a real physical feature of the flashes. After the first peak, at the time of the TGF, the lightning activity decreases almost to background level before it increases again to a local maximum around 400 ms, before it decreases again to the background level. We see that the second peak is significant above 3σ for both black and blue histograms for all space missions. This second peak was first presented by Omar et al. (2014) and discussed in Smith et al. (2016) where it is speculated that the second peak involves cases associated to a subsequent process in the IC flash where horizontal breakdowns occur coupling new charge regions into the already established channel, so-called K-changes. To enhance the signal-to-noise ratio of the second peak, the blue histograms in Figure 1 consist of only TGFs with a sferic match according to Table 1, keeping only sferics within 20 km from the sferic match. Because we require a TGF-sferic match for the blue histogram, the second peak is smaller because we remove TGFs without a sferic match that may have sferics in the second peak. We must remember that a large fraction of TGFs does not have a detectable sferic match (Connaughton et al., 2010, 2013; Lindanger et al., 2020). We can see from Figure 1 that this selection

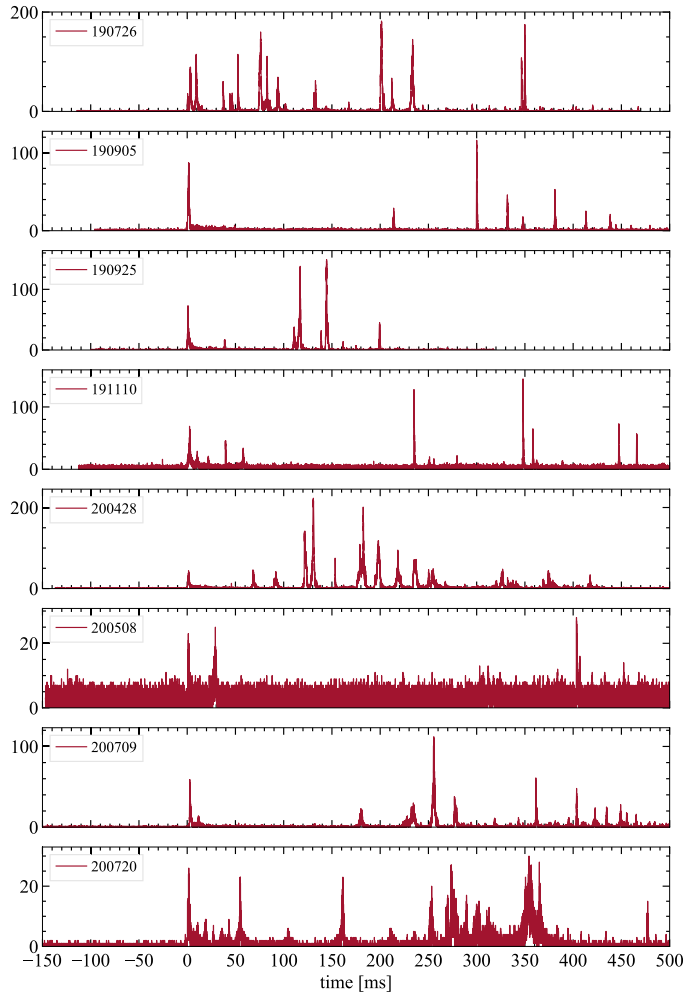


Figure 5. Optical data from the 777 nm photometer for 8 TGFs with lightning activity following the TGF. The TGF time is at time = 0, and the y-axis is in ADC units.

strategy removes almost all the background therefore enhancing the signal-to-noise ratio of the second peak. This is because most of the sferics producing the second peak are not located farther than 20 km from the sferic match. At a resolution of less than 20 km we approach the global location accuracy of WWLLN and GLD360, and from Figure 3 we can see that the 20 km radial distance from the TGF-sferic match is a conservative upper limit. Thus, we conclude that the second peak is co-located with the first peak within the localization uncertainties of the lightning detection networks meaning that the lightning discharges producing the second peak are co-located with the production location of the TGF. Note that Figure 5 shows a wide variability of the lightning activity, as observed in the optical bands, following the TGF, and that a second peak can only be seen on a larger sample of TGFs as shown in Figure 1.

To investigate if all TGFs with a sferic match (blue histograms in Figure 1) also have a sferic contributing to the second peak, we calculate the fraction of TGFs that also has one or more sferics in the second peak, between 150

Table 2
Overview Over the Fraction of TGFs With a Sferic Match That Also Have Sferic Detections in the Second Peak

Instrument-network	# TGFs with a sferic match and activity in 2nd peak	Fraction relative to 1st peak
RHESSI-WWLLN	44	0.10
Fermi-WWLLN	118	0.12
AGILE-WWLLN	83	0.13
ASIM-WWLLN	41	0.18
ASIM-GLD360	243	0.51

Note. The fraction is calculated by dividing the second column by the last column in Table 1.

and 750 ms. The results are shown in Table 2 and reveal that on average 13% of the TGFs with a WWLLN-sferic match also have sferic activity in the second peak. The fraction of TGFs with activity in second peak increases from RHESSI to ASIM. This can be explained by the improvement of the detection efficiency of WWLLN over time as the instruments are sorted from the oldest to newest time span of TGF detections. It is interesting to note that comparing ASIM-WWLLN with ASIM-GLD360, 18% of the TGFs with WWLLN-sferic matches have WWLLN detected sferics in the second peak, while 51% of the TGFs with GLD360-sferic matches have GLD360-detected sferics in the second peak. This can be explained by the difference in detection efficiency and sensitivity for the lightning detection networks. The median absolute peak current value, provided for GLD360 detections, for the first peak is 30 kA, and the median value for the second peak is 12 kA. As the strokes in the second peak in general have smaller peak currents than the first peak, the strokes in the second peak are harder to detect by lightning detection networks. This means that the detection of strokes in the second peak is strongly dependent on the sensitivity of the detection network, that is, in the threshold peak current. This is a further confirmation that when TGFs are compared to lightning data provided by lightning detection networks, the results are heavily affected by the networks' detection efficiency and sensitivity.

Mailyan et al. (2020) report a median peak current of 82 kA for sferics simultaneous with the TGFs within $\pm 200 \mu\text{s}$, and a median peak current of 26 kA for sferics associated with the TGFs from 200 μs to 3.5 ms, before and after the TGF. The median value of 30 kA in the first peak in Figure 1i consists of sferics ± 25 ms relative to the TGF, therefore including non-simultaneous sferics, biasing the median value toward lower values. Due to the timing uncertainty of ASIM, this study cannot reproduce the median peak current values from Mailyan et al. (2020).

To check if the second peak is unique for TGF production, or just a common feature of lightning flashes, we did a blind search in the GLD360 data for the first stroke in a lightning flash. The blind search data were downloaded independent of ASIM TGF triggers. We defined the first stroke in a flash as the first sferic that had no other detected sferics up to 2 s before within a radial distance of 800 km. This is done for randomly selected GLD360 data between $\pm 23^\circ$ latitude identifying 167 300 flashes with a total of 515 399 detected strokes/sferics. We did the same stacking analysis as we did for TGFs, stacking all sferics superposed at the time of the first lightning stroke. The results are shown in Figure 6 where we plot the sferics within 20 km following the first stroke, not including the first stroke itself, with the same time bin of 50 ms as used for Figure 1. The 20 km limit is applied to enhance a possible second peak between 150 and 750 ms as evidenced in the analysis of the TGF sample. The four panels have different thresholds on peak currents for the first stroke. The same analysis was also performed, with similar results as GLD360, for WWLLN data without any selection on polarity and peak current, because these variables are not available for WWLLN data. If the second peak is a general characteristic of +IC flashes, selection based on polarity and peak current of the flash as reported by GLD360 are not adequate enough to identify the second peak univocally in this sample.

As we could not identify a general second peak in the lightning data it seems that the second peak is not evident for flashes in general, thus suggesting that the second peak is a characteristic feature of a significant fraction of flashes that start with a TGF. Contrary to the blind search lightning flash sample (Figure 6), the TGF flashes (Figure 1) show a sharp decay after the first stroke which is not evident in the blind search sample. This suggests that those strokes with a TGF represent a large discharge and that it takes more than 150 ms before the electric activity is reactivated.

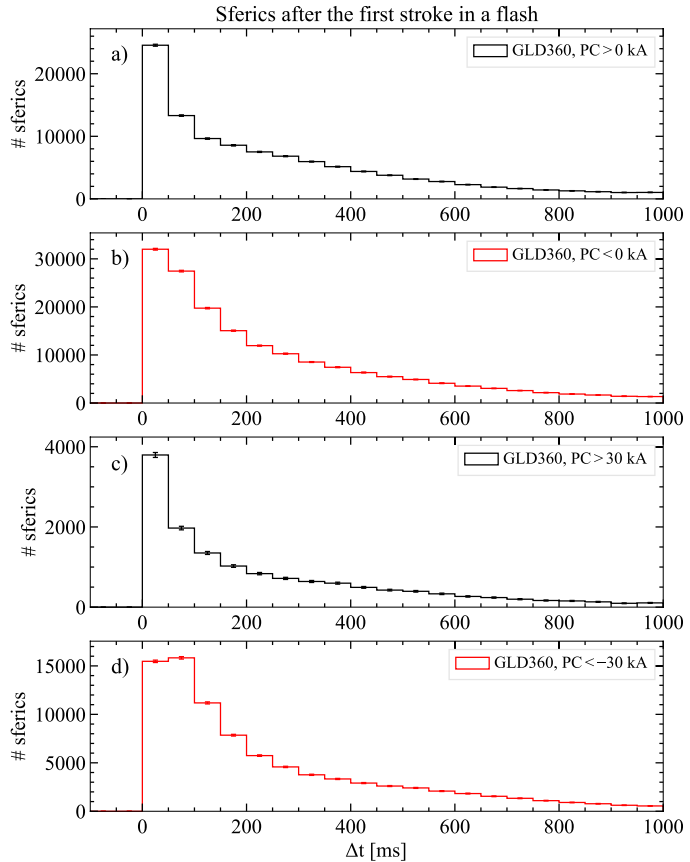


Figure 6. Histograms showing sferics within 20 km of the first stroke in a lightning flash. The first stroke is defined as the first sferic within a radius of 800 km with no detected sferics up to 2 s before. The first stroke itself is not included in the plot. The bin size is 50 ms. Each panel has a criterion, shown in the legend, on the peak current of the first stroke in the flash. The uncertainty of the data points is ± 1 standard deviation assuming Poisson statistics.

5. Summary

The TGF catalogs of RHESSI, Fermi, AGILE, and ASIM, a total of over 5,000 TGFs with sferic data ± 4 s within 500 km from the subsatellite point, are used to investigate the correlation between TGFs and sferics. The temporally closest sferic to the TGF has been studied in detail before (Albrechtsen et al., 2019; Connaughton et al., 2010, 2013; Lindanger et al., 2020; Marisaldi et al., 2015; Mezentsev et al., 2016; Østgaard et al., 2015), but the focus in these previous works was to find the *temporally closest* sferic associated to the TGF. In this study we have taken into account *all* sferics temporally close to the TGF. The study supports the idea that the TGFs are produced in the beginning of the lightning flash.

The conclusion is also supported by data from the ASIM instrumental suite, that provide a detailed high resolution data set combining TGF gamma-ray detection and optical lightning measurements. 98% (57 events out of 58) of the TGFs, where we only have optical data from the TGF location, show no lightning activity before the TGF. In the 98% sample, 26% have only one measured optical pulse and 74% have several optical pulses following the TGF. For one event of the 58 TGF events there is flash activity prior to the TGF. However, we cannot rule out that this event is a time coincidence and that the TGF is not associated with the optical signal.

There is an excess of sferics detected 150–750 ms after the TGFs in agreement with Omar et al. (2014); Smith et al. (2016). We term this excess of sferics the second peak. This study shows that in general the second peak is co-located with the first peak within <20 km, meaning that the discharges producing the second peak are co-located with the production location of the TGFs within the spatial uncertainties of the lightning detection networks. For TGFs associated with WWLLN, on average 13% of the TGFs with a WWLLN-sferic match have sferics in the second peak. For GLD360 and ASIM TGFs this fraction grows to 51%, showing that the presence or not of sferics in the second peak is strongly dependent on the sensitivity of the lightning network. A blind search in the lightning data, investigating if the second peak is a general property of lightning flashes, shows no evidence of a second peak for various selections on peak current. This suggests that the second peak is a characteristic feature for some lightning flashes that start with a TGF.

Data Availability Statement

WWLLN and VAISALA data are available upon subscription. ASIM is a mission of the European Space Agency (ESA) and is funded by ESA and by national grants of Denmark, Norway and Spain. ASIM data used for this study are available from the authors upon reasonable request or can be downloaded from the ASIM Science Data Center (<https://asdc.space.dtu.dk>). The RHESSI, Fermi, and AGILE TGF catalogs are available from the following links: <https://scipp.pbsci.ucsc.edu/rhessi/>, <https://fermi.gsfc.nasa.gov/ssc/data/access/gbm/tgf/>, and <https://www.ssdsc.asi.it/mcal3tgifcat/>. Additional data for this paper are available at <https://doi.org/10.5281/zenodo.5493848>.

Acknowledgments

This study was supported by the Research Council of Norway under contract 223252/F50 (CoE). The authors thank the International Space Science Institute, Bern, Switzerland, for providing financial support and meeting facilities in the frame of the International Team no. 471: Understanding the Properties of the Terrestrial Gamma-Ray Flash Population. The authors also wish to thank the World Wide Lightning Location Network (<http://wwlln.net>), a collaboration among over 50 universities and institutions, for providing the lightning location data used in this paper. The authors also wish to thank VAISALA for the GLD360 lightning data.

References

- Abarca, S. F., Corbosiero, K. L., & Galarneau, Jr., T. J. (2010). An evaluation of the Worldwide Lightning Location Network (WWLLN) using the National Lightning Detection Network (NLDN) as ground truth. *Journal of Geophysical Research*, *115*(D18). <https://doi.org/10.1029/2009JD013411>
- Albrechtsen, K. H., Østgaard, N., Berge, N., & Gjesteland, T. (2019). Observationally weak TGFs in the RHESSI data. *Journal of Geophysical Research: Atmospheres*, *124*(1), 287–298. <https://doi.org/10.1029/2018JD029272>
- Bogomolov, V. V., Panasyuk, M. I., Svertilov, S. I., Bogomolov, A. V., Garipov, G. K., Iyudin, A. F., et al. (2017). Observation of terrestrial gamma-ray flashes in the RELEC space experiment on the Vernov satellite. *Cosmic Research*, *55*(3), 159–168. <https://doi.org/10.1134/S0010952517030017>
- Briggs, M. S., Xiong, S., Connaughton, V., Tierney, D., Fitzpatrick, G., Foley, S., et al. (2013). Terrestrial gamma-ray flashes in the Fermi era: Improved observations and analysis methods. *Journal of Geophysical Research: Space Physics*, *118*(6), 3805–3830. <https://doi.org/10.1002/jgra.50205>
- Bürgesser, R. E. (2017). Assessment of the world wide lightning location network (WWLLN) detection efficiency by comparison to the Lightning Imaging Sensor (LIS). *Quarterly Journal of the Royal Meteorological Society*, *143*(708), 2809–2817. <https://doi.org/10.1002/qj.3129>
- Chanrion, O., Neubert, T., Lundgaard Rasmussen, I., Stoltze, C., Tcherniak, D., Jessen, N. C., et al. (2019). The Modular Multispectral Imaging Array (MMIA) of the ASIM payload on the International Space Station. *Space Science Reviews*, *215*(4), 28. <https://doi.org/10.1007/s11214-019-0593-y>
- Collier, A. B., Gjesteland, T., & Østgaard, N. (2011). Assessing the power law distribution of TGFs. *Journal of Geophysical Research*, *116*(A10). <https://doi.org/10.1029/2011JA016612>
- Connaughton, V., Briggs, M. S., Holzworth, R. H., Hutchins, M. L., Fishman, G. J., Wilson-Hodge, C. A., et al. (2010). Associations between Fermi gamma-ray burst Monitor terrestrial gamma ray flashes and sferics from the world wide lightning location network. *Journal of Geophysical Research*, *115*(A12). <https://doi.org/10.1029/2010JA015681>
- Connaughton, V., Briggs, M. S., Xiong, S., Dwyer, J. R., Hutchins, M. L., Grove, J. E., et al. (2013). Radio signals from electron beams in terrestrial gamma ray flashes. *Journal of Geophysical Research: Space Physics*, *118*(5), 2313–2320. <https://doi.org/10.1029/2012JA018288>
- Cummer, S. A., Lu, G., Briggs, M. S., Connaughton, V., Xiong, S., Fishman, G. J., & Dwyer, J. R. (2011). The lightning-TGF relationship on microsecond timescales. *Geophysical Research Letters*, *38*(14). <https://doi.org/10.1029/2011GL048099>
- Cummer, S. A., Lyu, F., Briggs, M. S., Fitzpatrick, G., Roberts, O. J., & Dwyer, J. R. (2015). Lightning leader altitude progression in terrestrial gamma-ray flashes. *Geophysical Research Letters*, *42*(18), 7792–7798. <https://doi.org/10.1002/2015GL065228>
- Cummer, S. A., Zhai, Y., Hu, W., Smith, D. M., Lopez, L. I., & Stanley, M. A. (2005). Measurements and implications of the relationship between lightning and terrestrial gamma ray flashes. *Geophysical Research Letters*, *32*(8). <https://doi.org/10.1029/2005GL022778>
- Dwyer, J. R. (2003). A fundamental limit on electric fields in air. *Geophysical Research Letters*, *30*(20). <https://doi.org/10.1029/2003gl017781>
- Dwyer, J. R., & Cummer, S. A. (2013). Radio emissions from terrestrial gamma-ray flashes. *Journal of Geophysical Research: Space Physics*, *118*(6), 3769–3790. <https://doi.org/10.1002/jgra.50188>
- Dwyer, J. R., & Smith, D. M. (2005). A comparison between Monte Carlo simulations of runaway breakdown and terrestrial gamma-ray flash observations. *Geophysical Research Letters*, *32*(22). <https://doi.org/10.1029/2005GL023848>
- Fishman, G. J., Bhat, P. N., Malozzi, R., Horack, J. M., Koshut, T., Kouveliotou, C., et al. (1994). Discovery of Intense gamma-ray flashes of atmospheric Origin. *Science*, *264*(5163), 1313–1316. <https://doi.org/10.1126/science.264.5163.1313>
- Gurevich, A., Milikh, G., & Roussel-Dupre, R. (1992). Runaway electron mechanism of air breakdown and preconditioning during a thunderstorm. *Physics Letters A*, *165*(5), 463–468. [https://doi.org/10.1016/0375-9601\(92\)90348-p](https://doi.org/10.1016/0375-9601(92)90348-p)
- Heumesser, M., Chanrion, O., Neubert, T., Christian, H. J., Dimitriadou, K., Gordillo-Vazquez, F. J., et al. (2021). Spectral observations of optical emissions associated with terrestrial gamma-ray flashes. *Geophysical Research Letters*, *48*(4), 2020GL090700. <https://doi.org/10.1029/2020GL090700>
- Hutchins, M. L., Holzworth, R. H., Brundell, J. B., & Rodger, C. J. (2012). Relative detection efficiency of the world wide lightning location network. *Radio Science*, *47*(6), RS6005. <https://doi.org/10.1029/2012rs005049>

- Lindanger, A., Marisaldi, M., Maiorana, C., Sarria, D., Albrechtsen, K., Østgaard, N., et al. (2020). The 3rd AGILE terrestrial gamma ray flash catalog. Part I: Association to lightning sferics. *Journal of Geophysical Research: Atmospheres*, *125*(11). <https://doi.org/10.1029/2019JD031985>
- Lindanger, A., Marisaldi, M., Sarria, D., Østgaard, N., Lehtinen, N., Skeie, C. A., et al. (2021). Spectral analysis of individual terrestrial gamma-ray flashes detected by ASIM. *Journal of Geophysical Research: Atmospheres*, *126*(23), e2021JD035347. <https://doi.org/10.1029/2021JD035347>
- Lu, G., Blakeslee, R. J., Li, J., Smith, D. M., Shao, X.-M., McCaul, E. W., et al. (2010). Lightning mapping observation of a terrestrial gamma-ray flash. *Geophysical Research Letters*, *37*(11). <https://doi.org/10.1029/2010GL043494>
- Mailyan, B. G., Briggs, M. S., Cramer, E. S., Fitzpatrick, G., Roberts, O. J., Stanbro, M., & Dwyer, J. R. (2016). The spectroscopy of individual terrestrial gamma-ray flashes: Constraining the source properties. *Journal of Geophysical Research: Space Physics*, *121*, 11–346. <https://doi.org/10.1002/2016ja022702>
- Mailyan, B. G., Nag, A., Dwyer, J. R., Said, R. K., Briggs, M. S., Roberts, O. J., et al. (2020). Gamma-ray and radio-frequency Radiation from thunderstorms observed from space and ground. *Scientific Reports*, *10*(1), 7286. <https://doi.org/10.1038/s41598-020-63437-2>
- Maiorana, C., Marisaldi, M., Füllekrug, M., Soula, S., Lapierre, J., Mezentsev, A., et al. (2021). Observation of terrestrial gamma-ray flashes at mid latitude. *Journal of Geophysical Research: Atmospheres*, *126*(18). <https://doi.org/10.1029/2020JD034432>
- Maiorana, C., Marisaldi, M., Lindanger, A., Østgaard, N., Ursi, A., Sarria, D., et al. (2020). The 3rd AGILE terrestrial gamma-ray flashes catalog. Part II: Optimized selection criteria and characteristics of the new sample. *Journal of Geophysical Research: Atmospheres*, *125*(11). <https://doi.org/10.1029/2019JD031986>
- Marisaldi, M., Argan, A., Ursi, A., Gjesteland, T., Fuschino, F., Labanti, C., et al. (2015). Enhanced detection of terrestrial gamma-ray flashes by AGILE. *Geophysical Research Letters*, *42*(21), 9481–9487. <https://doi.org/10.1002/2015GL066100>
- Marisaldi, M., Fuschino, F., Labanti, C., Galli, M., Longo, F., Del Monte, E., et al. (2010). Detection of terrestrial gamma ray flashes up to 40 MeV by the AGILE satellite. *Journal of Geophysical Research*, *115*(A3). <https://doi.org/10.1029/2009JA014502>
- Marisaldi, M., Galli, M., Labanti, C., Østgaard, N., Sarria, D., Cummer, S. A., et al. (2019). On the high-energy spectral Component and fine time Structure of terrestrial gamma ray flashes. *Journal of Geophysical Research: Atmospheres*, *124*(14), 7484–7497. <https://doi.org/10.1029/2019JD030554>
- Mezentsev, A., Østgaard, N., Gjesteland, T., Albrechtsen, K., Lehtinen, N., Marisaldi, M., et al. (2016). Radio emissions from double RHESSI TGFs. *Journal of Geophysical Research: Atmospheres*, *121*(13), 8006–8022. <https://doi.org/10.1002/2016JD025111>
- Neubert, T., Østgaard, N., Reglero, V., Blanc, E., Chanrion, O., Oxborrow, C. A., et al. (2019). The ASIM mission on the International space station. *Space Science Reviews*, *215*(2), 26. <https://doi.org/10.1007/s11214-019-0592-z>
- Neubert, T., Østgaard, N., Reglero, V., Chanrion, O., Heumesser, M., Dimitriadou, K., et al. (2020). A terrestrial gamma-ray flash and ionospheric ultraviolet emissions powered by lightning. *Science*, *367*(6474), 183–186. <https://doi.org/10.1126/science.aax3872>
- Omar, K. S., Briggs, M. S., & Heckman, S. (2014). *Characterizing the TGF-lightning relationship using ENTLN*. AGU Fall Meeting.
- Østgaard, N., Albrechtsen, K. H., Gjesteland, T., & Collier, A. (2015). A new population of terrestrial gamma-ray flashes in the RHESSI data. *Geophysical Research Letters*, *42*(24), 10–937. <https://doi.org/10.1002/2015GL067064>
- Østgaard, N., Balling, J. E., Bjørnsen, T., Brauer, P., Budtz-Jørgensen, C., Bujwan, W., et al. (2019). The Modular X- and Gamma-Ray Sensor (MXGS) of the ASIM Payload on the International Space Station. *Space Science Reviews*, *215*, 23. <https://doi.org/10.1007/s11214-018-0573-7>
- Østgaard, N., Cummer, S. A., Mezentsev, A., Luque, A., Dwyer, J., Neubert, T., et al. (2021). Simultaneous observations of EIP, TGF, Elve, and optical lightning. *Journal of Geophysical Research: Atmospheres*, *126*(11), e2020JD033921. <https://doi.org/10.1029/2020JD033921>
- Østgaard, N., Gjesteland, T., Carlson, B. E., Collier, A. B., Cummer, S. A., Lu, G., & Christian, H. J. (2013). Simultaneous observations of optical lightning and terrestrial gamma ray flash from space. *Geophysical Research Letters*, *40*(10), 2423–2426. <https://doi.org/10.1002/grl.50466>
- Østgaard, N., Neubert, T., Reglero, V., Ullaland, K., Yang, S., Genov, G., et al. (2019). First 10 Months of TGF observations by ASIM. *Journal of Geophysical Research: Atmospheres*, *124*(24), 14024–14036. <https://doi.org/10.1029/2019JD031214>
- Roberts, O. J., Fitzpatrick, G., Stanbro, M., McBreen, S., Briggs, M. S., Holzworth, R. H., et al. (2018). The first Fermi-GBM terrestrial gamma ray flash catalog. *Journal of Geophysical Research: Space Physics*, *123*(5), 4381–4401. <https://doi.org/10.1029/2017JA024837>
- Rodger, C. J., Brundell, J. B., Holzworth, R. H., Lay, E. H., Crosby, N. B., Huang, T.-Y., & Rycroft, M. J. (2009). Growing detection efficiency of the world wide lightning location network. *AIP Conference Proceedings*, *1118*(1), 15–20. <https://doi.org/10.1063/1.3137706>
- Said, R. K., & Murphy, M. J. (2016). GLD360 Upgrade: Performance analysis and applications. In *24th International Lightning Detection Conference(IC)*.
- Shao, X.-M., Hamlin, T., & Smith, D. M. (2010). A closer examination of terrestrial gamma-ray flash-related lightning processes. *Journal of Geophysical Research*, *115*(A6). <https://doi.org/10.1029/2009JA014835>
- Smith, D. M., Buzbee, P., Kelley, N. A., Infanger, A., Holzworth, R. H., & Dwyer, J. R. (2016). The rarity of terrestrial gamma-ray flashes: 2. RHESSI stacking analysis. *Journal of Geophysical Research: Atmospheres*, *121*(19), 11–382. <https://doi.org/10.1002/2016JD025395>
- Smith, D. M., Kelley, N. A., Buzbee, P., Infanger, A., Splitt, M., Holzworth, R. H., & Dwyer, J. R. (2020). Special Classes of terrestrial gamma ray flashes from RHESSI. *Journal of Geophysical Research: Atmospheres*, *125*(20), e2020JD033043. <https://doi.org/10.1029/2020JD033043>
- Smith, D. M., Lopez, L. I., Lin, R. P., & Barrington-Leigh, C. (2005). Terrestrial gamma-ray flashes observed up to 20 MeV. *Science (New York, N.Y.)*, *307*, 1085–1088. <https://doi.org/10.1126/science.1107466>
- Stanley, M. A., Shao, X. M., Smith, D. M., Lopez, L. I., Pongratz, M. B., Harlin, J. D., et al. (2006). A link between terrestrial gamma-ray flashes and intracloud lightning discharges. *Geophysical Research Letters*, *33*(6). <https://doi.org/10.1029/2005GL025537>
- Ursi, A., Guidorzi, C., Marisaldi, M., Sarria, D., & Frontera, F. (2017). Terrestrial gamma-ray flashes in the BeppoSAX data archive. *Journal of Atmospheric and Solar-Terrestrial Physics*, *156*, 50–56. <https://doi.org/10.1016/j.jastp.2017.02.014>

Paper III

The temporal relationship between Terrestrial Gamma-ray flashes and associated optical pulses from lightning

C. A. Skeie, N. Østgaard, A. Mezentsev, I. Bjørge-Engeland, M. Marisaldi, N. Lehtinen, V. Reglero, T. Neubert

Journal of Geophysical Research: Atmospheres - in review,

1 **The temporal relationship between Terrestrial**
2 **Gamma-ray flashes and associated optical pulses from**
3 **lightning**

4 **C. A. Skeie¹, N. Østgaard¹, A. Mezentsev¹, I. Bjørge-Engeland¹, M.**
5 **Marisaldi^{1,2}, N. Lehtinen¹, V. Reglero³, T. Neubert⁴**

6 ¹Birkeland Centre for Space Science, Institute of Physics and Technology, University of Bergen, Bergen,
7 Norway

8 ²INAF-OAS Bologna, Bologna, Italy

9 ³Imaging Processing Laboratory, University of Valencia, Valencia, Spain

10 ⁴National Space Institute, Technical University of Denmark, Kongens Lyngby, Denmark

11 **Key Points:**

- 12 • TGFs are produced before or simultaneously with the onset of an optical pulse
13 • For some events the delay of the optical pulse is too long to be explained by the
14 light scattering in the cloud
15 • Longer duration TGFs tend to have longer delays between onsets of the TGFs and
16 the optical pulses

Corresponding author: C. A. Skeie, Chris.Skeie@uib.no

17 Abstract

18 We present 221 Terrestrial Gamma-ray flashes (TGFs) and associated optical pulses ob-
 19 served by the Atmosphere-Space Interactions Monitor on board the International Space
 20 Station. The events were detected between the end of March 2019 and November 2020
 21 and consist of X- and Gamma-ray energy detections, as well as photometer data (180-
 22 230 nm, 337 nm and 777 nm) and optical camera data (337 nm and 777 nm). Using the
 23 available ASIM data and applying a consistency check based on TGF characteristics and
 24 lightning detections from lightning radio atmospherics close in time, we determine the
 25 most likely position of the TGFs in relation to the photometer field of view (FoV), and
 26 the association to the observed optical pulses. Out of the 221 events we find 72 events
 27 where the TGF and optical data are determined to be associated and inside the photome-
 28 ter FoV. Using the measured TGF durations and the time between the onsets of the TGFs
 29 and optical pulses we find 1) That the TGF onsets are always before or at the same time
 30 as the optical pulse onsets (taking into account cloud scattering). 2) A tendency for longer
 31 duration TGFs to have longer delays between onsets. 3) Two groups of events, one where
 32 the TGFs last longer than the delay between onsets, and one where there are long de-
 33 lays between onsets, that can not be explained by cloud scattering.

34 1 Introduction

35 Terrestrial Gamma-ray Flashes (TGFs) are bursts of hard X- and gamma-rays pro-
 36 duced via bremsstrahlung from runaway electrons accelerated in the electric fields of thun-
 37 derstorms (Wilson, 1925; Gurevich et al., 1992; Moss et al., 2006; Dwyer, 2012). The TGFs
 38 are reported to typically last a few tens, up to a few hundred microseconds, and have
 39 individual photon energies up to ~ 40 MeV (Fishman et al., 1994; Smith et al., 2005; Marisaldi
 40 et al., 2010; Briggs et al., 2013; Marisaldi et al., 2014). Analysis of the energy spectra
 41 of TGFs and lightning radio atmospherics indicate that they are produced below 21 km
 42 altitude, most likely between 10 and 15 km (Dwyer & Smith, 2005; Stanley et al., 2006;
 43 Carlson et al., 2007; Xu et al., 2012; Cummer et al., 2014; Mailyan et al., 2016; Pu et
 44 al., 2019; Lindanger et al., 2021). The underlying mechanism for creating the observed
 45 TGF photon fluxes is still unclear. There are two leading models for explaining the ob-
 46 served fluxes based on where and how the electrons are accelerated. Both theories build
 47 on electrons being accelerated in electric fields that are strong enough to overcome the
 48 friction force of the air, in what is called the runaway process (Wilson, 1925), before be-

49 ing multiplied in a relativistic runaway electron avalanche (RREA) process (Gurevich
50 et al., 1992). In the first model, an electron flux is created in an avalanche process de-
51 veloping in the large-scale electric fields within the thunderclouds. Back-scattered X-rays
52 created by bremsstrahlung, and positrons created by pair-production, seed additional
53 electron avalanches in what is called a relativistic feedback mechanism (Dwyer, 2008).
54 In the other model the initial electron flux is created in small, intense, transient over-
55 lapping electric fields of streamers, lightning leader and thundercloud electric field. The
56 overlapping electric fields are strong enough to let electrons runaway, and then undergo
57 bremsstrahlung and produce X- and gamma-rays (Moss et al., 2006; Celestin & Pasko,
58 2011). These two models can also be at play simultaneously, as one does not exclude the
59 other.

60 TGFs were first reported by Fishman et al. (1994), using the Burst and Transient
61 Source Experiment (BATSE) on the Compton Gamma Ray Observatory. Since then many
62 observations of TGFs have been made, using mostly satellite-based (Smith et al., 2005;
63 Briggs et al., 2010; Marisaldi et al., 2010, 2014; Østgaard, Neubert, et al., 2019), but also
64 aircraft (Smith et al., 2011; Bowers et al., 2018) and ground based instruments (Dwyer
65 et al., 2004, 2012; Hare et al., 2016; Abbasi et al., 2018; Wada et al., 2019). The Atmosphere-
66 Space Interactions Monitor (ASIM) is the first instrument specifically designed to ob-
67 serve TGFs, as well as transient luminous events. ASIM is mounted on the Columbus
68 module of the International Space Station (ISS), and has been gathering data since April
69 2018. ASIM has multiple detectors consisting of high and low energy X- and gamma-
70 ray detectors, photometers and optical cameras (Neubert et al., 2019).

71 Past studies using radio data have shown that TGFs likely occur during the early
72 phase of intracloud lightning (Lu et al., 2010; Shao et al., 2010; Østgaard et al., 2013,
73 2021; Pu et al., 2019). This is also shown in Lindanger et al. (2022) who used TGF de-
74 tections paired with optical measurements of lightning activity to show that TGFs are
75 produced during the initial phase of a lightning flash. The sequence of the TGF and op-
76 tical signal of the flash is still uncertain. Østgaard et al. (2013) were the first to report
77 simultaneous observation of a TGF and optical light from lightning. Using a TGF de-
78 tected by the Ramaty High Energy Solar Spectroscopic Imager (RHESSI) and optical
79 data from the Lightning Imaging Sensor (LIS) on board the Tropical Rainfall Measur-
80 ing Mission (TRMM) satellite, they conclude that the TGF was produced in the initial
81 stage of an intracloud (IC) lightning propagating upwards in the cloud. Gjesteland, Østgaard,

82 Bitzer, and Christian (2017) re-investigated the TGF-optical sequence using two TGFs
83 detected by RHESSI and optical data from LIS, as well as lightning radio atmospher-
84 ics from the World Wide Lightning Location Network (WWLLN). However, due to the
85 uncertainties of the instruments (± 1.6 ms) they could not determine the sequence of TGF
86 and optical signal of the flash. More recent observations from ASIM have shown that
87 the majority of TGFs occur before or at the onset of the optical emissions, given the un-
88 certainties in the measurements (Neubert et al., 2020; Østgaard, Neubert, et al., 2019;
89 Heumesser et al., 2021). A relevant aspect in the determination of the sequence of the
90 TGF and optical emissions is the cloud scattering of the optical signals. Satellite detec-
91 tion of optical light from lightning including cloud effects such as scattering, has recently
92 been modelled (Luque et al., 2020; Peterson, 2020). The optical light emitted from light-
93 ning in different wavelength bands is associated with different processes in a lightning
94 flash, such as the hot channel of a lightning discharge, or streamer activity before the
95 discharge (Chanrion et al., 2019).

96 In this work we will investigate the temporal relationship between TGFs and op-
97 tical emissions from lightning. For this purpose we will use a set of TGFs with accom-
98 panying optical detections observed by ASIM. We start by investigating the sequence
99 of TGF and the main optical pulse (defined in section 3.6), which has been addressed
100 using ASIM before in Østgaard, Neubert, et al. (2019) and Heumesser et al. (2021). The
101 results of Østgaard, Neubert, et al. (2019) were hampered by the relative timing accu-
102 racy (± 80 μ s) between the MXGS and MMIA instruments. In this paper we will use a
103 larger data sample from a later period, where the relative accuracy between the instru-
104 ments have been improved to ± 5 μ s, and more sophisticated and accurate methodology.
105 Heumesser et al. (2021) also analysed TGFs and optical data observed by ASIM, and
106 concluded that the sequence of TGF-optical can not be addressed due to the uncertain-
107 ties in timing and the model they used. For this work we have carefully inspected each
108 event and applied a consistency check (outlined in Section 3), where we determine the
109 relationship of each detected TGF and optical pulse. For this purpose we inspected the
110 geolocation source of the radio atmospherics from the lightning discharges, together with
111 the optical detections of lightning and TGF characteristics to determine which of the ob-
112 served optical pulses are most likely associated with the TGFs. The events where the
113 TGF and optical pulse are found to be associated will then be used to investigate the
114 sequence of the TGF and optical pulse, as well as the relationship between TGF dura-

115 tions and the time delay between TGF and the onset of the optical pulse, to help un-
 116 derstanding the processes involved and sequence of events.

117 2 Instruments and Data

118 The ASIM payload (Neubert et al., 2019) on board the ISS consists of two main
 119 instruments: the Modular Multi-spectral Imaging Array (MMIA) and the Modular X-
 120 and Gamma-ray Sensor (MXGS). The MMIA (Chanrion et al., 2019) consists of three
 121 photometers and two cameras, which are tilted 5 degrees upwards from nadir (toward
 122 starboard of ISS) to avoid potential obstructions from payloads on the bottom of the mount-
 123 ing platform. The photometers operate in 180-230 nm (UV), 337 nm (blue) with a 4 nm
 124 bandwidth, 777.4 nm (red) with a 5 nm bandwidth bands and have a sample rate of 100
 125 kHz. The two optical cameras capture up to 12 frames per second, operate in the 337
 126 and 777 nm bands, and have a 400 x 400 m resolution at nadir. Both the 337 nm and
 127 777 nm photometers and cameras have a square field of view (FoV) (80° diagonal), while
 128 the UV photometer have a circular FoV (80° diameter). As we are only using the 777
 129 nm and 337 nm band in this study we will refer to the square FoV as MMIA FoV through-
 130 out this paper. To prevent damage by sunlight, the MMIA instrument is only active dur-
 131 ing night time. The MXGS (Østgaard, Balling, et al., 2019) consists of a high and low
 132 energy detector. The high-energy detector (HED) is always active while outside the South
 133 Atlantic Anomaly, detects energies between 300 keV to 30 MeV, and has a time reso-
 134 lution of 28.7 ns. The low energy detector (LED) is only active during night, due to op-
 135 tical photon contamination during day time, detects energies between ~ 50 to 400 keV,
 136 and has a resolution of 1 μ s. The ASIM instrument includes a cross triggering system
 137 between MXGS and MMIA, such that if either instrument triggers data from both will
 138 be kept for a period of ~ 2 seconds, centred on the trigger time. The relative timing ac-
 139 curacy between the MXGS and MMIA instrument was ± 80 μ s until a software update
 140 in April 2019, which reduced it to ± 5 μ s. Due to a non-optimal timing interface between
 141 the ISS and the ASIM instrument, the absolute timing accuracy is found to be ~ -10
 142 to $+40$ ms (determined using lightning detection location from lightning radio atmospher-
 143 ics). This timing accuracy can be improved for some events by using lightning detections
 144 together with optical data, to reduce the absolute timing accuracy to ± 1 ms.

145 Lightning Radio atmospheric used in this work is provided by Vaisala's Global Light-
 146 ning Detection Network (GLD360), and give us mainly time and location data of light-

147 ning flashes. GLD360 is a ground-based very-low-frequency (VLF) and lower part of low-
 148 frequency (LF) radio lightning detection network which employs Time of Arrival and Mag-
 149 netic Direction Finding at each sensor, to determine the location of individual lightning
 150 discharges. The expected GLD360 detection efficiency is $\sim 75\text{-}85\%$ for cloud-to-ground
 151 flashes, $\sim 40\text{-}50\%$ for intracloud pulses (IC), with a $\sim 2\text{-}6$ km uncertainty in median lo-
 152 cation accuracy (Demetriades et al., 2010; Said & Murphy, 2016).

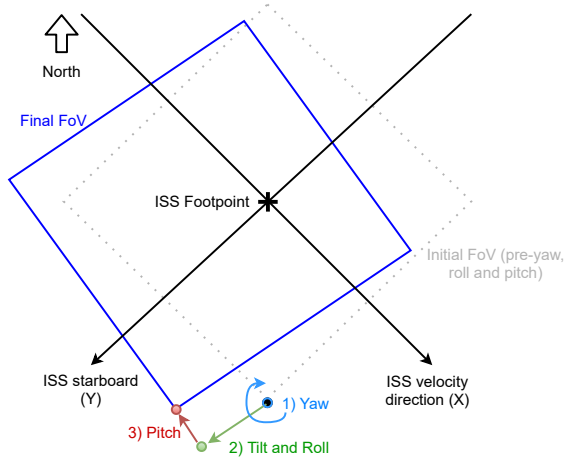
153 **3 Methodology**

154 Between end of March 2019 and November 2020 we have observed 221 TGFs, where
 155 also optical data from MMIA are available with a relative timing accuracy of ± 5 μs . To
 156 determine the association between the TGFs and the optical pulses we investigated the
 157 photometer data in three main steps. 1) We search for an optical pulse in the 337 and
 158 777 nm optical band within 5 ms of the TGF. If there is no optical pulse the TGF is most
 159 likely outside the MMIA FoV and we exclude the event. 2) For the remaining events the
 160 MMIA FoV is determined and the surrounding lightning activity within 15 minutes of
 161 the TGF is investigated to determine a possible location of the TGF. 3) A consistency
 162 check is performed (as outlined in section 3.3) using the surrounding lightning activity,
 163 camera images (83.3 ms resolution) and TGF characteristics, such as number of counts
 164 and their energies.

165 **3.1 MMIA Field of View**

166 To determine the square MMIA photometer FoV we first interpolate the ISS foot-
 167 point at the time of the TGF, using the closest ISS locations before and after the TGF,
 168 as well as the ISS velocity and the difference in time between the TGF detection and the
 169 two points. From the ISS foot-point we map out the 337 and 777 nm photometer FoV,
 170 which is a square with 80° diagonal for both photometers (Chanrion et al., 2019), with
 171 the sides going along and across the ISS direction of travel (X and Y in Figure 1). This
 172 is done by using 8 points, namely the 4 corners of the square and points at the middle
 173 of each side. These 8 points are then shifted using yaw, roll and pitch angles of the ISS
 174 at the time of the TGF, as well as the 5 degree tilt in the roll direction, as illustrated
 175 in Figure 1. The photometer FoV was compared with coastline camera images, acquired
 176 specifically to optimise the pointing accuracy. The difference in the determined FoV and

177 coastal camera images were found to be at most ~ 20 km, which is acceptable for the pur-
 178 poses of this study.



179 **Figure 1.** Illustration of how to determine the corner-point of the MMIA FoV projected from
 180 the ISS to ground level on Earth in 3 steps. 1) Rotation due to ISS yaw angle ($\pm Z$ -direction), 2)
 181 move according to roll angle and the 5 degree tilt of the MMIA instrument in the roll direction
 182 ($\pm Y$ -direction). 3) move according to the pitch angle ($\pm X$ -direction)

183 3.2 Lightning detections

184 Using the location data from lightning radio atmospheric (detected by GLD360)
 185 in the surrounding area from within ± 1000 seconds we get 3 different scenarios. 1) All
 186 lightning activity is outside the MMIA FoV, meaning the TGF is most likely from out-
 187 side the FoV. 2) All lightning activity is inside the MMIA FoV, meaning the TGF is most
 188 likely from inside the FoV. 3) There is lightning activity both inside and outside the MMIA
 189 FoV. For all of these groups of events we apply the consistency check (see section 3.3),
 190 where the lightning activity is used together with 1) TGFs individual photon energies
 191 and fluence and 2) camera images.

192 The GLD360 detections are also used to improve the absolute timing accuracy of
 193 ASIM, which is found to be -10 to $+40$ ms before improvement. For many of the events
 194 we can improve the absolute timing of ASIM by time alignment of the measured opti-

cal pulses and GLD360 detections. This is done by first finding the ISS time of the GLD360
detections, by adding the lights travel time from source to the ISS, to the given GLD360
detection time. We then use multiple triggers of MMIA data (up to three, consisting of
the trigger containing the TGF and one trigger before and after the trigger containing
the TGF) to align as many optical pulse peaks as possible to the GLD360 detections.
A minimum of two alignments is required, with a minimum of one optical pulse aligned
from the MMIA trigger containing the TGF.

Aligning the GLD360 detections to the optical pulse peaks is practical, although
this approach does not take into account the time delay due to light scattering through
the clouds. However, given the typical rise times of the optical pulses, this is well within
the error of the method. The lightning detection locations and camera images are then
checked for consistency. Using this technique we can get the absolute timing accuracy
between MMIA and the GLD360 detections down to ± 1 ms. This method of improv-
ing absolute timing accuracy has already been implemented in Maiorana et al. (2021),
Lindanger et al. (2022), and independently developed and applied in Heumesser et al.
(2021). Using the method outlined here we found 95 alignments for the total sample of
events.

3.3 Consistency check

A consistency check is performed to determine if the TGFs are likely to be within
the MMIA FoV and have an association with the optical pulses. For this purpose we use
the TGF fluence and individual photon energies, and compare to optical camera and light-
ning activity. For the consistency check we consider a TGF emission half-cone of 30-40°
without tilt. The TGF fluence is expected to be reduced as the distance between the TGF
and ISS-footpoint increases. This is due to the scattering of photons in the atmosphere
and the increasing distance ($1/R^2$ effect). Furthermore, we expect TGFs observed within
the production cone to have more high energy (above energy channel 1000, which is ap-
proximately 10 MeV) counts than the TGFs from outside the production cone. For TGFs
observed outside the initial production cone the photons will have undergone Compton
scattering and have reduced energies (Carlson et al., 2007; Gjesteland et al., 2011; Lin-
danger et al., 2021). This means the TGFs with no or very few counts with high ener-
gies are more likely to be produced outside the MMIA FoV, because the half-cone an-
gle (30-40°) is similar to the MMIA FoV (diagonal angle of 40°). We also investigate the

227 lightning activity surrounding the TGF and check for a GLD360 detection associated
 228 to the TGF and optical pulse. If such a pulse is found we compare the location of the
 229 GLD360 detection to the optical camera, as well as the TGF characteristics. We do not
 230 use any of these assumptions as hard limitations, but as an indicator to differentiate TGFs
 231 inside the MMIA FoV from those outside the MMIA FoV.

232 3.4 Event examples

233 Following are examples that show events where the consistency check is used to help
 234 determine the TGF-optical pulse association.

235 Figure 2 shows an example of an event where we have determined that the TGF
 236 and optical pulse is associated. For this event enough GLD360 detections could be aligned
 237 with optical pulses so that the total timing accuracy was reduced to ± 1 ms. As seen panel
 238 e) of the figure, most lightning activity is inside the MMIA FoV, with multiple lightning
 239 detections within 1 second of the TGF clustered at the same area. The magenta stars
 240 show the GLD360 detections within one second of the TGF time, with the green star
 241 showing the GLD360 detection found to be aligned in time to the optical pulse. No other
 242 GLD360 detections were found to be within the -10 to $+40$ ms window (blue stars), cor-
 243 responding to the total timing accuracy of ASIM. The camera images (f and g) support
 244 that the optical pulses come from the same location as the GLD360 detections. Panel
 245 a) shows the counts, with energies from the HED. The TGF has a hard spectrum (5 counts
 246 above channel 1000) with many counts (97) in a short time interval (~ 100 μ s), which
 247 is consistent with a TGF within a small radial distance ~ 200 - 300 km to the ISS foot-
 248 point, ie. within the MMIA FoV. ISS is moving eastward and the camera images have
 249 Y-axis along the path and X-axis towards starboard. This all indicates that the TGF
 250 is from within the MMIA FoV, and associated to the observed optical pulse.

251 Figure 3 shows another example of an event where the TGF is determined to be
 252 within the MMIA FoV. For this event there is only lightning activity within the MMIA
 253 FoV. There were not enough GLD360 detections to improve the timing accuracy for this
 254 event. Two GLD360 detections are seen inside the MMIA FoV within the minimum and
 255 maximum of the absolute timing correction (blue stars). One of the detections is most
 256 likely an ionospheric reflection, considering the time, distance and peak currents (oppo-
 257 site but similar magnitude). This is also supported by the camera images, where only

258 one active area is seen. An ELVE (Emission of Light and Very Low Frequency pertur-
 259 bations due to Electromagnetic Pulse Sources) event is observed (UV pulse starting at
 260 0 μ s) at the same time as the TGF. Thirteen such ELVEs were found in this dataset,
 261 these events are also a part of the data set analysed and presented in Bjørge-Engeland
 262 et al. (2022).

263 A total of 72 events were found, where we could determine an association between
 264 the TGF and the optical pulse such as the events shown in Figures 2 and 3. 45 absolute
 265 timing corrections were determined for these 72 events, where 33 ended up with a GLD360
 266 detection aligned with the optical pulse associated to the TGFs.

267 Figure 4 shows an event for which we have determined that the TGF is not from
 268 within the MMIA FoV, and therefore the observed optical pulse is not associated with
 269 the TGF. The lightning activity map (e) shows there are many centres of activity out-
 270 side the MMIA FoV, but no lightning activity within 1 second of the TGF (magenta,
 271 blue or green stars). The camera images (f-g) show that the optical pulses come from
 272 a location close to the ISS foot-point. The TGF (a) is found to be long, with relatively
 273 few counts in HED (19) and only one count above energy channel 1000. The TGF char-
 274 aracteristics in this instance do not match our expectations of a TGF found inside the MMIA
 275 FoV and close to the ISS foot-point. In this case it is likely that the TGF is produced
 276 in one of the active areas outside the FoV and is not associated with the optical pulses
 277 we observe. We found 57 events of this type, where the TGF is most likely outside the
 278 FoV, and consequently not included in our study.

279 The last group of events are the 88 events excluded in the beginning where we have
 280 no association, as there is no observed optical pulse within ± 5 ms of the TGF. Figure
 281 5 shows one of these events, with no lightning activity within the MMIA FoV as further
 282 support. Some lightning activity is observed within 1 second of the TGF just outside the
 283 MMIA FoV, shown as the 3 magenta stars. The TGF has few counts, with energies be-
 284 low channel 300, which is consistent with being produced outside the MMIA FoV.

285 For four events there are difficulties in determining optical pulse onset, or TGF as-
 286 sociation to the optical pulse. This is due to there either being multiple TGFs within
 287 the 5 ms time window, but only 1 optical pulse, or difficulties identifying the pre-activity
 288 and determining the onset of the optical pulse. As we do not want to make assumption
 289 on which TGF is associated to the optical pulse, or what is pre-activity and main op-

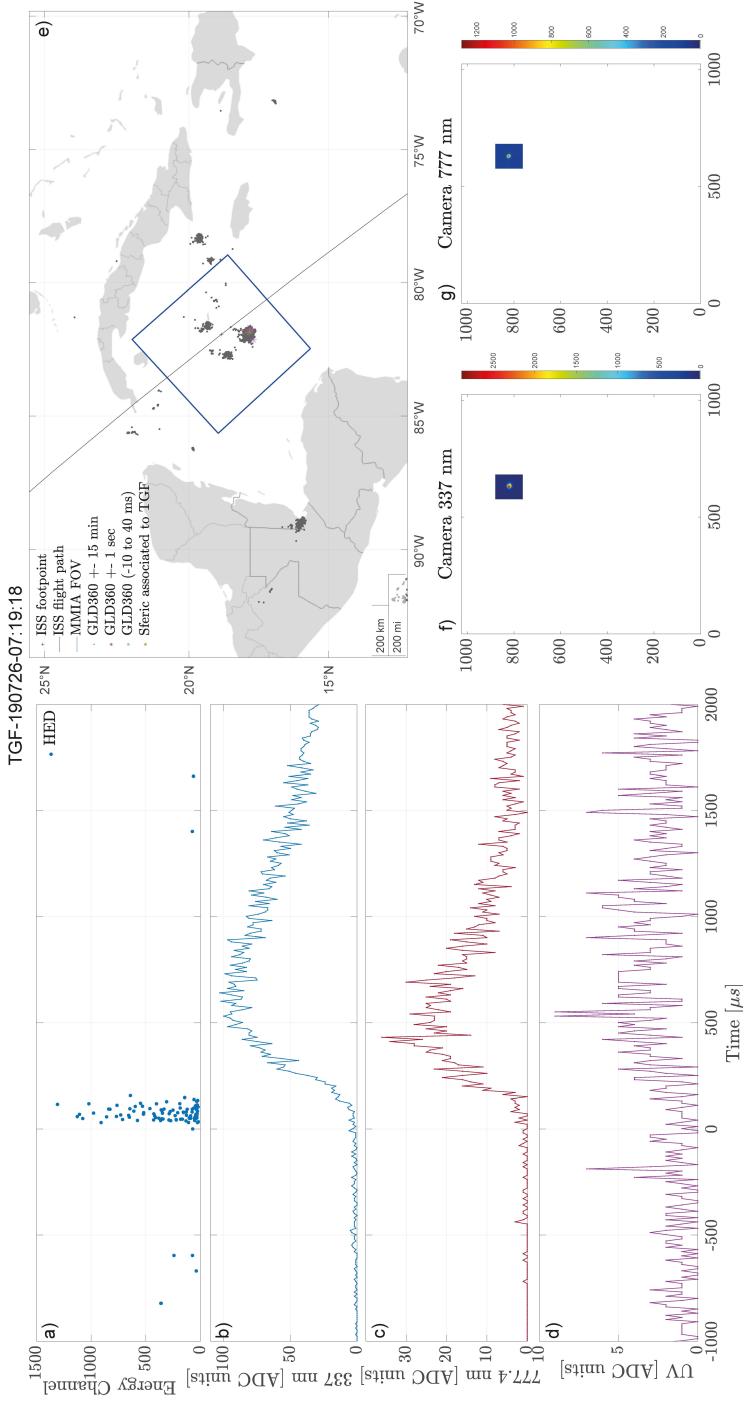


Figure 2. Example of an event where we have determined the TGF to be inside the MMIA FOV and associated to the observed optical pulse. a) Detected counts in HED. b-d) Light curves from the photometers, 337, 777 and 180-230 nm. e) Map of the area around the ISS footprint. The blue square shows the MMIA FOV, the black dots are lightning activity within ± 15 min of the TGF, the magenta stars are lightning activity within a second of the TGF, and the green star shows the lightning detection aligned to the optical pulse. f-g) Camera 337 nm and 777 nm show the optical camera images from the frame containing the TGF (Y-axis is along the flight path of the ISS, which is always eastwards/right in the images).

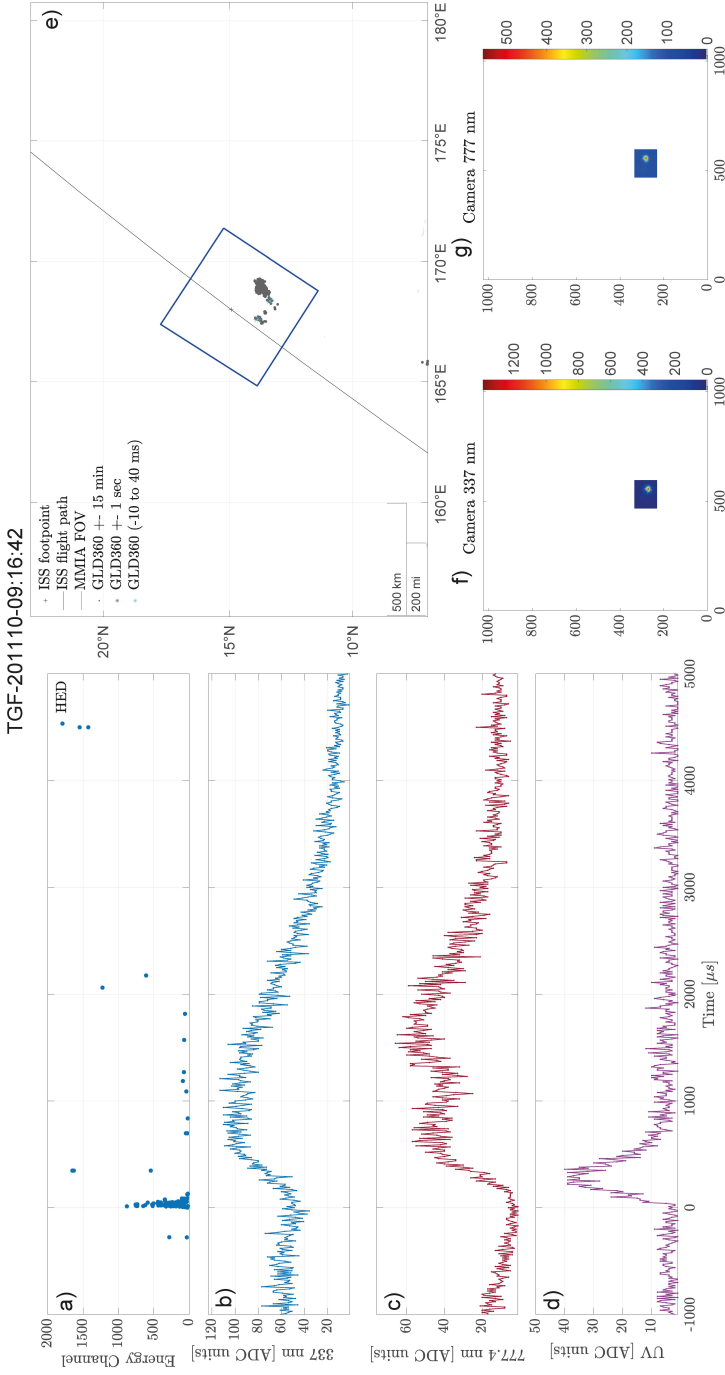


Figure 3. Example of an event where we have determined the TGF to be inside the MMIA FoV and associated to the observed optical pulse, and there is only lightning activity from within the FoV. a) Detected counts in HED. b-d) Light curves from the photometers, 337, 777 and 180-230 nm. e) Map of the area around the ISS footprint. The blue square shows the MMIA FoV, the black dots are lightning activity within ± 15 min of the TGF, the magenta stars are lightning activity within a second of the TGF, and the green star shows the lightning detection aligned to the optical pulse. f-g) Camera 337 nm and 777 nm show the optical camera images from the frame containing the TGF (Y-axis is along the flight path of the ISS, which is always eastwards/right in the images).

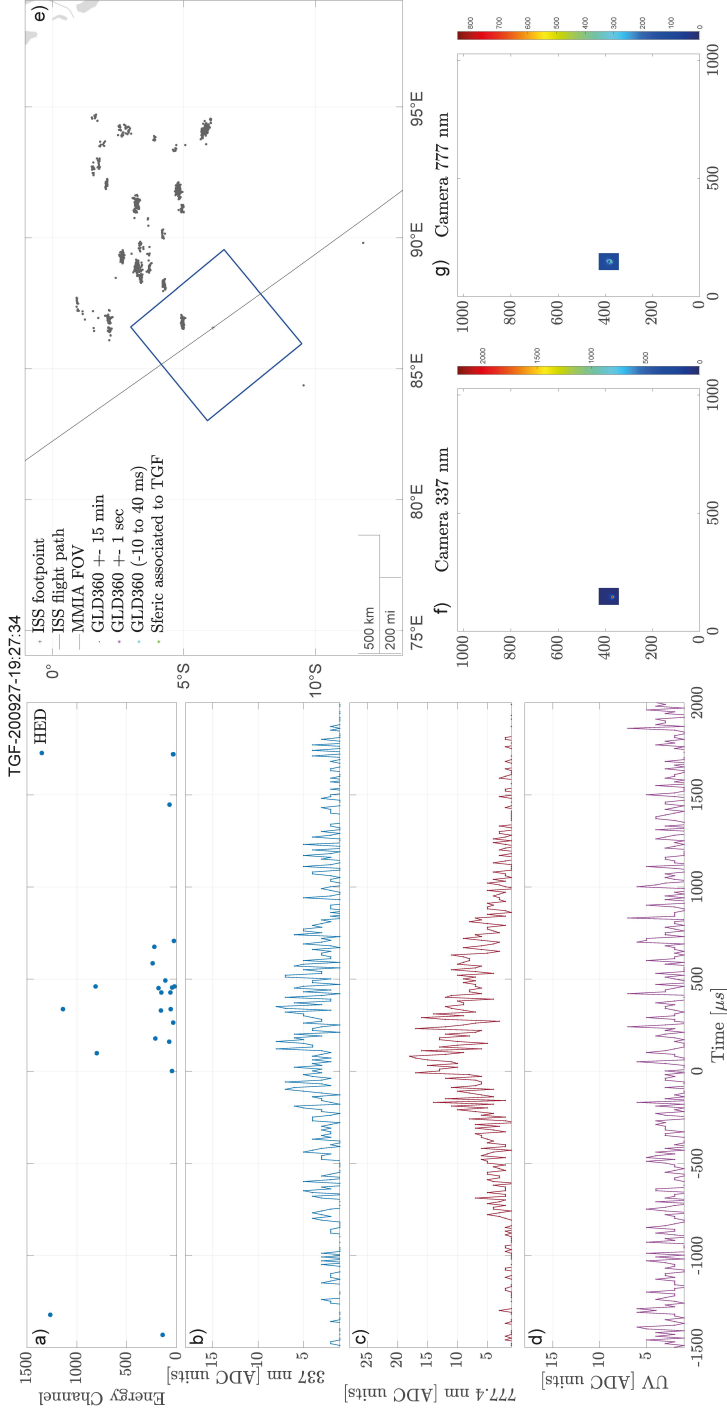


Figure 4. Example of an event where we have determined the TGF to be outside the MMIA FoV and is therefore not associated to the observed optical pulse. a) Detected counts in HED. b-d) Light curves from the photometers, 337, 777 and 180-230 nm. e) Map of the area around the ISS footprint. The blue square shows the MMIA FoV, the black dots are lightning activity within ± 15 minutes of the TGF. No lightning detections are within 1 minute of the detected TGF (magenta, blue or green stars). f-g) Camera 337 and 777 nm show the optical camera images from the frame containing the TGF (up is along the flight path of the ISS, which is always eastwards/right in the images).

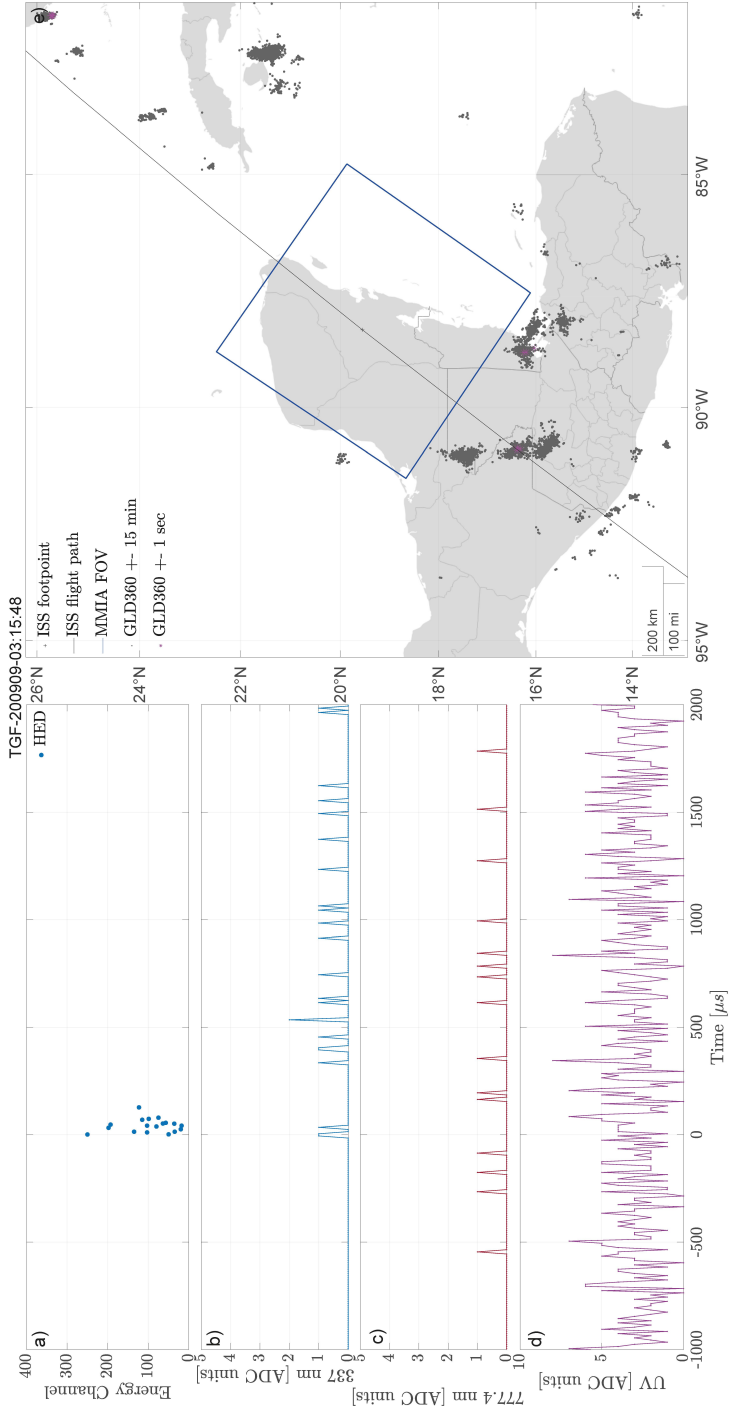


Figure 5. Example of an event where the TGF is outside MMIA FoV, and there is no optical pulse observed in the photometers. a) Detected counts in HED. b-d) Light curves from the photometers, 337, 777 and 180-230 nm. e) Map of the area around the ISS footprint. The blue square shows the MMIA FoV, the black dots are lightning activity within 15 minutes of the TGF, the magenta stars show lightning activity within a second of the TGF.

tical pulse, we decided to exclude these events going forward. Table 1 shows a summary
of the number of events in each category.

Table 1. Summary of events

Inside FoV (# time alignments)	Most likely outside FoV	No optical pulse	Non-determinable
72 (45)	57	88	4

3.5 TGF durations

The TGF durations were determined using an algorithm to find a “core duration” defined as the shortest time interval which includes 90% of the counts (t_{core90}). The algorithm works by first binning the counts around TGF time into 40 μs bins, and selecting the bin with the most counts as a starting point. Thereafter we go backwards and include any count that is within 100 μs of the previously included count. The first photon of the TGF is then found where there is more than 100 μs between the current count and the one before it. This same approach is also applied from the starting position and forwards in time, to find the end of the TGF. A sliding window is then used to find the shortest duration that contains 90% of the counts (rounded up) between the start and end counts. As this method runs the risk of including cosmic showers and solar protons we perform a manual inspection of the events for the purpose of removing these counts. To determine the uncertainties in TGF t_{core90} durations we chose to add the closest count in time before and after the determined TGF counts in the method outlined above (these counts will be more than 100 μs before/after the first/last count). We then determine the t_{core90} duration of this sample and use the difference in duration compared to the original t_{core90} as the uncertainty.

3.6 Optical pulse onsets

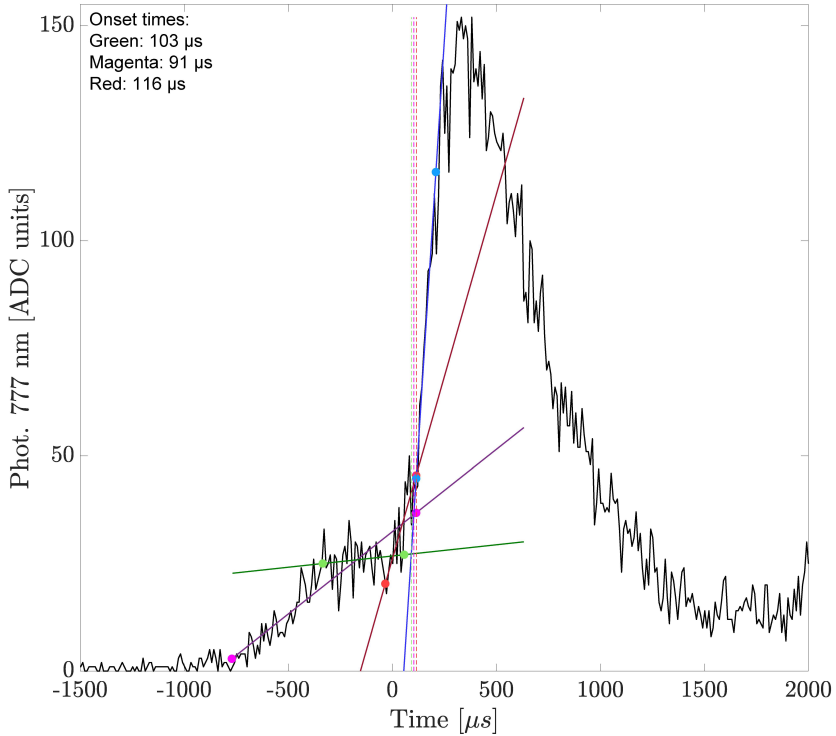
To determine the onset of the optical pulse we determined several separate linear fits to different parts of the optical pulse. We used the intersects of linear fits of the sharpest rise in the optical pulse and the activity before this rise. To make these fits we mainly used the 777 nm light curves, but for some events a good fit could not be made to the 777 nm light curves, so the 337 nm light curves were used instead. The red light (777 nm) is preferred as it is thought to be mainly associated to atomic oxygen (OI) which

317 may only exist (after dissociation of O_2) in the heated lightning leader channel (Chanrion
 318 et al., 2019), whereas the blue light (337 nm) is associated to the streamer activity, namely
 319 N_2 second positive band group radiation caused by excitation by supra-thermal electrons.
 320 The 337 band might also detect some UV emissions, such as from ELVEs.

321 For each event we separate the optical pulse activity into pre-activity and main rise
 322 (sharpest increase). One linear fit was made for the sharpest rise of the optical pulse,
 323 while we use 3 fits for the pre-activity. The pre-activity is thought to be optical emis-
 324 sions from the propagating lightning leader (Østgaard, Neubert, et al., 2019), and can
 325 be seen in Figure 6 as the relatively slow increase after $-1000 \mu s$ and until $\sim +100 \mu s$.
 326 For some cases we found it necessary to make two fits to the sharpest increase part, as
 327 the pulse was irregular with a separate increase between the sharpest increase and the
 328 pre-activity. The average of the intersects between the main rise fit lines and the mul-
 329 tiple pre-activity fit lines is used as the optical onset time, with the difference between
 330 the minimum and maximum times of these intersects used to define the uncertainties.
 331 The uncertainties range from $1 \mu s$ to $\sim 100 \mu s$, with an average of $13 \mu s$. Figure 6 shows
 332 an event where we have determined 4 linear fits. The solid coloured lines show the dif-
 333 ferent linear fits: blue for the sharpest increase in the optical pulse, magenta, red and
 334 green for different segments of pre-activity. The coloured dots show the start and end
 335 of the data used in the fit. The dotted lines show the intersects from the fits of the pre-
 336 activity to that of the sharpest increase. As seen in the figure, the pre-activity has a lin-
 337 ear trend, but can be broken into 3 parts for this particular event. The magenta line shows
 338 the total pre-activity, while the green line uses the data points at what appears to be
 339 a plateau in the pre-activity. Lastly, the red line used the data points in the last part
 340 of the pre-activity where we have a steeper increase than for the previous parts of the
 341 pre-activity.

348 4 Results and discussion

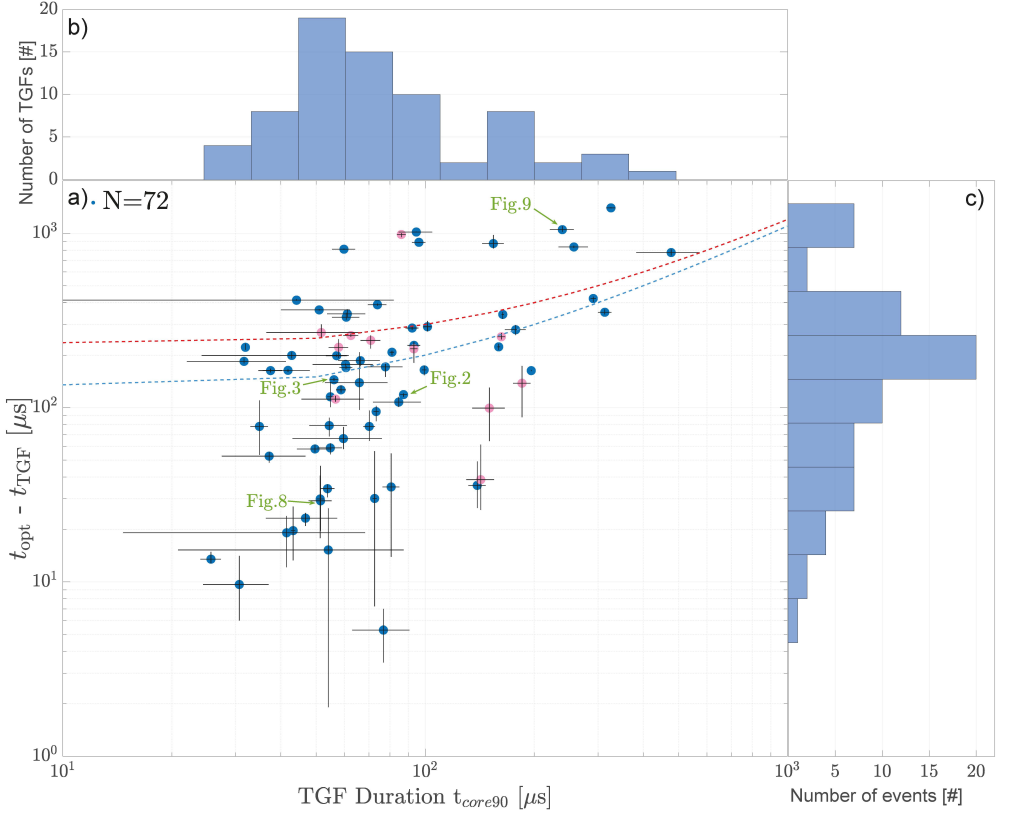
349 During the period between end of March 2019 and November 2020, 221 events were
 350 detected with both MMIA and MXGS data. From these events 88 had no optical pulse
 351 within ± 5 ms of the TGFs. Using the method outlined in section 3 we determined that
 352 for 72 of the events the TGFs are inside the MMIA FoV, and associated to the observed
 353 optical signal. Using the lightning radio atmospherics from GLD360 we find that the ab-
 354 solute timing can be improved for 95 of the 221 events, which includes 45 timing cor-



342 **Figure 6.** Example of optical pulse onset determination. The solid coloured lines show the
 343 different linear fits: green, purple and red lines show fits for different parts of the pre-activity
 344 data, while the blue line shows a fit to the sharpest increase of the optical pulse. The dots on
 345 the fit lines represent the start and end of the data used in the fitting. The dotted lines represent
 346 the intersects between the pre-activity fits (green, purple and red) and the fit for the sharpest
 347 increase.

355 rections for the events where TGFs are determined to most likely be inside the MMIA
 356 FoV. The mean timing correction was found to be $\sim +14$ ms, varying from -11.5 ms
 357 to $+40$ ms.

366 Using the TGF t_{core90} durations and the delay between onsets we plot the relation-
 367 ship between the two in panel a) of figure 7. The blue and pink dots show this relation-
 368 ship, where blue dots have the optical onset determined from 777 nm, and the pink dots
 369 have optical onsets determined from 337 nm. The TGFs showing large uncertainties in



358 **Figure 7.** a) Plot showing the difference in TGF and optical onset times compared to TGF
 359 durations, with accompanying uncertainties. The blue dots show the events with onsets deter-
 360 mined from the 777 nm optical pulse, and the pink dots show the events where onsets were
 361 determined from the 337 nm optical pulse. Green arrows refer to events that are shown in separate
 362 Figures. The dotted red line shows the maximum expected optical delay due to cloud scattering,
 363 of 200 μs, and the dotted blue line shows the expected value (~100 μs). b) TGF t_{core90} durations
 364 in 10 logarithmic bins. c) Histogram of 10 logarithmic bins showing determined delays between
 365 TGF and optical signal.

370 duration have typically low number of counts, for which our method of determining the
 371 TGF duration is less robust. The expected delay of the observed optical onsets due to
 372 scattering in the cloud was modelled by Luque et al. (2020). Using a uniform cloud with

373 typical value for particle radius of 10 μm and particle density of 100 cm^{-3} the delay of
 374 the 777 pulse would be 100 μs for a 6 km thick cloud, and 200 μs for 8.5 km thick cloud.
 375 Considering a cloud-top of 15 km, a delay of up to 100 μs seems realistic, with expect-
 376 tations that TGFs from these altitudes (above 9 km) are easily observable. A 200 μs de-
 377 lay due to a 8.5 km thick cloud would place the source very deep in the cloud (~ 6.5 km),
 378 making it more difficult to observe all but the most powerful TGFs. 200 μs is therefore
 379 used as an upper limit of delay due to scattering. Figure 7a shows the lines correspond-
 380 ing to these two cloud scattering delays added to the TGF durations (dotted red and
 381 blue lines). The plot shows a tendency for longer-duration TGFs to have longer opti-
 382 cal delays.

383 Panel c) of the figure shows the distribution of the optical onset delays with respect
 384 to the TGF t_{core90} start time. The delays are calculated as the duration from the first
 385 photon of the TGF t_{core90} duration and the onset of the main optical pulse. The data
 386 is binned to 10 logarithmic bins. The median determined delay between onsets is 190
 387 μs , with only 9 events having delays over ~ 500 μs . None of the events are observed to
 388 have a negative delay, that is, there are no observed events where the optical pulse on-
 389 set precedes the onset of the TGF. This has been ambiguous in previous work with ASIM
 390 data, but has been improved here due to the new and larger sample of events with bet-
 391 ter relative timing accuracy and our method of determining that the location of TGFs
 392 are inside the MMIA FoV and association to optical pulses. The sequence of events pre-
 393 sented here support the sequence presented in Østgaard, Neubert, et al. (2019). Our de-
 394 termined delay between onsets are a bit different to what has previously been reported
 395 using ASIM data. Heumesser et al. (2021) use ASIM data from between June 2018 and
 396 October 2019 to determine characteristics of the optical pulses associated to TGFs. Heumesser
 397 et al. (2021) shows in figure 3, panel (a), events with negative delays, with a mean source
 398 time of -10 μs and outliers with more than 4 ms delays. We have shown in this work,
 399 using the methods outlined that there are no negative values between onsets, albeit with
 400 a different methodology and somewhat different data set (we only use ASIM data from
 401 after end of March 2019, when the MXGS-MMIA uncertainty was reduced to ± 5 μs).
 402 However, like Heumesser et al. (2021) we see the same trend with the majority of events
 403 having less than $\sim 2\text{-}300$ μs delays between onsets and a similar group of outliers at around
 404 $\sim 800\text{-}1200$ μs .

Panel b) in Figure 7 shows the TGF t_{core90} durations of the 72 events within MMIA FoV, binned to 10 logarithmic bins. The average TGF t_{core90} duration is found to be ~ 140 μs for the full sample of 221 TGFs, with the TGFs inside the MMIA FoV (72 TGFs) having a mean of ~ 100 μs and median of 66 μs , which is similar to previously reported ASIM detected TGFs by Østgaard, Neubert, et al. (2019).

All events are found to have the optical signal after the TGF onset, with the events below the dotted blue line (100 μs scattering delay) being consistent with optical emissions produced simultaneously with the TGF (taking into account typical delay due to cloud scattering and uncertainties). There are 37 events ($\sim 51\%$) which are below the 100 μs delay line (dotted blue), meaning the TGF and the source of the optical pulse could be simultaneous. 15 events ($\sim 21\%$) are above the 200 μs delay line, where the delay of the observed optical pulses can not be explained by scattering from the cloud alone. 20 events ($\sim 28\%$) are between the two delay lines, which means that we can not rule out that the TGFs and sources of the optical pulses are simultaneous. However, we think it is unlikely that so many powerful TGFs are detected from so deep in the cloud. The next subsections will discuss the events that are below the 100 μs delay line (dotted blue), and the events above the 200 μs delay line (dotted red).

4.1 Events where optical onset delay is less than 100 μs

In 7a there are 37 events ($\sim 51\%$) where the delay is less than 100 μs , meaning that the TGF and the source of the optical pulse could be simultaneous, when a more realistic delay due to scattering in the cloud is taken into account. For many short TGFs it is difficult to firmly establish whether the TGFs end before the onset of the optical pulse or not, due to the uncertainties of the method. For some events with longer duration the TGFs appear to be continuing after the onset of the optical pulse, suggesting that the conditions for producing runaway electrons as well as X- and gamma-rays (electric field, voltage drop and seed particles) could still exist after the current through the leader channel occurs. However, most of these events have very weak optical signatures, and we can therefore not make a strong statement based on these outliers. Figure 8 shows one of these events (marked in figure 7 with a green arrow). Panel a) shows the HED and LED detections, with the dotted magenta line showing the first photon of the TGF t_{core90} duration. The 3 lower panels (b-d) show the photometer data from 337 nm, 777 nm and 180-230 nm. The dotted magenta line in the 777 nm panel shows the

437 average onset determined from the method described in section 3.6. As seen in Figure
 438 8 the TGF is not over at the time of the optical pulse onset. The HED counts (black dots)
 439 found after the optical pulse onsets are also high energy, so that they can not be said
 440 to be Compton scattered photons (which can be seen in LED, after the end of the black
 441 dots). This means that the TGF is still ongoing at the onset of the optical pulse, mean-
 442 ing the large electric field needed for TGF production is still in place when the current
 443 surge responsible for the optical pulse starts.

449 4.2 Events where optical onset delay is by more than 200 μ s

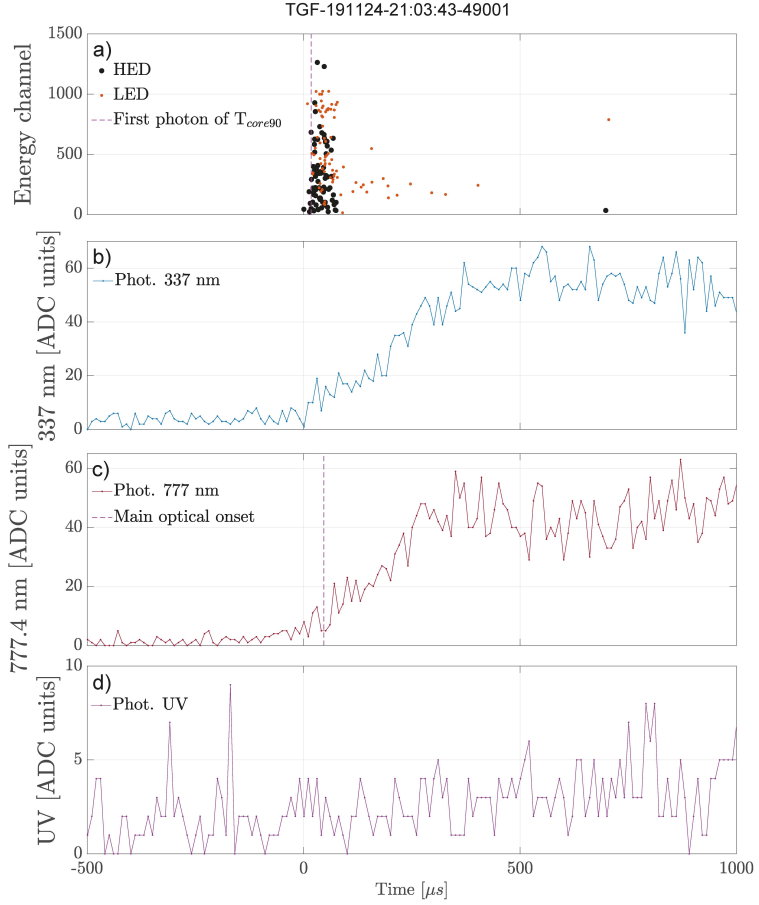
450 In Figure 7 there are 15 ($\sim 21\%$) events that are above the 200 μ s delay line (dot-
 451 ted red). This means that the conditions for TGF production are no longer present, and
 452 a time interval (few hundreds up to a thousand microseconds) before the leader current
 453 occur is observed. Figure 9 shows one of these 15 events, where panel a) shows the HED
 454 and LED counts of the TGF, and the 3 lower panels (b-d) show the photometer data for
 455 337 nm, 777 nm and 180-230 nm. The dotted magenta lines show the onset of the TGF
 456 t_{core90} (a) and optical pulse (c), and a ~ 1 ms delay between the two can be seen. There
 457 is ~ 600 μ s from the end of the TGF to the onset of the optical pulse.

458 The connection between TGF and the leader current is a complex problem. This
 459 study shows that TGFs start before or simultaneous with the optical onset source. The
 460 study also shows that there is a group of events where the TGFs end ($\sim 21\%$) before the
 461 leader current occurs.

467 5 Summary of results

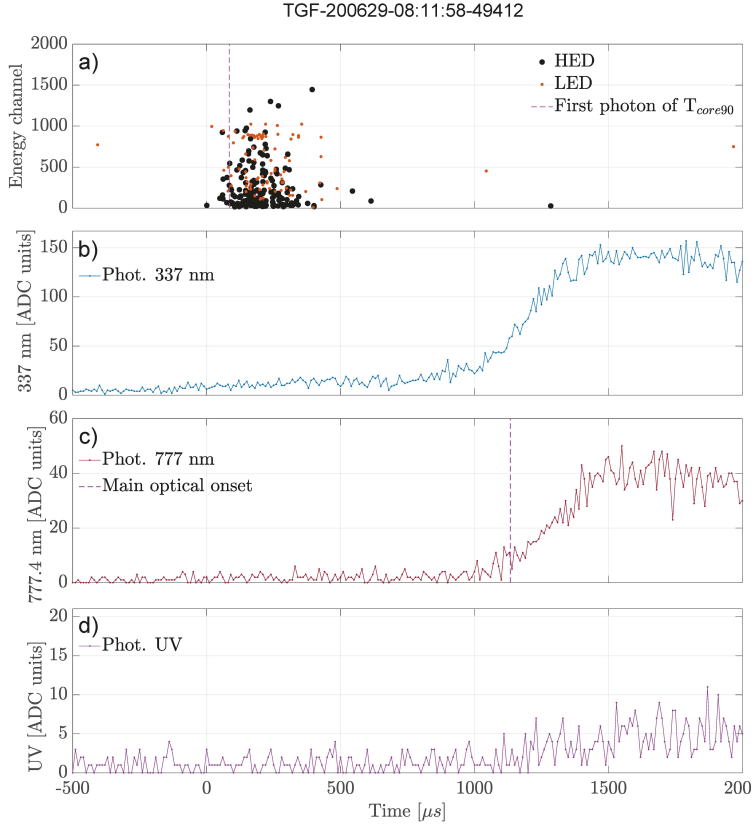
468 Based on the 72 events where we have optical pulses associated with TGFs, we find
 469 the following:

- 470 • All events have TGF onsets before the onset of the optical pulses
- 471 • 37 ($\sim 51\%$) of the events are below the 100 μ s delay line, and therefore have TGF
 472 onsets before or simultaneous with the onset of the optical pulse, taking into ac-
 473 count the light scattering in the cloud
- 474 – Some of these events could have TGFs ending after the onset of the optical pulse



444 **Figure 8.** Plot showing the detection of a TGF that continues after the onset of the optical
 445 pulse. a) shows the HED and LED counts given in energy channels. The dotted magenta line
 446 shows the first photon of the TGF t_{core90} duration. Panels b-d) show the photometer data of 337
 447 nm, 777 nm and 180-230 nm respectively. The dotted magenta line in the panel c) shows the
 448 determined onset of the optical pulse.

- 475 • 15 (~21%) of the events (above the 200 μs delay line) have longer delays than can
 476 be explained by cloud scattering, which means that the TGFs end before the leader
 477 current occurs



462 **Figure 9.** Plot showing the detection of a TGF that has an unusual long delay between onset
 463 of TGF and optical pulse. a) shows the HED and LED counts given in energy channels. The
 464 dotted magenta line shows the first photon of the TGF t_{core90} duration. Panels b-d) show the
 465 photometer data of 337 nm, 777 nm and 180-230 nm respectively. The dotted magenta line in
 466 panel c) shows the determined onset of the optical pulse.

- 478 • 20 ($\sim 28\%$) of the events are between the two delay lines, these events are com-
 479 patible with TGF onsets before or simultaneous with the onset of the optical pulse,
 480 taking into account a 200 μs delay due to light scattering in the cloud
- 481 • Longer duration TGFs tend to have longer delays between the onset of TGF and
 482 the optical pulse

Acknowledgments

This study was supported by the Research Council of Norway under contract 223252/F50371 (CoE) and the European Research Council under the European Union's Seventh Framework Programme (FP7/2007–2013)/ERC grant agreement no. 320839. ASIM is a mission of the European Space Agency (ESA) and is funded by ESA and by national grants of Denmark, Norway and Spain. ASIM data used in this study are available from the ASIM Science Data Center (<https://asdc.space.dtu.dk>). Values determined in this paper and presentations of the 221 events are available at zenodo: *Link will come here*

The data used in this study will be available on zenodo, but while under review we have uploaded the data to a temporary jotta-cloud folder:

<https://www.jottacloud.com/s/221c053c0b5502e4ce7bd5b8c4cc670b1ad>

References

- Abbasi, R. U., Abu-Zayyad, T., Allen, M., Barcikowski, E., Belz, J. W., Bergman, D. R., . . . Zundel, Z. (2018). Gamma ray showers observed at ground level in coincidence with downward lightning leaders. *Journal of Geophysical Research: Atmospheres*, *123*(13), 6864–6879. doi: <https://doi.org/10.1029/2017JD027931>
- Bjørge-Engeland, I., Østgaard, N., Mezentsev, A., Skeie, C., Sarria, D., Lapierre, J., . . . Reglero, V. (2022). Terrestrial gamma-ray flashes with accompanying elves, detected by asim. *Journal of Geophysical Research: Atmospheres*. doi: INREVIEW
- Bowers, G. S., Smith, D. M., Kelley, N. A., Martinez-McKinney, G. F., Cummer, S. A., Dwyer, J. R., . . . Rassoul, H. K. (2018). A terrestrial gamma-ray flash inside the eyewall of hurricane patricia. *Journal of Geophysical Research: Atmospheres*, *123*(10), 4977–4987. doi: <https://doi.org/10.1029/2017JD027771>
- Briggs, M. S., Fishman, G. J., Connaughton, V., Bhat, P. N., Paciasas, W. S., Preece, R. D., . . . Chekhtman, A. (2010). First results on terrestrial gamma ray flashes from the fermi gamma-ray burst monitor. *Journal of Geophysical Research: Space Physics*, *115*(A7). doi: <https://doi.org/10.1029/2009JA015242>
- Briggs, M. S., Xiong, S., Connaughton, V., Tierney, D., Fitzpatrick, G., Foley, S., . . . Hutchins, M. L. (2013). Terrestrial gamma-ray flashes in the fermi era:

- 515 Improved observations and analysis methods. *Journal of Geophysical Research:*
 516 *Space Physics*, 118(6), 3805-3830. doi: <https://doi.org/10.1002/jgra.50205>
- 517 Carlson, B. E., Lehtinen, N. G., & Inan, U. S. (2007). Constraints on terrestrial
 518 gamma ray flash production from satellite observation. *Geophysical Research*
 519 *Letters*, 34(8). doi: <https://doi.org/10.1029/2006GL029229>
- 520 Celestin, S., & Pasko, V. P. (2011). Energy and fluxes of thermal runaway electrons
 521 produced by exponential growth of streamers during the stepping of lightning
 522 leaders and in transient luminous events. *Journal of Geophysical Research:*
 523 *Space Physics*, 116(A3). doi: <https://doi.org/10.1029/2010JA016260>
- 524 Chanrion, O., Neubert, T., Lundgaard, R., Stoltze, C., Tcherniak, D., Jessen, N., ...
 525 Lorenzen, M. (2019). The modular multispectral imaging array (mmia) of the
 526 asim payload on the international space station. *Space Science Reviews*, 215.
 527 doi: 10.1007/s11214-019-0593-y
- 528 Cummer, S. A., Briggs, M. S., Dwyer, J. R., Xiong, S., Connaughton, V., Fishman,
 529 G. J., ... Solanki, R. (2014). The source altitude, electric current, and intrinsic
 530 brightness of terrestrial gamma ray flashes. *Geophysical Research Letters*,
 531 41(23), 8586-8593. doi: <https://doi.org/10.1002/2014GL062196>
- 532 Demetriades, N., Pohjola, H., Murphy, M., & Cramer, J. (2010). Validation of
 533 vaisala's global lightning dataset (gld360). *Conference paper: Technical Con-*
 534 *ference on Meteorological and Environmental Instruments and Methods of*
 535 *Observation.*
- 536 Dwyer, J. R. (2008). Source mechanisms of terrestrial gamma-ray flashes. *Journal of*
 537 *Geophysical Research: Atmospheres*, 113(D10). doi: [https://doi.org/10.1029/](https://doi.org/10.1029/2007JD009248)
 538 [2007JD009248](https://doi.org/10.1029/2007JD009248)
- 539 Dwyer, J. R. (2012). The relativistic feedback discharge model of terrestrial gamma
 540 ray flashes. *Journal of Geophysical Research: Space Physics*, 117(A2). doi:
 541 <https://doi.org/10.1029/2011JA017160>
- 542 Dwyer, J. R., Rassoul, H. K., Al-Dayeh, M., Caraway, L., Wright, B., Chrest, A., ...
 543 Smyth, C. (2004). A ground level gamma-ray burst observed in association
 544 with rocket-triggered lightning. *Geophysical Research Letters*, 31(5). doi:
 545 <https://doi.org/10.1029/2003GL018771>
- 546 Dwyer, J. R., Schaal, M. M., Cramer, E., Arabshahi, S., Liu, N., Rassoul, H. K., ...
 547 Uman, M. A. (2012). Observation of a gamma-ray flash at ground level in

- 548 association with a cloud-to-ground lightning return stroke. *Journal of Geo-*
 549 *physical Research: Space Physics*, 117(A10). doi: [https://doi.org/10.1029/](https://doi.org/10.1029/2012JA017810)
 550 2012JA017810
- 551 Dwyer, J. R., & Smith, D. M. (2005). A comparison between monte carlo sim-
 552 ulations of runaway breakdown and terrestrial gamma-ray flash observa-
 553 tions. *Geophysical Research Letters*, 32(22). doi: [https://doi.org/10.1029/](https://doi.org/10.1029/2005GL023848)
 554 2005GL023848
- 555 Fishman, G. J., Bhat, P. N., Mallozzi, R., Horack, J. M., Koshut, T., Kouve-
 556 liotou, C., . . . Christian, H. J. (1994). Discovery of intense gamma-
 557 ray flashes of atmospheric origin. *Science*, 264(5163), 1313–1316. doi:
 558 10.1126/science.264.5163.1313
- 559 Gjesteland, T., Østgaard, N., Bitzer, P., & Christian, H. (2017). On the timing
 560 between terrestrial gamma ray flashes, radio atmospheric, and optical light-
 561 ning emission. *Journal of Geophysical Research: Space Physics*, 112(7). doi:
 562 10.1002/2017JA024285
- 563 Gjesteland, T., Østgaard, N., Collier, A. B., Carlson, B. E., Cohen, M. B., & Lehti-
 564 nen, N. G. (2011). Confining the angular distribution of terrestrial gamma ray
 565 flash emission. *Journal of Geophysical Research: Space Physics*, 116(A11). doi:
 566 <https://doi.org/10.1029/2011JA016716>
- 567 Gurevich, A., Milikh, G., & Roussel-Dupre, R. (1992). Runaway electron mechanism
 568 of air breakdown and preconditioning during a thunderstorm. *Physics Letters*
 569 *A*, 165(5), 463-468. doi: [https://doi.org/10.1016/0375-9601\(92\)90348-P](https://doi.org/10.1016/0375-9601(92)90348-P)
- 570 Hare, B. M., Uman, M. A., Dwyer, J. R., Jordan, D. M., Biggerstaff, M. I., Caicedo,
 571 J. A., . . . Bozarth, A. (2016). Ground-level observation of a terrestrial
 572 gamma ray flash initiated by a triggered lightning. *Journal of Geophysical*
 573 *Research: Atmospheres*, 121(11), 6511-6533. doi: [https://doi.org/10.1002/](https://doi.org/10.1002/2015JD024426)
 574 2015JD024426
- 575 Heumesser, M., Chanrion, O., Neubert, T., Christian, H. J., Dimitriadou, K.,
 576 Gordillo-Vazquez, F. J., . . . Köhn, C. (2021). Spectral observations of op-
 577 tical emissions associated with terrestrial gamma-ray flashes. *Geophysical*
 578 *Research Letters*, 48(4). doi: <https://doi.org/10.1029/2020GL090700>
- 579 Lindanger, A., Marisaldi, M., Sarria, D., Østgaard, N., Lehtinen, N., Skeie, C. A.,
 580 . . . Neubert, T. (2021). Spectral analysis of individual terrestrial gamma-

- 581 ray flashes detected by asim. *Journal of Geophysical Research: Atmospheres*,
 582 *126*(23), e2021JD035347. doi: <https://doi.org/10.1029/2021JD035347>
- 583 Lindanger, A., Skeie, C. A., Marisaldi, M., Bjørge-Engeland, I., Østgaard, N.,
 584 Mezentsev, A., . . . Neubert, T. (2022). Production of terrestrial gamma-
 585 ray flashes during the early stages of lightning flashes. *Journal of Geophysical*
 586 *Research: Atmospheres*, *127*(8). doi: <https://doi.org/10.1029/2021JD036305>
- 587 Lu, G., Blakeslee, R. J., Li, J., Smith, D. M., Shao, X.-M., McCaul, E. W., . . .
 588 Cummer, S. A. (2010). Lightning mapping observation of a terrestrial gamma-
 589 ray flash. *Geophysical Research Letters*, *37*(11). doi: [https://doi.org/10.1029/](https://doi.org/10.1029/2010GL043494)
 590 [2010GL043494](https://doi.org/10.1029/2010GL043494)
- 591 Luque, A., Gordillo-Vázquez, F. J., Li, D., Malagón-Romero, A., Pérez-Invernón,
 592 F. J., Schmalzried, A., . . . Østgaard, N. (2020). Modeling lightning obser-
 593 vations from space-based platforms (cloudscat.jl 1.0). *Geoscientific Model*
 594 *Development*, *13*(11), 5549–5566. doi: [10.5194/gmd-13-5549-2020](https://doi.org/10.5194/gmd-13-5549-2020)
- 595 Mailyan, B. G., Briggs, M. S., Cramer, E. S., Fitzpatrick, G., Roberts, O. J.,
 596 Stanbro, M., . . . Dwyer, J. R. (2016). The spectroscopy of individual
 597 terrestrial gamma-ray flashes: Constraining the source properties. *Jour-*
 598 *nal of Geophysical Research: Space Physics*, *121*(11), 11,346-11,363. doi:
 599 <https://doi.org/10.1002/2016JA022702>
- 600 Maiorana, C., Marisaldi, M., Füllekrug, M., Soula, S., Lapierre, J., Mezentsev,
 601 A., . . . Reglero, V. (2021). Observation of terrestrial gamma-ray flashes
 602 at mid latitude. *Journal of Geophysical Research: Atmospheres*, *126*(18),
 603 e2020JD034432. doi: <https://doi.org/10.1029/2020JD034432>
- 604 Marisaldi, M., Fuschino, F., Labanti, C., Galli, M., Longo, F., Del Monte, E., . . .
 605 Salotti, L. (2010). Detection of terrestrial gamma ray flashes up to 40 mev by
 606 the agile satellite. *Journal of Geophysical Research: Space Physics*, *115*(A3).
 607 doi: <https://doi.org/10.1029/2009JA014502>
- 608 Marisaldi, M., Fuschino, F., Tavani, M., Dietrich, S., Price, C., Galli, M., . . . Vercel-
 609 lone, S. (2014). Properties of terrestrial gamma ray flashes detected by agile
 610 mecal below 30mev. *Journal of Geophysical Research: Space Physics*, *119*(2),
 611 1337-1355. doi: <https://doi.org/10.1002/2013JA019301>
- 612 Moss, G. D., Pasko, V. P., Liu, N., & Veronis, G. (2006). Monte carlo model for
 613 analysis of thermal runaway electrons in streamer tips in transient luminous

- 614 events and streamer zones of lightning leaders. *Journal of Geophysical Re-*
615 *search: Space Physics*, 111(A2). doi: <https://doi.org/10.1029/2005JA011350>
- 616 Neubert, T., Østgaard, N., Reglero, V., Blanc, E., Chanrion, O., Oxborrow, C.,
617 ... Bhanderi, D. (2019). The asim mission on the international space
618 station. *Space Science Reviews*, 215(26). doi: <https://doi.org/10.1007/s11214-019-0592-z>
- 620 Neubert, T., Østgaard, N., Reglero, V., Chanrion, O., Heumesser, M., Dimitriadou,
621 K., ... Eyles, C. J. (2020). A terrestrial gamma-ray flash and ionospheric
622 ultraviolet emissions powered by lightning. *Science*, 367(6474), 183-186. doi:
623 [10.1126/science.aax3872](https://doi.org/10.1126/science.aax3872)
- 624 Peterson, M. (2020). Modeling the transmission of optical lightning signals through
625 complex 3-d cloud scenes. *Journal of Geophysical Research: Atmospheres*,
626 125(23). doi: <https://doi.org/10.1029/2020JD033231>
- 627 Pu, Y., Cummer, S. A., Lyu, F., Briggs, M., Mailyan, B., Stanbro, M., & Roberts,
628 O. (2019). Low frequency radio pulses produced by terrestrial gamma-
629 ray flashes. *Geophysical Research Letters*, 46(12), 6990-6997. doi:
630 <https://doi.org/10.1029/2019GL082743>
- 631 Said, R., & Murphy, M. (2016). Gld360 upgrade: Performance analysis and appli-
632 cations. *Conference paper: 24th International Lightning Detection Conference*
633 *6th International Lightning Meteorology Conference*.
- 634 Shao, X.-M., Hamlin, T., & Smith, D. M. (2010). A closer examination of terrestrial
635 gamma-ray flash-related lightning processes. *Journal of Geophysical Research:*
636 *Space Physics*, 115(A6). doi: <https://doi.org/10.1029/2009JA014835>
- 637 Smith, D. M., Dwyer, J. R., Hazelton, B. J., Grefenstette, B. W., Martinez-
638 McKinney, G. F. M., Zhang, Z. Y., ... Heckman, S. (2011). A terrestrial
639 gamma ray flash observed from an aircraft. *Journal of Geophysical Research:*
640 *Atmospheres*, 116(D20). doi: <https://doi.org/10.1029/2011JD016252>
- 641 Smith, D. M., Lopez, L. I., Lin, R. P., & Barrington-Leigh, C. P. (2005). Terrestrial
642 gamma-ray flashes observed up to 20 mev. *Science*, 307(5712), 1085-1088. doi:
643 [10.1126/science.1107466](https://doi.org/10.1126/science.1107466)
- 644 Stanley, M. A., Shao, X.-M., Smith, D. M., Lopez, L. I., Pongratz, M. B., Harlin,
645 J. D., ... Regan, A. (2006). A link between terrestrial gamma-ray flashes
646 and intracloud lightning discharges. *Geophysical Research Letters*, 33(6). doi:

- 647 <https://doi.org/10.1029/2005GL025537>
- 648 Wada, Y., Enoto, T., Nakamura, Y., Furuta, Y., Yuasa, T., Nakazawa, K., ...
- 649 Tsuchiya, H. (2019). Gamma-ray glow preceding downward terrestrial gamma-
- 650 ray flash. *Communications Physics*, 2(67). doi: <https://doi.org/10.1038/s42005-019-0168-y>
- 651
- 652 Wilson, C. T. R. (1925). The acceleration of γ -particles in strong electric fields such
- 653 as those of thunderclouds. *Mathematical Proceedings of the Cambridge Philo-*
- 654 *sophical Society*, 22(4), 534–538. doi: 10.1017/S0305004100003236
- 655 Xu, W., Celestin, S., & Pasko, V. P. (2012). Source altitudes of terrestrial gamma-
- 656 ray flashes produced by lightning leaders. *Geophysical Research Letters*, 39(8).
- 657 doi: <https://doi.org/10.1029/2012GL051351>
- 658 Østgaard, N., Balling, J. E., Bjørnson, T., Brauer, P., Budtz-Jørgensen, C., Bujwan,
- 659 W., ... Yang, S. (2019). The modular x- and gamma-ray sensor (mxgs) of
- 660 the asim payload on the international space station. *Space Science Reviews*,
- 661 215(23). doi: <https://doi.org/10.1007/s11214-018-0573-7>
- 662 Østgaard, N., Cummer, S. A., Mezentsev, A., Luque, A., Dwyer, J., Neubert, T.,
- 663 ... Pu, Y. (2021). Simultaneous observations of eip, tgf, elve, and optical
- 664 lightning. *Journal of Geophysical Research: Atmospheres*, 126(11). doi:
- 665 <https://doi.org/10.1029/2020JD033921>
- 666 Østgaard, N., Gjesteland, T., Carlson, B. E., Collier, A. B., Cummer, S. A., Lu, G.,
- 667 & Christian, H. J. (2013). Simultaneous observations of optical lightning and
- 668 terrestrial gamma ray flash from space. *Geophysical Research Letters*, 40(10),
- 669 2423–2426. doi: <https://doi.org/10.1002/grl.50466>
- 670 Østgaard, N., Neubert, T., Reglero, V., Ullaland, K., Yang, S., Genov, G., ... Al-
- 671 nussirat, S. (2019). First 10 months of tgf observations by asim. *Jour-*
- 672 *nal of Geophysical Research: Atmospheres*, 124(24), 14024–14036. doi:
- 673 <https://doi.org/10.1029/2019JD031214>



Graphic design: Communication Division, UIB / Print: Skjipes Kommunikasjon AS



uib.no

ISBN: 9788230852101 (print)
9788230869024 (PDF)